Active and Reconfigurable Millimetre-Wave Antennas and Systems

Peter Alizadeh

A thesis submitted in partial fulfillment of the requirements
for the degree of

Doctor of Philosophy

School of Electronic Engineering and Computer Science
Queen Mary University of London
London, E1 4NS
United Kingdom

September 2017

I, Peter Lawrence Alizadeh confirm that the research included within this thesis is my own work or that where it has been carried out in collaboration with, or supported by others, that this is duly acknowledged below and my contribution indicated. Previously published material is also acknowledged below.

I attest that I have exercised reasonable care to ensure that the work is original, and does not to the best of my knowledge break any UK law, infringe any third party's copyright or other Intellectual Property Right, or contain any confidential material.

I accept that the College has the right to use plagiarism detection software to check the electronic version of the thesis.

I confirm that this thesis has not been previously submitted for the award of a degree by this or any other university.

Signature: 

Date: 22/09/2017

Details of collaboration and publications:

P. Alizadeh, C. Parini, and K. Z. Rajab "An optically reconfigurable unit-cell for Ka-Band reflectarray antennas," *Electronics Letters*, to be published.

P. Alizadeh, C. Parini, and K. Z. Rajab "A Ka-band reflectarray with variable amplitude unit cells," in *Proc. 46th European Microwave Conference (EuMC)*, Oct. 2016, pp. 1295–1298.

P. Alizadeh, A. S. Andy, C. Parini, and K. Z. Rajab, "A reconfigurable reflectarray antenna in Ka-band using optically excited silicon," in *Proc. 10th European Conference on Antennas and Propagation (EuCAP)*, Apr. 2016, pp. 1–5.

A. Andy, **P. Alizadeh**, K. Z. Rajab, T. Kreouzis, and R. Donnan, "An optically-switched frequency reconfigurable antenna for cognitive radio applications" in *Proc. 10th European Conference on Antennas and Propagation (EuCAP)*, Apr. 2016, pp. 1–4.

P. Alizadeh, C. Parini, and K. Z. Rajab, "A low-cost FMCW radar front end for imaging at 24 GHz to 33 GHz," in *Proc. Loughborough Antennas & Propagation Conference (LAPC)*, Nov. 2015, pp. 1–4.

This work was supported by the EPSRC DTC under grant number 1356147

To My Family.

Abstract

The millimetre-wave (mm-wave) spectrum offers considerable advantages in terms of antenna form factor and spectrum availability. However, use of this region often requires reconfigurable antennas and systems. Initially, a review of the various applications which are taking hold in the lower regions of the mm-wave spectrum (30 to 100 GHz) is undertaken. Specifically, reconfigurable reflectarray technologies are selected for further research, and critical analysis of the reconfiguration techniques for including these in antennas is considered.

Silicon as an optically activated semiconductor is chosen as the reconfiguration mechanism due to its low cost and the scope for improvement in this area. A new form of illumination is used, replacing traditional infra-red (IR) lasers with high power IR-LEDs enclosed in a cavity, increasing the efficiency of the silicon illumination. However, to make use of this novel illumination source, and subsequently integrate it into an antenna, the silicon response has to be characterised within Ka-band. This is done through measurements in a waveguide-based characterisation test cell, from which the complex electromagnetic properties of silicon under IR-LED illumination are retrieved with the aid of full-wave simulations.

Using the measured conductivity properties of the illuminated silicon, reflectarrays with non-uniform amplitude distributions can be designed. Through variation of illumination intensities of IR-LEDs throughout the array, it is shown through measurements and full-wave simulations that unit cell reflections can be modified while phases are kept relatively constant. This theoretically allows switching between, for example a low side-lobe pattern binomial array, or a narrow beamwidth pattern Chebyshev array. To implement this, a novel multilayer unit-cell is designed, integrating the IR-LED. This is then used in a full reflectarray design which is measured. The key contributions of this work include the novel illumination mechanism and its integration into a reflectarray antenna, and the use of reconfigurable photoconductive materials to provide a mechanism for beam shaping and pattern synthesis at Ka-band.

Acknowledgement

I would like to thank my supervisory committee, who have been excellent mentors throughout my PhD studies. Dr. Khalid Z. Rajab, who initially sparked my interest in microwaves and antenna design, and has always been understanding that I would rather be in the lab than behind a computer screen! Prof. Clive Parini, whose immense knowledge and experience has continuously steered my research in positive directions. My thanks also go to Dr. Akram Alomainy who has assessed my work throughout and given excellent advice over the past four years.

I would also like to thank the staff of the Antenna Group at QMUL, who have been friendly, helpful, and interested in many aspects of my research. Particularly Dr. Max Munoz Torrico, who has been second-to-none in terms of his assistance with fabrication of test fixtures and measurements, and has always been willing to train me on the various equipment in the Antenna Lab. I would also like to thank Dr Rostyslav Dubrovka who has helped me throughout both financially and with his knowledge of reflector antennas. My thanks also go to the staff of the Electronics lab who have been extremely generous and willing to help, especially Mr. Kok Ho Huen.

I would like to also thank my colleagues in the antenna group, who have become friendly and familiar faces. Fizzah Jilani who has been a constant source of sweets and chocolate; Ardavan Rahimian who is always ready to sort out my Google Scholar; Andre Sarker Andy who has always been a source of lab entertainment; Shaker Alkaraki, whose music is always appreciated; Deepak Nagarkoti who always has a solution for everything; Najmeh Rezaei who brightens the office with her flowers and friendly smile, and Ahmed Aziz, who will make sure that the fridge is always clean! My thanks also go to my friends outside of QMUL, particularly my housemates, for putting up with my late arrivals at home!

Finally, my heartfelt thanks go to my family who have supported me throughout this PhD in knowledge, food and kindness! My gratitude to you cannot really be put into words.

Table of Contents

List of Tables

List of Figures

List of Abbreviations

AC: Alternating Current
ACC: active cruise control
AUT: Antenna Under Test
CATR: Compact Antenna Test Range
CPW: Co-planar waveguide
CST: Computer Simulation Technologies
CW: continuous wave
FET: Field Effect Transistor
FFT: Fast Fourier Transform
FMCW: Frequency modulated continuous wave
GaAs: Gallium Arsenide
GHz: Gigahertz
GPS: Global Positioning Systems
IR-LED: Infra-Red Light Emitting Diode
ISM: Industrial, Scientific and medical
LC: Inductor-Capacitor
LED: Light Emitting Diode
LOCOMO: LOw cost and COmpact Ka-band MObile satcom terminal
LRR3: Long range radar 3
MEMS: Micro Electromechanical System
Millimetre-wave: mm-wave
MIMO: Multiple-input and Multiple-Output
MMIC: Microwave Monolithic Integrated Circuit
NLOS: Non-line-of-sight
QMUL: Queen Mary University of London
QoS: Quality of Service
RF: Radio Frequency
SAR: synthetic aperture radar
SATCOM: Satellite Communications
SiGe: Silicon Germanium
SIW: Substrate Integrated Waveguide
SKA: Square Kilometer Array
SMA: Sub – miniature type A.
SOTM: SATCOM On-The-Move
SPDT: Single Pole Double Throw
VLA: Very Large Array
VNA: Vector Network Analyser

Chapter 1:

Introduction

1.1 Background

The constant challenge facing the various industries and research groups involved in the telecommunications sector is the increasingly sparse availability of the spectrum space. The saturation of the lower RF frequencies, particuleamarly those used by global positioning systems (GPS), Wi-Fi, and cellular networks, has accelerated the movement towards millimetre-wave (mm-wave) frequencies. The shift towards mm-wave frequencies enables the reduction of the overall form factor of the antennas and their relevant matching or feeding networks, which is a potential advantage in terms of cost. Moreover, highly directive antennas with significant surface area reductions are possible due to the inversely proportional relationship between beam width and operating frequency [1]. However, the materials required for efficient, well performing antennas are often more expensive than those found for the lower frequencies below 30 GHz. In contrast, a further advantage which benefits applications in the mm-wave spectrum is that of the available bandwidth. Frequency bands such as Ka-Band (26.5 – 40 GHz), V-band (40 – 75 GHz), W-band (75 – 110 GHz) offer wide allocations of spectrum for various applications such as next generation

wireless communication (5G), satellite communication (SATCOM), high data rate communication [2], automotive radar systems [3] and mm-wave imaging systems [4].

These applications, in particular, have driven the use of the mm-wave spectrum in the last decade. Each has unique requirements, based on both the application itself and the frequency band in which the application operates in. Automotive radar systems illuminate the area directly in front of the vehicle with a broad-beam antenna, but require beam steering at the receiver to provide adequate angular resolution [5], [6]. Similarly, SATCOM systems operating at Ka-Band require beam-steering with narrow beams, allowing for a consistent connection between the user and the satellite [7] but with minimal interference to other satellite systems. High data rate communications, such as those defined in the 802.11ad standard [8], require intelligent beamforming and steerable beams, overcoming propagation limitations such as multipath fading and high absorption. Each of the applications listed above, will be studied in further detail in the following section. The aim is to outline the state-of-the-art products and projects, with emphasis on the reconfiguration mechanisms which are being used in each.

Reconfiguration of a transceiver system can be done in a number of ways. Beamforming is a method to have control over the amplitude and phase at each element of an antenna array. Beam steering is a process in which the radio wave is propagated towards the direction of interest, which can be achieved through a number of different strategies. Beam shaping, also known as pattern synthesis, is a way to manipulate the beams with desired characteristics, without adjustment to the direction of the radiation. In addition to this, reconfiguration may involve the ability to change the operating frequency of the system, or adjustment to the polarisation of the antenna.

1.2 State-of-the-art mm-wave applications

1.2.1 Ka-Band technologies

The frequency band between 26.5 GHz and 40 GHz is referred to as Ka-Band [9], and covers what is widely accepted as the lower mm-wave frequencies. This frequency band has seen a significant increase in interest due to the growth in SATCOM and its proposed usage for fifth-generation wireless communication (5G). Both of these applications require the use of beam reconfiguration, frequency reconfiguration and polarisation diversity. The requirements for a satellite antenna, be it the ground station or the satellite itself, vary depending on its application.

One of the most recent proposals for a set of satellite antennas is outlined in [10]. Here, both Ku-Band (12 GHz – 18 GHz) and Ka-Band antennas are used for satellite uplink and downlink connections. Like many other recent satellite proposals, the objective is to provide high speed internet coverage across the globe, particularly in remote locations. The antennas on each satellite require beam-steering, achieved through phased array techniques, to cover the full view of the Earth. Precision beamforming and side-lobe nulling are used to reduce interference. In total over 4000 satellites are proposed, meaning that reconfigurability is fundamental to the avoidance of interference.

SATCOM On-The-Move (SOTM) presents a new challenge over traditional satellite-to-ground communications. SOTM is used for both military and for consumer products, in which the ground terminal is in motion at speed. The requirement for a consistent connection at high speed requires the use of beam-steerable antennas and intelligent tracking systems. Furthermore, the requirement for these antennas to be mounted on trains or aircraft means that the antenna structure should have a minimal form factor to reduce cost and potential aerodynamic drag [11]. This makes the traditional parabolic dish antennas impractical for this application, and has spurned the development of new types of satellite antennas based around planar adaptation of the aforementioned antenna, namely the reflectarray antenna.

The reflectarray antenna has seen a great deal of interest in the mm-wave regime, its low profile and planar nature makes it ideal for airborne and mobile platforms. Furthermore, it has the ability to have reconfiguration mechanisms incorporated into its structure, which can provide necessary features such as beam-steering or polarisation reconfiguration. Further development to the reflectarray antenna comes from the folded reflectarray antenna design, which has provided additional reductions in the form factor of the reflectarray, making it suitable for various SOTM designs [12], [13].

Ka-band has also seen great activity from the consumer device market, due to it being one of the bands proposed for 5G communications [14]. The need for a new operating band for this new generation of cellular technology is due to the saturated bands at which current cellular networks operate in. The larger available bandwidth in Ka-band increases the data capacity for the mobile channel. Smaller wavelengths in this band pave the way for spatially varying systems including adaptive beam antennas and multiple-input multiple-output (MIMO) antennas and their beamforming networks. In [15], [16] it has recently been shown through analysis of propagation models, that the multipath components, which affect mm-wave frequencies in particular, can be used for link improvement in future 5G systems, especially in non-line-of-sight (NLOS) scenarios. Moreover, rain attenuation and the attenuation of building construction materials must be considered in 5G propagation scenarios. Again, this proves the benefit that adaptive antenna arrays in the next generation of cellular technology.

Both SATCOM and 5G harness the lower parts of the mm-wave spectrum, making use of the wider available bandwidths and smaller wavelengths to enhance systems in ways which would be very challenging at microwave frequencies. However, these two applications operating in the same bandwidths highlights the need for adaptive systems to overcome interference issues which may arise. The reduction in cost of Ka-band transceiver components over time has provided great potential for this band. A similar effect is being seen in its initial stages in the higher frequency band, beginning at 40 GHz and extending up to 75 GHz.

1.2.2 V-band technologies

The frequencies around the 60 GHz mark are currently one of the main bands of interest for consumer products. This is due to the international availability of this band for use in short range high data-rate communication systems such as those proposed by 802.11ad (WiGig) and WirelessHD. This technology will allow wireless docking and streaming of HD quality video from mobile devices to computers and projectors. Fig. 1-1 shows the potential evolution of a wireless network, making use of V-band technology. The interest in these two technologies has been from both an academic research perspective but also from a large number of telecommunication chip design companies. The need for reconfigurability in this band is particularly prevalent, due to the atmospheric attenuation, which limits the point to point communication distance greatly. Overcoming this requires RF beamforming and beam-steering, enabling an increase in the distance over which these frequency bands can be used for consumer applications. These can be provided using various means including beamforming networks such as Rotman lenses [17], Butler matrices [18] or other types of phase shifting technologies [19], [20].

For a system operating in a band with high attenuation, such as the V-band spectrum, the link budget requirements are particularly important. Numerous studies have been carried out on propagation at 60 GHz, including measurements relating to the absorption of various building materials [21], [22], multi-path effects [22]–[24]and on-body propagation [25]

Fig. 1-1: Block diagram for a typical evolution to a WirelessHD system.

The results of these propagation analyses have enabled system designers to develop better chipsets at mm-wave frequencies. Broadcom [26], Intel [27], [28] and IBM [29] each have 802.11ad compatible chipsets, using a variety of technologies which will be studied later in this thesis in more detail. The power handling capability of the semiconductor used is particularly important, due to the power requirements of operating in the 60 GHz band. In the past, more expensive substrates such as Gallium Arsenide (GaAs) would have been used due to the superior power handling capabilities of III-V group semiconductors. However, the development of Silicon Germanium (SiGe) BiCMOS technology has enabled these chipsets to be fabricated at a lower cost than previously possible.

This section of unlicensed mm-wave spectrum can also be used for wireless backhaul networks. Adaptive antenna arrays with beam-steering or cross-polarised antennas, allow for multiple V-band transceiver systems to be located in close proximity, for example on a single rooftop, with little or no interference. A further advantage of operating in this band for wireless backhaul is that of the decrease in antenna size for a given beam width. The high oxygen absorption in this frequency range also provides a level of security that other bands may not be able to benefit from. Any rogue listener would need to be in the immediate vicinity, and be in the transmit path of a fairly narrow beam width antenna, and furthermore, be tuned to the appropriate channel to intercept any data.

The unlicensed nature of this part of the spectrum allows for unique and novel applications which would not be possible in licensed areas of spectrum. Project Soli [30] is one such innovation in this band. Making use of mm-wave radar technology, very fine gesture recognition is possible. Development of the chipset over time has allowed it to be integrated into consumer products such as smart watches and televisions, as shown in Fig. 1-2. The wide bandwidths available in this industrial, scientific and medical (ISM) band allow the radar technology being used to have very high resolution, making fine gesture recognition is possible.

These technologies represent the state-of-the-art of general consumer based mm-wave systems, which have potential or are already present in mass-market products. This section of unlicensed spectrum allows manufacturers to push towards novel and innovative products, making use of traditional concepts such as radar in consumer products.

1.2.3 W-band technologies

The use of radar has reached beyond its original military and metrological applications, and is now present in many other consumer products. The growing market of automotive radar is one such area, in which the 77 GHz band is used for driver assistance and warning systems in many vehicles. Originally only fitted to high-end luxury vehicles, the development of CMOS technology has allowed dramatic cost reduction of a single radar unit. It is now a standard system on many small city cars. High end luxury vehicles may have as many as 8 radar systems with various objectives such as blind-spot detection and active cruise control (ACC). Systems based on mm-wave radar possess a major advantage over visual systems such as camera based image recognition, in that they are not affected by adverse weather such as fog or rain. Operating at 77 GHz also offers an advantage over other frequency bands, as the short wavelength significantly reduces the overall dimensions of the system,

Fig. 1-2: Development of Google's Project Soli, based on an Infineon chipset.

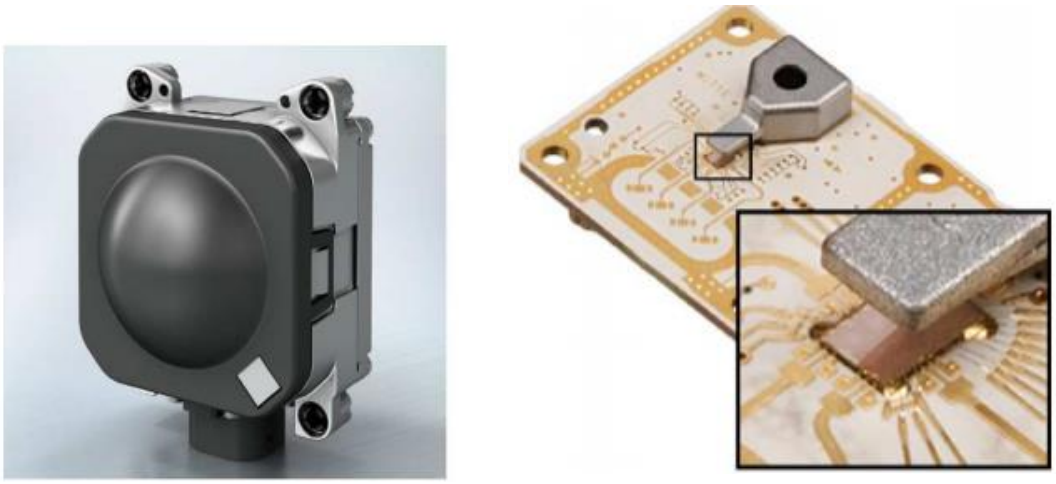

(a) (b)

Fig. 1-3: (a) The Bosch LRR4 radar sensor (b) RF radar transceiver board of the LRR3 sensor; taken from [31].

without a reduction in performance. This is particularly useful given the number of sensors present on new vehicles.

A range of reconfiguration techniques are employed by the major automotive radar manufacturers. The main differences stem from their varying implementations of beam steering, which is necessary for the angle estimation of a detected object. The system designed by Bosch, the fourth generation long range radar (LRR3) [31] minimises component cost by removing active components, and using parasitic coupling between four antennas for angle estimation. Each antenna couples to two adjacent antennas, as shown in Fig. 1-3, which then radiate through a dielectric lens which increases the overall gain and thereby increasing the range of this radar to 250m [32].The proximity of each antenna to the other means that there is a slight beam squint when each individual antenna is activated. This provides the necessary angle estimation.

In contrast to the simple construction of the Bosch radar system, the competing radar system designed by Conti [33], makes use of a mechanical reconfiguration mechanism as used in [34]. This radar consists of multiple mechanical moving components, which may inhibit its reliability in the long term. This radar however, has a further

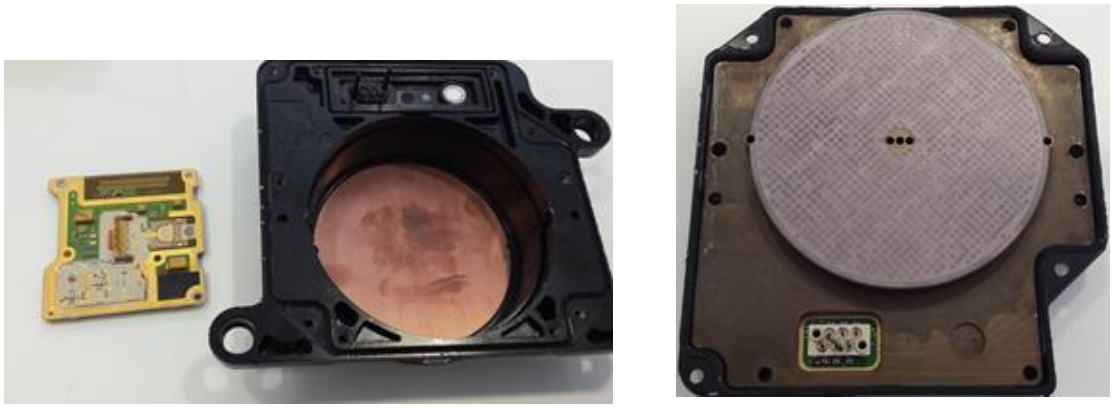

(a) (b)

Fig. 1-4: Components of the reflectarray based Continental radar system (a) Antenna feeds and polarising grid, including outer casing, of the folded reflectarray. (b) Reflectarray elements.

advantage in that it is able to convert between mid-range and long-range modes in a single unit.

Reflectarray antennas are also a possibility for use in W-band automotive radar applications. The non-planar nature of this type of antenna means that a folded reflectarray, which makes use of a sub-reflector, has to be used for automotive radar applications. This is primarily due to the space requirements at the front of a vehicle. One of the original Continental radar systems fitted to Mercedes models made use of this type of reflectarray system [6]. The components of this radar system are shown in Fig. 1-4. The folded reflectarray antenna is made up of multiple components, including the feeding antennas, the reflective surface itself and the polarising grid. The design of folded reflectarray antennas is studied in more detail later in this thesis. Although this type of antenna provides high gain, later models did not continue with this design, perhaps due to its overall size. W-Band is not limited to just automotive radar applications, encompassing further frequencies which have useful properties.

One frequency which is particularly prevalent in W-band is 94 GHz, at which there is an absorption 'window', referring to the lower absorption of propagating signals at this frequency. This has allowed this frequency to become popular for imaging systems, both passive and active. Passive mm-wave imaging systems generate images through detecting the naturally occurring radiation from an object or a scenario. In

many applications, it is necessary to generate images at video rates, overcoming low visibility situations such as fog or smoke, or through opaque items such as clothing. This has only been possible recently due to advancements in mm-wave sensor technology and improvements to the sensitivity of systems [35], [36]. A passive system somewhat lacks the versatility that an active system possesses in terms of imaging techniques, being hampered by its inability to generate different waveforms for object detection. However, a passive system may have uses for military applications, as there is no emitted signature from the system, and has no radiation hazard unlike an active system.

The aforementioned active systems benefit from their ability to illuminate targets or areas of interest with different waveforms, such as frequency modulated continuous wave (FMCW), continuous wave (CW), or pulse waveforms. Mm-wave imaging systems have a variety of applications, including airport body scanners [37], [38], stand-off object detection and synthetic aperture radar (SAR) based mobile imaging systems [39]. The new generation of mm-wave based airport body scanners possess advantages over the current X-ray based systems, due to their non-ionising radiative properties. The stand-off detection of objects also provides the possibility of detecting malicious objects in a non-intrusive manner.

SAR based imaging systems are able to take a high resolution image of an area, and can operate using reconfigurable antenna systems. SAR systems rely on the movement of the antennas across an area, with the image being reconstructed using post-processing techniques. A variation on this is when a SAR system is used in its spotlight mode [40]. In this case, although the platform - typically an aircraft - is moving, the radar beam is fixed on a target area for a longer period of time, thus increasing the azimuth resolution. The primary method for achieving this is through the use of electronic beam-steering antennas.

From this review of the state-of-the-art mm-wave systems for commercial and research purposes, it is clear that a fundamental driver is the need for beam-forming antennas. Although other forms of reconfiguration exist in mm-wave systems,

including frequency flexibility and polarisation diversity, the main requirement is for antennas with pattern synthesis ability, and for antennas with beam steering capability. For this reason, the research in this thesis will focus on these type of antennas, more specifically, those antennas with pattern synthesis capability, to adjust the sidelobes and null locations in the radiation patterns. It is also important to note that this review of the state-of-the-art does not go above W-band. The main reason being that the bands above the W-band are not extensively used in any particular applications at this point in time.

It is evident that research and development on many products is already underway, especially in the V- and W- bands. Table 1-1 summarises the applications in each band, including the stage of development of each one and the challenges which need to be overcome. It is clear that there is still room for development, particularly in Ka-band and V-band. For this reason, the work in this thesis is mainly focused on the technologies in these bands with a primary emphasis on satellite communication.

Table 1-1: Comparison of the state-of-the-art technologies in from Ka-Band to W-Band

Frequency Band	Applications	State of Development	Advantages	Challenges
Ka – Band (26.5 – 40 GHz)	Satellite communications, SOTM, 5G	SOTM – Early; 5G – Early; Sat. Com. – commercialised technology, but many research groups are applying new techniques to this area	Large bandwidth available. Many commercial MMIC chips available.	More congested than other mm-wave bands.
V-Band (40 – 75 GHz)	High – data rate communications, WiGig, WirelessHD. Gesture recognition.	Early	Large bandwidth, small feature size.	High absorption requires high power and multiple antennas.
W-Band (75 – 110 GHz)	Automotive radar, mm-wave imaging systems	Automotive radar – very developed and saturated by major companies; Mm-wave imaging – Some commercialised technology but improvements are being made to increase resolution with new algorithms for data processing	Large bandwidth, very small feature size. Absorption window at 94 GHz.	Complex signal generation required for 94 GHz [REF]. Size of consumer devices at 77GHz limits gain of antennas.

1.3 Aims and objectives of this research

The overall aim of this research is to investigate reconfigurable systems at mm-wave frequencies, initially through a broad literature review, followed by the design and fabrication of a reflectarray antenna operating in Ka-band.

Initially, a study of several applications operating in the mm-wave bands should be carried out with a particular frequency band and application chosen based on this study. A review of antenna systems in this band, techniques and technologies will highlight a technique of reconfiguration which can be developed further.

An in-depth analysis of the performance and characteristics of the reconfiguration should be carried out to ensure its applicability to reconfigurable antennas at mm-wave frequencies. In addition to this, a theoretical model of the proposed antenna concept should also be developed, and its potential is demonstrated through both numerical modelling and full wave simulations.

A full design of the reconfigurable antenna is the next logical step of the design procedure. Careful consideration of the measurement facilities and the design of a test fixture should be carried out, allowing the antenna to be characterised consistently and with repeatable results. The measured results of the reconfigurable antenna should then be analysed through comparison with the numerical and full wave models. Finally, a proposal for a further development of the antenna should be provided.

1.4 Novelty

There are a number of novel aspects to the work presented in this thesis. The first is the use of LEDs, rather than laser based sources for the activation of silicon at mm-wave frequencies, and the comparison of this source to laser based illumination. This work has therefore provided a much more compact light source for use in optically activated antennas.

A second novelty is the use of a number of technologies to form a multilayer unit-cell for use in a reflectarray antenna. Both ink-jet printing and 3-D material printing

have been used in the design of the reflectarray, to provide a means of simple fabrication and a rapidly adjustable design. Furthermore, the unit-cell has been designed around the illumination mechanism, ensuring that it has negligible impact on the mm-wave performance of the antenna.

Finally, there is the novel design of the reflectarray, which makes use of the IR-LEDs to provide a method for pattern synthesis. Pattern synthesis in reflectarrays is often difficult to achieve, due to the increased circuitry required and the limited amount of space in each unit-cell at mm-wave frequencies. However, the novel design of the unit-cell in this work, which incorporates the IR-LED has allowed this to be possible at Ka-band.

1.5 Outline of thesis

In this first chapter, a brief overview of the state-of-the-art technologies and applications in the first third of the mm-wave spectrum has been carried out. It is seen that most applications require beam-steering and reconfiguration mechanisms. The state of development of each application is reviewed and it is concluded that those systems in Ka-band and V-band have most potential for research.

The second chapter provides a more in-depth review of the systems operating in Ka-band, particularly for satellite communications or 5G. Typical antenna designs such as reflector antennas, reflectarray antennas and folded reflectarray antennas are studied and methods for incorporating reconfiguration into these antennas will be considered. A chosen method for reconfiguration and a particular antenna is settled upon, and an outline for its implementation is given.

Chapter three describes the initial design of a test-bed for the evaluation of the reconfiguration mechanism used in this antenna design, namely IR-LED illuminated silicon. The reconfiguration mechanism is looked at in detail, with a description of the physics behind the reconfigurability. A number of characterisation methods are considered, reviewed and tested, with a final method being used to extract the conductivity of the silicon being used in this work at Ka-band.

Chapter 4 shows the design of the final reflectarray antenna, initially undertaking a numerical analysis of the reflectarray antenna showing the potential benefits that the reconfiguration mechanism can provide. The work in this chapter makes use of the characterisation results in chapter three to develop a unit-cell for the reflectarray antenna used in this project. Following this, the unit-cell is further developed for manufacture and is then integrated as part of the full reflectarray antenna concept. This reflectarray antenna is simulated in a full-wave solver to verify its performance.

The penultimate chapter details the measurement procedure used for the reflectarray antenna, including documentation on the antenna test ranges which can be used for the measurement of this antenna. A test fixture is designed for accurate and repeatable testing of the antenna. Initial optimisation of the antenna is carried out prior to the testing of the reconfiguration principle and presentation of the results.

The concluding chapter of this thesis outlines the future work intended for this research. Additionally, conclusions are drawn with regards to the techniques and experiments used in this thesis, and improvements which can be made.

Chapter 2:

Reconfigurable Antennas and Systems

2.1 Introduction

In the previous chapter the lower region of the mm-wave spectrum was explored, with a primary focus on the applications which can make use of this potentially advantageous portion of the EM spectrum. Individual bands were considered and the various drawbacks and advantages were discussed. Based on this, it was determined that an area for further exploration is the frequencies between 26.5 GHz – 40 GHz (Ka-Band). As stated in Chapter 1, this band has been used recently for early automotive radars, and is now predominately a band for satellite communications. Furthermore, it is one of those bands proposed for 5th Generation communications, and as such there is a great deal of research with regards to reconfigurable systems in this band.

These two applications have very different specifications due to the environments in which they operate. The most prominent form of reconfiguration in satellite applications is that of beam forming and shaping, followed by polarisation diversity [41]. Frequency reconfiguration is less common in satellite communications due to the regulatory requirements on the operating bands of satellites. Contrasting this, 5G

systems can make use of frequency reconfiguration, particularly in a system that uses cognitive radio techniques to switch between less congested frequency bands. However, beamforming techniques also have their place in this application.

The next subsection will document the various scenarios that may exist for both 5G systems and for satellite systems. These scenarios will highlight the areas in which reconfigurable antennas can be used, and the requirements that these systems would need to meet. This will be followed by a study of antenna systems which employ these reconfiguration techniques at Ka-band. Finally, a review of particular techniques which can enable reconfiguration at Ka-Band, covering both traditional and novel technologies will be carried out. This review will highlight both the established and the novel reconfiguration techniques which can be explored further for use in antenna systems incorporating these reconfiguration methods.

2.2 Ka-band application scenarios

The two main applications in focus here are satellite communications and fifth generation mobile communications, both requiring reconfiguration. The antenna systems which operate in these bands are relatively complex, with multiple factors needing consideration due to the scenarios. Satellite communications, especially SOTM, have a need for beam steering antennas, with Fig. 2-1 showing a typical scenario for a SOTM system, highlighting some requirements for a SOTM system. With these systems, it is important that the mounted antenna performance is sufficient between the transmitter and the receiver, whilst maintaining a low amount of interference to adjacent satellites [42]. SOTM, in particular, suffers in this regard since the antennas are typically small, due to the need to mount them on a moving vehicle. Due to the inverse relationship [1], between antenna beamwidth and the antenna diameter, the larger immobile antennas which have been previously used for satellite communications do not suffer from adjacent satellite interference due to their lower beamwidth radiation patterns. However, smaller SOTM antennas must be designed carefully to eliminate this undesired RF radiation without an impact on the form factor of the system itself.

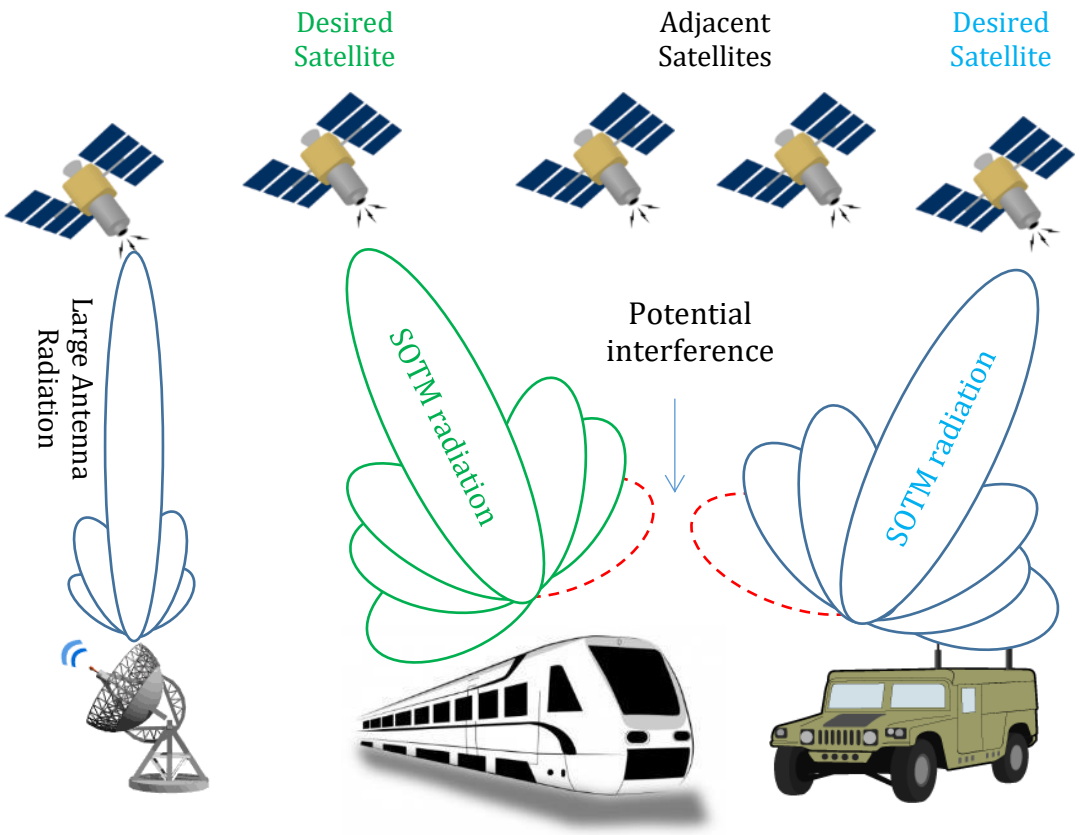

Fig. 2-1: A typical SOTM scenario

Although the standards for a 5G wireless network are not confirmed, some base technical requirements are accepted by those with an interest in this field [43]–[45]. Due to the considerable number of users, the speed at which those users might be travelling at and the additional requirement that the network must ensure a certain Quality of Service (QoS), reconfigurable systems are a vital component of a 5G network. Control of the amplitude and the phase of the radiated signal ensures minimal undesired radiation whilst maximising the radiation to a specific individual in the network. A beamforming system in this situation provides a 5G network with the ability to re-use frequency bands without interference to other users. Further constraints to a 5G antenna system come from the space limitations of mobile devices. A smart antenna system for a base-station can easily achieve the necessary levels of directivity and angle modification [46], [47], but a mobile device may suffer from space limitations. Despite this, promising results have been seen from Samsung in modifications to current handsets [48].

A 5G system consists of many components, each with different requirements. However, in this review of Ka-Band scenarios, the main focus is on the mm-wave components, and predominately those which require reconfiguration. The 5G network components which would require reconfiguration are typically those which are mobile, requiring an adaptive system which can ensure a consistent, high speed connection. Fig. 2-2 demonstrates a specific scenario, one of many in a 5G system, in which smart antennas utilising beamforming techniques will provide an advantage over conventional omnidirectional base station antennas.

Antennas which radiate indiscriminately, in the way that an omnidirectional antenna does, would prevent high numbers of user terminals being used. They would also reduce the speed at which those users could connect. If individual beams can be created for each user using smart beamforming algorithms, then each user can benefit from potentially higher data rates.

It would be difficult to cover every potential scenario which exists in this band, but these show the general need for a reconfigurable antenna system operating in Ka-band. Based on these scenarios, a focus will be placed on satellite antenna systems but some reference to antennas or systems in 5G will be provided, as the techniques used in each application are somewhat compatible.

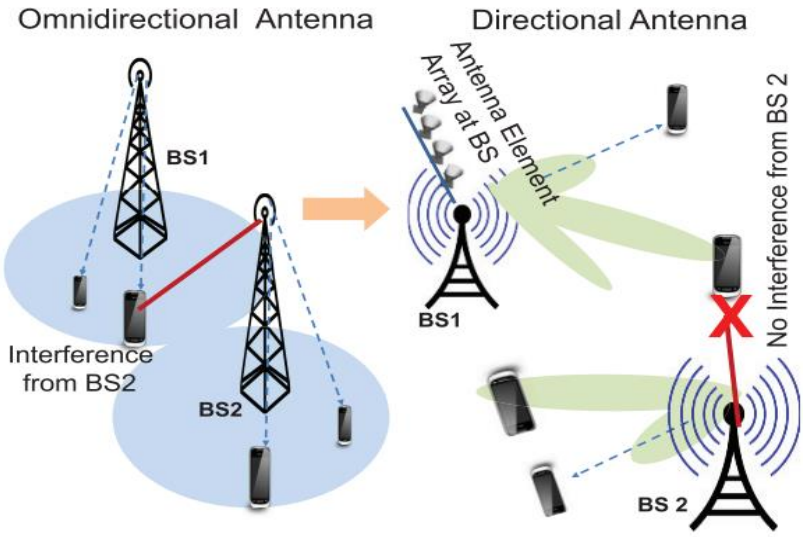

Fig. 2-2: Comparison of a smart antenna based beam forming system with a traditional omnidirectional base station antenna system; taken from [47]**.**

2.3 Antenna systems for Ka-band

Although reconfiguration can take a variety forms, this study of antenna systems has been directed towards radiation pattern reconfigurable antennas, rather than those which reconfigure polarisation or frequency. This is primarily due to the frequency band of interest and the applications which make use of it. Furthermore, it has been established in the previous section, that directive beams are often required, in order to enhance any steering performance and to minimise adjacent antenna interference. Generating these directional beams has often been achieved using phased array antennas and reflector antennas. More recently however, the reflectarray antenna has become popular, which combines the high gain of a reflector antenna with the planar nature of a phased array antenna. Each of these types of antennas will be explored briefly in terms of their basic structures, followed by a number of examples of the current state-of-the-art of these antenna types.

2.3.1 Phased array antenna designs

Phased array antennas consist of multiple unit-cells or elements. They are combined in such a way that the pattern of each individual element combines with others to form a more directive pattern. This makes the antenna much more useful for communications, where the higher gain increases the range of the system, and the increased directivity minimises interference to and from other devices.

The individual elements can be arranged in a linear fashion, with each element adjacent to each other in a single direction. Another common arrangement is a planar array, in which elements are located in both x and y directions. Other possibilities include circular and spherical arrangements of the elements. The shape alone is just one of the factors considered when designing the array. The design must additionally consider the excitation amplitude and phase of each element, the relative spacing between elements, and the individual radiation patterns of each element. Modifications to the excitation phase will result in the ability to change the beam direction, while the shape of the main beam and its side-lobes can be altered through

changing the excitation amplitude of each unit-cell. Additionally, elements which are closely spaced, at less than $\lambda_g/2$ will result in the potential for grating lobes, which are in undesirable in many applications.

Reconfiguration can therefore be incorporated into the design of phased arrays through the modification of the single element pattern, whether through the change of the excitation phase or through the reconfiguration of the amplitude of the excitation. This reconfiguration can be achieved through various mechanisms such as multiple-bit phase shifters based on PIN diodes [49], [50]or FET switches [51], [52], or novel material inclusion into the array [53], [54]. These various mechanisms for providing the phase shift to each individual element will be studied in more detail in the later subsections of this chapter. The elements themselves are commonly planar in nature, with the most simplistic being a square patch. However, many designs operate with modifications to the simple square patch.

Phased array antenna designs based on silicon at Ka-band are very promising as the chip area can be reduced and the full antenna and switching architecture can be incorporated into a single device. Often these silicon based designs will consist of discrete switching components to adjust the phase of each individual element. These will often be multi-bit phase shifters using inductor-capacitor (L-C) switching networks such as those in [55], [56]. Silicon BiCMOS has been used frequently in phased array designs, with this technology enabling the incorporation of power amplifiers, low noise amplifiers and the feeding networks required for antenna operation at Ka-band and above [57], [58]. However, silicon BiCMOS design is challenging, and requires high-level fabrication facilities.

Novel materials can also be applied to phased array antennas. Liquid crystal as a reconfiguration mechanism has been applied to phased array technologies in [54] in a design known as LISA (Lightweight Intersatellite Link Antenna). Here, liquid crystal is combined with horn antennas acting as a phase shifter, which itself is embedded into copper waveguides. The phase delay for each horn antenna depends on the dielectric properties of the liquid crystals, which are controlled by an electric field

passed across them. Each phase shifter can achieve up to 400 degrees of phase shift, but requires ±200 V biasing voltage, which is significantly higher than that which is used in chip-based phase shifting mechanisms.

2.3.2 Reflector antenna designs

The reflector antenna is one of the most visible antennas of the 20th and 21st centuries. It has seen uses in large radio telescopes and can often be seen on the sides of many households as a method for receiving satellite television. It also saw extensive usage as a method of deep space communication, being present on the Voyager 1 and 2 probes, in addition to many other space exploration craft of the 1960s onwards [59]. Its high gain and directional beams make it an ideal candidate for these types of application.

Many designs of reflector antennas exist, but the most common are the planar, front-fed curved, corner and Cassegrain-feed Curved reflector [1]. The feeding point is usually maintained at a position in front of the reflector surface, except in the case of the Cassegrain-fed antenna, in which a sub-reflector is used. The best of these aforementioned designs in terms of the radiation characteristics are the curved reflector designs. If the curve takes the shape of a parabolic dish, then the rays reflected by a point source placed in the focal point of this parabolic dish will be in a parallel beam. The principle of reciprocity can be used to find the focal point of the parabolic dish, as if the dish is illuminated by parallel rays, the reflected rays will focus on a particular point, which is the focal point. This is typically the feed point of the dish. To avoid feed-blockage however, the parabolic shape is often slightly modified to accommodate an offset focal point, meaning that the radiation pattern is not largely affected by the feed.

Although the reflector antenna is not a new concept, it has seen a large amount of recent research. In [60], the feed, which is typically a horn is replaced by a phased array antenna as seen in Fig. 2-3. A 49-element phased array which is controllable using a multilayer board arrangement is used to feed the array at Ka-band. The array

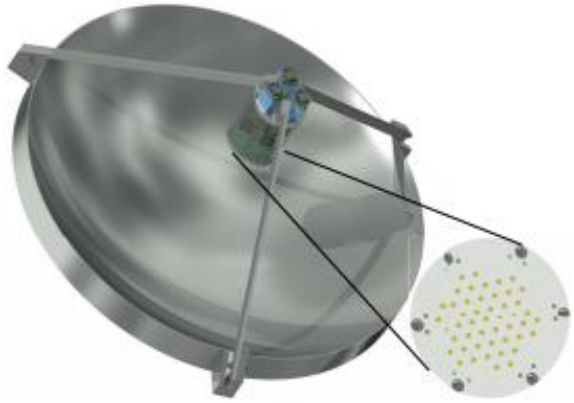

Fig. 2-3: The electronically scannable reflector antenna which uses an active feed showing the spherical reflector with planar array; taken from [60]**.**

itself is reconfigurable and provides the ability to scan the beam of the antenna by ±6° which is beneficial for many applications. This highlights how a classic antenna design can be modified to provide beam-scanning making use of active components.

Another recent advancement in reflector antennas is that of the deployable reflector antenna which is proposed to be present on the next generation of CubeSats [61]. The antenna itself operates at Ka-band and adheres to strict volume and weight requirements stipulated by its use in small satellites. The feeding mechanism for this antenna is a Cassegrain type, in order to minimise the space that the antenna occupies in the CubeSat. Despite the small initial dimensions, once deployed then antenna has a directivity of up to 44.5 dBi at 34 GHz. This enables the system to be used in deep-space applications, which is the next targeted application for CubeSats.

2.3.3 Reconfigurable reflectarray antenna designs

The combination of the two previous antenna concepts has resulted in the establishment of a new type of antenna known as the reflectarray antenna. It still possesses the ability to provide high gain, using a reflective surface, similar to that of a reflector antenna. However, the reflective surface, rather than being a curved parabolic aperture, has a planar nature composed of multiple unit-cells. Therefore, by the combination of array theory, and by analysing the geometry of the reflectarray

(Fig. 2-4), it is possible to form the equations which enable the straightforward design of a reflectarray antenna. These equations will be formulated later in Chapter 4.

The first reflectarray was designed in 1963, consisting of an illuminating horn antenna and an array of waveguide structures [62]. With the advent of planar microstrip technology in the 1980s and 90s, the planar reflectarray was developed [63], [64]. Using microstrip technology has clear advantages in that phase shifting circuits and other reconfiguration mechanisms can be included with ease. Furthermore, the planar nature of microstrip technology means that the profile of the antenna is much lower. This can be further improved with the use of sub-reflectors, allowing this antenna to be embedded into vehicular environments, where space is at a premium.

In the traditional design of a reflectarray, each cell is illuminated by a feed horn which is at a distance from the reflecting surface, as shown in Fig. 2-4. This means that each element will be at a different distance from the feed horn. To have the desired reflected wave in equi-phase in a certain direction, a phase shift must be applied to each element to compensate the elements' distance from the feed horn. In the case where the feed horn is located directly above the central element of the reflecting surface, the phase shift in the centre will be maximum, while those elements at the edges will have the least amount of phase shift applied to them. This phase shift can be applied using modifications to the geometry of the individual unit-

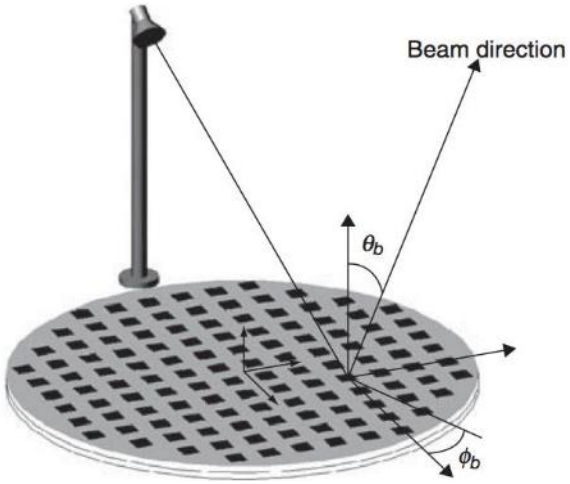

Fig. 2-4: The geometry of a standard reflectarray antenna; taken from [12]**.**

cells resulting in a fixed beam reflectarray. Alternatively, the inclusion of active elements to the unit-cell, similar to those methods used in phased arrays, can provide the reflectarray with reconfiguration in terms of its reflection and thus its beam.

Continuing with the similarities that exist between phased arrays and reflectarrays, the amplitude of the reflection from each unit-cell can be adjusted to provide a similar effect to that which is observed in a phased array. Although most reflectarray designs focus on a phase-only approach, designs which can adjust the amplitude of each individual cell can be beneficial to application requiring shaped beams or null synthesis [65].

Reflection amplitude control has been attempted through the use of integrated FET amplifiers [66], which provide both phase and amplitude control of the reflected beam. However, the associated DC and RF circuits can prove challenging to integrate into the design with the necessary isolation between the respective circuits. The resistor-loaded reflectarray element recently presented in [65] provides a novel technique for amplitude and phase control, but the relatively fixed nature of these elements limits its reconfigurability. Here, they achieve full 360 degree phase range, over a 10dB amplitude variation.

Phase-only reconfiguration of the reflectarray has often resulted in the integration of active non-linear devices into the individual cells [12], [67]. These devices can be lossy, particularly if the array consists of many elements. As a result, mechanical reconfiguration has been considered in [68] to overcome this problem. In this case, the authors have achieved the full 360 degree phase, using micromotors to continuously tune the reflection phase.

Another novel Ka-band reflectarray design is that of a deployable reflectarray, again being designed to meet the requirements of CubeSats. In [69], a state of the art deployable reflectarray is presented, which initially surrounds the outer wall of the CubeSat, and can be opened up to operate at Ka-band with a highly directive beam and gain levels of up to 33 dB. Uncommonly, this reflectarray is fed using a phased

array, rather than the traditional horn antenna, which also goes further towards decreasing the form factor of the design.

The various reconfiguration techniques for these reconfigurable reflectarrays and phased arrays are analysed in more detail in the next sections, highlighting their advantages and drawbacks.

2.4 Reconfiguration techniques for antenna systems

So far, the need for reconfigurable systems operating at Ka-band and beyond has been highlighted through the study of various applications. Satisfaction of this need for particular applications requires the knowledge of the range of techniques available to the system designer. Included in this section is a study of the variety of techniques for the antennas mentioned in the previous sections. Although this study is not comprehensive, it documents the techniques which may be particularly pertinent at Ka-band. Furthermore, it is important to note that some of these techniques, may not have been tested at Ka-band, but may be applicable at higher frequencies if developed further.

The first sub-section will document MMIC-based reconfiguration techniques, which are particularly useful for phased array antennas, especially when combined with beamforming techniques. Following this, MEMS-based reconfiguration is considered which, as was seen in the previous sections functions well in both reconfigurable reflectarrays and phased arrays. Tunable materials are studied after this, which are particularly advantageous for the continuous tuning properties and the high level of integration that these materials can offer. Lastly, mechanical reconfiguration is considered, which is universally applicable to phased arrays, reflector antennas and reflectarrays.

2.4.1 MMIC-based reconfiguration for mm-wave devices

Electronically steered antennas often make use of multi-bit phase shifter chips integrated into the feedlines of the antenna. Phase shifting devices of this sort can

have up to 5 bits, providing quite fine, but discrete resolution. For a 5-bit phase shifter, the spacing between each state is 11.25°. Due to the way that the chip is integrated into the feedlines, the insertion loss is a key concern when choosing or designing such a phase shifter. Various multibit phase shifters for antenna beam steering are compared in Table 2-1.

Phase shifting is typically achieved by switched-line phase shifters with the various types using different switching technologies. The different technologies such

Table 2-1: Comparison of mm-wave phase shifters fabricated using different semiconductor technologies. These devices were being researched at the time they were published and are not commercially available.

Ref.	Device Tech.	Bits	Frequency (GHz)	Insertion Loss (dB)	Return Loss (dB)	Image
[70]	InGaAs PIN	4	46-49 GHz	< 6.1	> 10	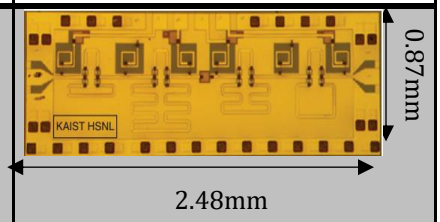
[71]	GaAs FET	4	33-35 GHz	< 14.2	> 10	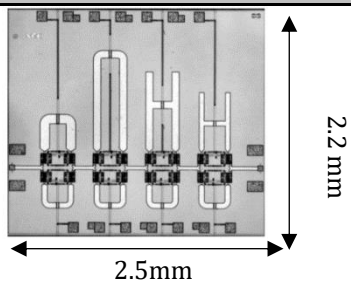
[72]	GaAs pHEMT	3	43-45 GHz	<7.5	>8	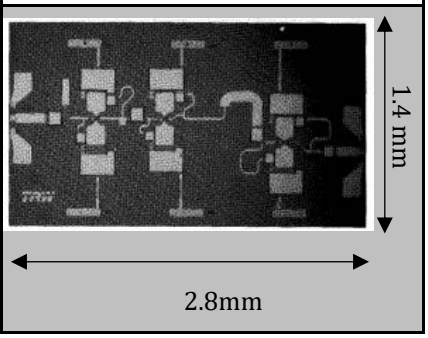

as GaAs FET switches, InP PIN diodes, InGaAs PIN diodes, or SiGe Bi-CMOS.

The table clearly shows that there is a difference between the technologies, particularly in terms of insertion loss. GaAs FET phase shifters have a high insertion loss, when compared to a PIN diode based design. However, it is important to note that as technology progresses, this will improve. The development of transistor fabrication has resulted in an improvement in various parameters of phase shifters, with the most recent designs possessing the best results. Technologies such as SiGe Bi-CMOS have both lowered the chip costs, and enabled the phase shifting mechanism to be embedded into the chip itself [29].

Although this is a very brief study of a few MMIC-based solutions for reconfiguration, it does show that this method is a well-established and commonly used mechanism for the design of reconfigurable antennas. In particular, this method is quite well suited to phased array antennas, which have many individual unit-cells.

2.4.2 MEMS reconfiguration for mm-wave devices

An alternative to these semiconductor based switching technologies is MEMS-based phase shifters or switches. MEMS devices were first proposed in 1986 [73] and refers to devices with microscopic devices with moving parts. An example is the MEMS switch, which has microscopic moving parts which connect and disconnect based on an external controlling voltage.

MEMS-based phase shifters possess advantages including lower loss and lower parasitic components when compared to the phase shifters which are fabricated using FETs or PIN diode based switches. By minimising the loss in a phased array, the need for power amplifiers driving the phase shifters can be reduced, further improving the performance of the array. However, MEMS based phase shifters require higher driving voltages. Nevertheless, overcoming these issues is possible as described by [74]. Two Ka-band designs are presented for use in a phased array antenna. These use switchable shunt capacitive stubs which alter the group velocity of the signal, producing a phase shift. These designs were presented, one at 30 GHz

and another at 35 GHz, with the former showing -2.4dB insertion loss and the latter exhibiting -2.7dB, both of which are lower than those presented in Table 2-1.

Moving away from MEMS-based phase shifters, it is also possible to use MEMS devices in the structure of the antenna or surface. In [75] a MEMS enabled frequency selective surface (FSS) which operates at 60 GHz is designed. The MEMS switches allow the structure to become a reflective surface when they are turned on. The use of MEMS in this case is ideal as the switches provide high isolation between the on and off state – a general requirement for FSS structures. However, the switches used in this particular design require a biasing voltage of 20V, which is higher than what would be required for a PIN diode or FET based switch.

Due to the need for these relatively high voltages, to accurately use a MEMS device in an antenna, it is necessary to model the effect of the biasing lines on the antenna. One such case where this has been carried out is in [76]. A MEMS-loaded frequency reconfigurable antenna was designed for operation in both V-band and the band between 71 GHz and 86 GHz. The use of highly resistive biasing lines is considered in this approach, and the effect on the return loss is analysed. It was seen that lower resistivity biasing lines can have a dramatic effect on the operating frequency of the antenna. Higher resistivity biasing lines can mitigate this issue to a certain extent. This illustrates that, provided accurate simulations are carried out, MEMS switches can be a useful method for designing a reconfigurable antenna at Ka-band or above.

2.4.3 Tunable materials

Tunable materials present a slightly more novel option for reconfiguration. Materials with reconfigurable properties can be integrated into the antenna design to provide one or more forms of reconfiguration. Various materials with continuously variable properties exist including liquid crystal, organic and inorganic semiconductors and ferroelectric materials. Aside from the ability to continuously reconfigure these materials, they can be fully integrated in the antenna solution, avoiding the need for switches or phase shifters on the radiating surface.

Liquid crystal-based reconfiguration mechanisms have grown in popularity in recent years. In [19] a liquid crystal based phase shifter was presented. In this case, a small AC voltage was sufficient to change the permittivity such that a phase shift of 130 degrees could be achieved. An 11V AC signal was used to vary the permittivity of the liquid crystal underneath two reflective loads, giving rise to a change in the capacitance of the loads, thus providing a phase shift.

Similarly, in [77] a phase shifter at Ka-Band utilising liquid crystal technology was presented. In this case a ring resonator filter was used, with the liquid crystal forming the bulk substrate. The liquid crystal had a bias voltage applied to it between 0 and 40V, which provided a maximum of a 117 degree phase shift and an average insertion loss across the biasing states of 3.82dB. These higher biasing voltages are in line with those required for MEMS switches. However, the MEMS-based option will not provide continuously variable phase shift, and the liquid crystal design performs with better reliability.

An alternative method to the permittivity manipulation for providing reconfiguration in an antenna design is that of the conductivity change of a material. Varying the conductivity of a material to cause it to appear more conductive to the incident EM waves can provide a number of options for novel antenna or component designs. An example is presented in [78]. Here a photoconductive switch is designed, which has a filter-like design, fabricated on high-resistive silicon as shown in Fig. 2-5(a). Variation of the conductivity is carried out using an IR-LED with a wavelength of 870nm, which enables the generation of a plasma in the semiconductor. When the

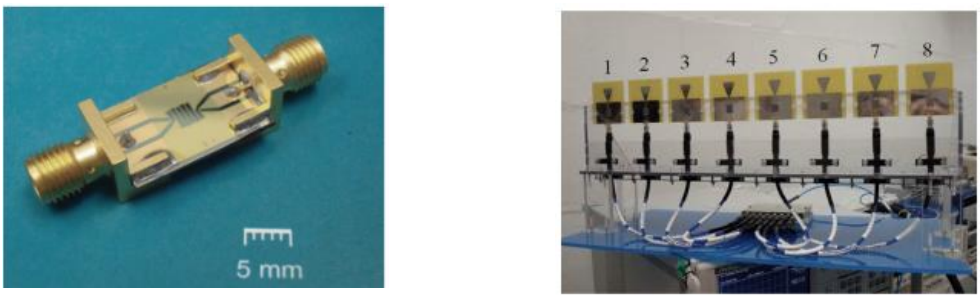

(a) **(b)**

Fig. 2-5: (a) Optically reconfigurable switch using a filter-like construction on high resistivity silicon. (b) Uniform linear array with reconfigurable amplitude weights; taken from [79]**.**

device is not illuminated, the structure has a minimal insertion loss, while in its illumination state, the device is able to attenuate the signal by up to -35dB without the use of a high power illumination source. Varying the illumination intensity enables the variation of the attenuation, such that the device can also act as an attenuator for phased array amplitude weighting. This concept has been extended to a phased array as presented in [79], [80]. As shown in Fig. 2-5 (b) a linear array with these photoconductive attenuators integrated into the feed line provided the ability to adjust the amplitude distribution of the array. This enables sidelobe manipulation through the adjustment of the diode current. This design provides the advantage of not using unpredictable biasing lines close to the antenna radiating surface.

Although this provides a useful means of reconfiguration, it must be noted, that for many cases, using optically reconfigurable semiconductors requires high power light sources as in [81]–[83]. This may make this approach prohibitive for commercial applications. However, if the structure is designed in such a way that this is not necessary, then this technique can provide advantages such as continuous variation of the antenna parameters, removal of unpredictable and lossy biasing lines and fast switching speeds. Despite these potential advantages, this method of reconfiguration

Table 2-2: Comparison of semiconductors for optically activated devices. The cost metric refers to a general pricing and availability of wafers of that semiconductor. A "-" refers to a low-cost wafer, "+" refers to a material which has high priced wafers. Those with a "o" are an average cost wafer, with a price point between high and low-cost wafers.

Material	Band gap nature	Bandgap (eV)	Absorption Cut off Wavelength (nm)	Cost metric	Applications
Silicon (Si)	Indirect	1.12	1117	-	Solar cells, optically activated switches and attenuators
Gallium Nitride (GaN)	Direct	3.44	360	o	Blue LEDs, spacecraft solar panels.
Gallium Arsenide (GaAs)	Direct	1.43	867	o	THz signal generation, high efficiency solar cells.
Indium phosphide (InP)	Direct	1.35	920	+	Some optoelectronics such as lasers
Germanium (Ge)	Indirect	0.67	1851	o	Some photovoltaics

has had little exploration above the ISM bands of 2 to 5 GHz, which leaves room for research in this area towards the mm-wave frequencies.

There are a large number of semiconductors available for use as photoconductors, but only some can be used effectively for optically activated devices and antennas. Table 2-2 summarises some of these, based on their wavelength of absorption, band-gap, and the optically activated applications which they have been used for.

From the table, it is clear to see that there are a range of semiconductors which can be used in optically activated devices. Many of the indirect semiconductors have applications in photovoltaics, while those with direct bandgaps are used as emitters including lasers and LEDs. GaAs is most notable in that it used in THz electronics to assist in the generation of THz pulses through THz gratings [84]. However, the increased cost of GaAs as an optically reconfigurable switch may make it less suitable for this particular application. Furthermore, the short carrier lifetimes of InP devices mean that maintaining a continuous active or inactive state is not possible, but may make it applicable to applications which need high speed switching. Based on the costs of not only the wafer itself, but also costs of the light sources available and their output powers, silicon has shown itself to be the best option for this type of optically activated application.

2.4.4 Mechanical reconfiguration

Mechanical reconfiguration has been one of the more straightforward methods for achieving reconfiguration, particularly at mm-wave frequencies. However, due to the bulky components such as motors, and the possible EM interference that these might cause, mechanical reconfiguration has been recently surpassed by the aforementioned electronic means of reconfiguration. However, for certain applications such as radio astronomy, large, high gain antennas may still use mechanical reconfiguration, since the overall size of the antenna lends itself to this form of reconfiguration. Examples include the Square Kilometre Array (SKA) or the Very Large Array (VLA).

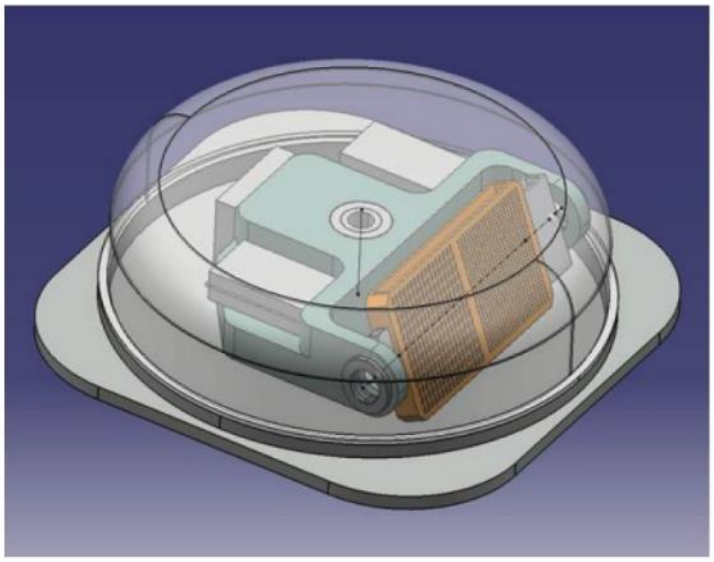

Fig. 2-6: An image of the LOCOMO system; taken from [85]**.**

Mechanical scanning can often provide an economical solution to satellite reconfiguration requirements. A project known as LOCOMO [83] (LOw cost and COmpact Ka-band MObile satcom terminal) makes use of mechanical reconfiguration to scan in two axes of rotation. An image of the proposed system is shown in Fig. 2-6. Despite the use of mechanical reconfiguration, the system maintains a low profile nature while possessing the ability to scan in both azimuth and elevation angles. In the former, it can scan a full 360° while in the elevation plane it can scan from 5 to 90 degrees. Mechanical reconfiguration is the simplest technique for implementing dual-axis scanning, as implementing this electronically would require a high number of switches and biasing circuitry.

However, mechanical reconfiguration can also be found in smaller antennas. In [86] a mechanically reconfigurable cognitive radio antenna was shown. A non-reconfigurable 'sensing' antenna was designed, along with a rotatable 'communicating' antenna. The rotating section has two separate antennas. When rotated, one or the other antenna will connect with the microstrip feed line. This design presents an alternative to using FET or PIN diode switches, which are often used for cognitive radio applications. This technique of using micro-motors can be extended to higher frequencies and much more complex designs.

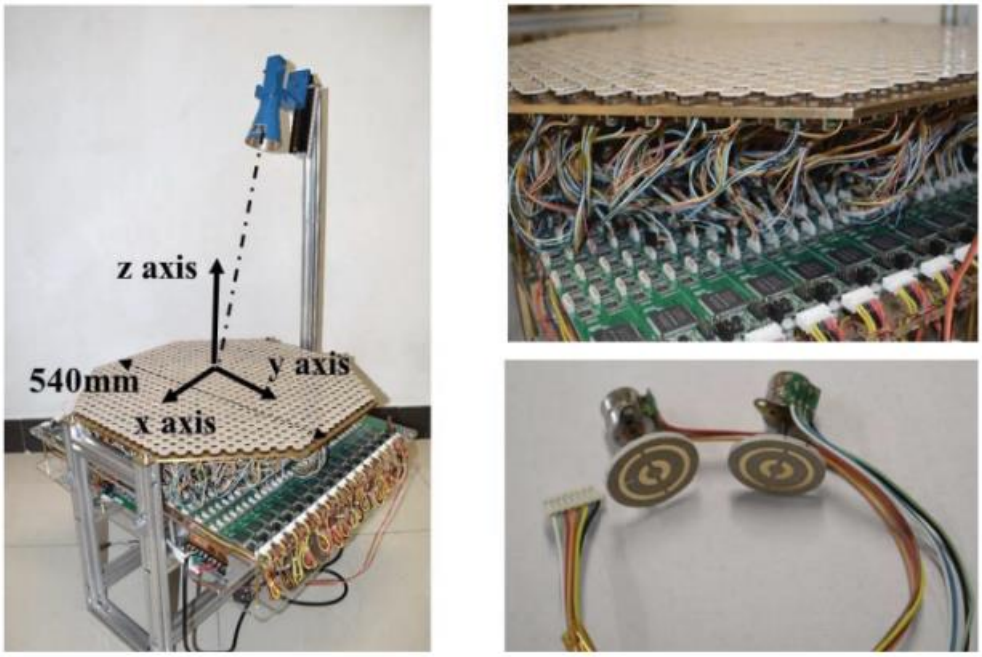

Fig. 2-7: The fabricated micromotor controlled reflectarray showing the array, the control board and the individual elements; taken from [68].

Micro-motors as a means of mechanical reconfiguration are included in [68]. The design overcomes some of the inherent limitations associated with using phase shifters, particularly in a large design. Each element includes a micromotor, which allows the cell to rotate around its central axis, providing 360° reflection phase control. Initial tests proved the concept, and a large-scale 756 element array is fabricated and measured (Fig 2-7). The complexity of this design is quite high, requiring multiple FPGA's and micromotor driver chips, however this method is useful in this design as it removes the large loss that would be associated with RF phase shifting devices on a large-scale array.

2.5 The proposed Ka-band reflectarray

The above study of both the reconfigurable antennas and the mechanisms available to antennas that operate in the mm-wave bands has highlighted the challenges associated with designing a reconfigurable system which include the need for compact sized devices, the increased potential for parasitic effects and the need for many individual devices in array configurations. Moreover, it has shown the need

for reconfiguration in the two application scenarios presented. Furthermore, it has also shown that certain methods of reconfiguration still leave room for further research. One of the least explored areas at mm-wave is the use of optical reconfiguration in an antenna. As a result, this method will be the main focus henceforth of the research into reconfigurable antennas in this work. Additionally, the combination of this technique of radiation pattern alteration with a relativity new design of antenna, the reflectarray, forms a novel and challenging design.

2.5.1 Design challenges

Multiple aspects of the design present challenges. Initially, simulation of a full scale reflectarray is difficult, due to its electromagnetic size with respect to the wavelength. The most straightforward method for simulating large antenna structures such as this is to use high power computing architectures, which can handle the computational complexity of the antenna. However, when this is not available, other approaches can be used, both in simulation and in measurements. For example, a single unit-cell can be simulated and measured which will provide a good estimation of the performance of the full structure. Furthermore, the use of mathematical models can also provide estimations close to that of the performance of the reflectarray.

A second challenge which is envisaged is that of the long-term performance of the illumination mechanism. The use of high power LEDs will require LEDs which are operating close to their maximum performance over long periods of time. Ensuring that the LEDs remain operational is important, and this can be achieved using LED driver circuits. Additionally, ensuring that the LED is in close enough proximity to the silicon substrate itself. The final major challenge would be the design of the measurement test rig, which needs to be designed with both the electromagnetic performance of the array and the movement of any measurement equipment in mind.

2.5.2 Development procedure

The first major milestone of this project would be to characterise the silicon substrate under the optical illumination. Various optical sources will be used, with the trade-offs such as size, power consumption and safety considered. The response of the silicon under the chosen illumination method will be analysed. With this established, it is possible to include the silicon accurately into the simulation models for the reflectarray itself.

Reflectarray antennas follow a common procedure for their design [12]. It is typical to begin with the unit-cell simulations using a full-wave solver. This is often carried out using the infinite array approach, which assumes an infinitely large array of identical unit-cells illuminated by a plane wave. Following this, the unit-cell can be fabricated and tested using a waveguide approach as in [87]. When a good simulation-measurement match is attained, the full reflectarray can be simulated using a full-wave solver. By characterising the unit-cell, a design for this can be finalised prior to running the more time consuming full array simulations. Furthermore, it is possible to reduce the complexity of the simulation model through the use of symmetry planes, and with good consideration of the meshing of the array. This will be covered in more detail in chapter 4. Once simulated, the full array can be fabricated and tested using various methods. An important measurement is the radiation patterns in the various LED states, which include the on and off states of the LEDs, and a distributed pattern for the sidelobe modification.

2.6 Summary

Reconfigurable mm-wave antennas encompass a large variety of antenna designs, and the reconfiguration of the antenna may be in the form of frequency, polarisation, or the antenna pattern. The methods for achieving this reconfiguration are vast, and many of these have been covered in this section.

The main focus of this section has been on beam reconfigurable antennas, including phased arrays, reflector antennas and reconfigurable reflectarray antennas.

These were studied from a structural perspective, showing many of the state-of-the-art designs for these particular antenna types, and how they can be applied to scenarios existing in the Ka-band.

Following the analysis of these antenna structures, and their specific requirements, a study of reconfiguration mechanisms was undertaken, covering many of the recent methods through which phase and amplitude reconfiguration can be achieved. For phased array designs, it was seen that multi-bit phase shifter chips are popular, both semiconductor-based and MEMS-based. In addition to this, antennas in Ka-band have often made used of mechanical reconfiguration to achieve dual-axis scanning. It was seen that while mechanical reconfiguration was previously confined to large antennas, recent size reductions in motor technology has allowed for compact motors to be integrated into phased arrays and reflectarray designs. Continuous scanning of an antenna pattern can be achieved using reconfigurable materials such as liquid crystal or through optically activated semiconductor wafers The research of the latter of these reconfigurable materials is still quite young, and the large-scale incorporation of this type of reconfiguration into an application focussed antenna such as a reflectarray antenna has not been attempted at mm-wave frequencies.

This literature review has highlighted an area in which novel materials can be incorporated into a compact antenna. Therefore, the focus of the remainder of this thesis will be to design a reflectarray which can operate in Ka-band, incorporating optically activated semiconductor devices, providing a novel, antenna which can be used for satellite based applications.

Chapter 3:

Silicon Characterisation

3.1 Introduction

The reconfiguration mechanism is one area of key novelty in this work. Chapter 2 highlighted the fact that silicon as an optically reconfigurable semiconductor, has been used in many designs, first being used by Lee *et al.* in 1980 [88] . However, the various designs [78], [81]–[83], [89]–[91] presented since have further room for development in two areas. The first is to make the illumination mechanism more compact, and the second is to increase the frequency at which this form of reconfiguration has been used in a practical design.

This chapter focuses first on an alternative illumination method, using IR-LEDs rather than the more commonly used laser sources. Once tested at lower frequencies, with a comparison to a laser source, the frequency at which the silicon is used will be increased to cover most of Ka-Band. Furthermore, the properties of the silicon when illuminated will be extracted using a simulation-measurement comparison technique.

The work presented in [89], [90] is essential to assist in the prediction of the characteristics of the silicon under optical illumination. The choice of silicon as the

semiconductor is due to the pre-existing work which has encompassed a large portion of the theoretical principles behind the use of the material as photoconductor. Furthermore, its use in the photovoltaic and semiconductor industries have provided the scope for the development of the processing and fabrication techniques for the material.

3.2 Reconfiguration principle

3.2.1 Energy bandgap

The reconfiguration principle is based on the band-gap of semiconductor materials. Unlike metals and insulator materials, the conductivity of semiconductors can be altered significantly. It is this ability which has meant that these materials have become immensely important in the last century, with many devices such as transistors and diodes being fabricated based on the changeable conductivity of the material [92].

The changes to the conductivity arise from the unique nature of the band gap of the material when compared to metals or insulators. The atoms which make up the material and the energy states of the electrons which exist in their shells are the defining components which determine how conductive a material can be.

Metals, insulators and semiconductors all consist of a valence band and a conduction band, with the former band comprising of bound electrons and the latter band having free electrons. In the conduction band, the electrons are able to move through the lattice of the material and are therefore able to carry a current. Separating the conduction band and the valence band is a region in which there are no electron states. This region exists between the highest energy of the valence band and the lowest energy of the conduction band and is known as the band-gap as shown in Fig. 3-1.

Unlike semiconductors and insulators, the energy levels of the conduction and valence bands overlap in a metal, giving rise to the high current carrying capability of

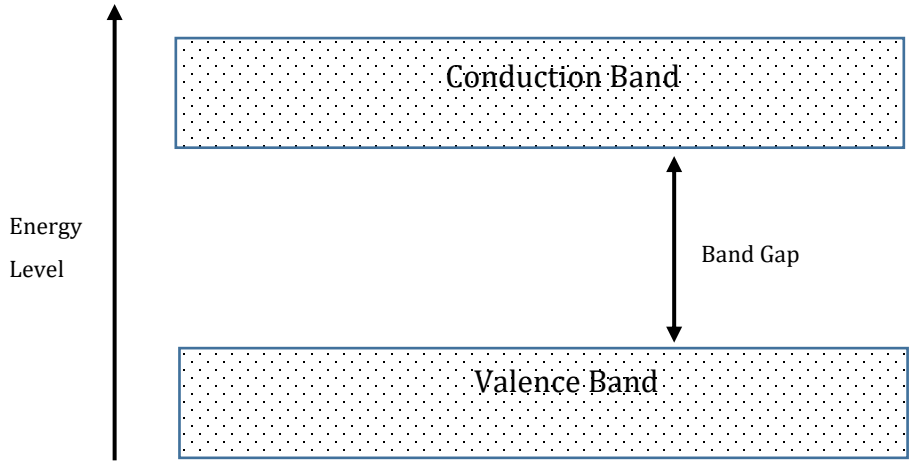

Fig. 3-1: Energy diagram for an ideal semiconductor.

metals. This is because very little energy is required to allow electrons to flow in the material. Semiconductors and insulating materials both have a distinct energy gap separating the conduction and valence bands, but the size of the band-gap in a former is much smaller than in an insulating material. Insulating materials may have a band-gap of 3 eV, while semiconductors can have band gaps as low as 0.36 eV.

The fact that the band-gap of a semiconductor is much smaller means that it is possible for electrons in the fully occupied valence band to enter the conduction band. This happens due to the absorption of external energy sources such as heat or light. When this occurs, the electron leaves behind a 'hole' which behaves as a positive charge. When an external electric field is applied across the semiconductor, the hole will move towards the positive side (cathode) and the electron will move towards the negative side (anode). This means that current flow in the semiconductor is made up of the movement of electrons in the conduction band and holes in the valence band.

3.2.2 Semiconductor doping

Semiconductors can also be modified to alter their conducting properties by adding small amounts of impurities. This is a process known as 'doping'. The addition of a dopant material allows for a modification to the band-gap of the original semiconductor. By appropriately doping the material, it is possible to increase the

conductivity of the material. The dopant can be from an element with either an excess of electrons or an excess of holes. Those which impart an extra electron to the original semiconductor form an n-type semiconductor, while those added to semiconductor and provide an excess of holes become p-type semiconductors.

3.2.3 Direct and indirect bandgaps

Semiconductors can be further sub-categorised into those with a direct bandgap, and those with an indirect bandgap. The difference between these categories depends on the band structure and the momentum that electrons in the conduction and valence band have. If the momentum of the electrons in the valence band is the same as that of the electrons in the conduction band, then the material is classified as a direct bandgap semiconductor. If this is not the case, then the material is classified as an indirect bandgap material. Examples of the former include Gallium Arsenide and Indium Arsenide, while examples of the latter include Silicon and Germanium.

The difference has implications, particularly for indirect bandgap semiconductors. The difference in momentum is in addition to that of the aforementioned energy bandgap, meaning that an increase conductivity through an increase in charge carriers is less likely due to the additional parameter required to free and electron from the valence band.

When the electron moves from the valence band to the conduction band, the conservation of momentum and energy must be satisfied. The electron-hole recombination in a direct semiconductor results in the emission or absorption of excess energy as a photon which has close to zero momentum. However, in an indirect bandgap semiconductor, the electron-hole recombination process is also dependent on the involvement of a phonon, which possesses a momentum equal to the difference in momentum between the electron and the hole in the respective bands.

3.2.4 Photoconductivity

The aforementioned application of external energy sources is the principle by which reconfiguration of the semiconductor is achieved. The properties can be altered significantly through the application of either a light source (photons) or through thermal excitation of the material. It is the former of these that is known as photoconductive reconfiguration. This process relies on the absorption of the photons from a light source to create electron-hole pairs, which only occurs if the photon has enough energy to allow an electron to overcome the band-gap. This is a process known as photo-generation. When this occurs, a layer of free charge carriers forms at the top surface of the semi-conductor closest to the light source, which decreases in conductivity with distance from the surface.

When using any semiconductor, it is necessary to pay attention to the wavelength of the light that is used to illuminate the material, which is directly related to the band-gap of the material. The known band-gap for silicon is 1.11 eV, which allows the calculation of the wavelength of the incident photon to be calculated as follows:

$$E(e\mathrm{V}) = h \cdot v = \frac{hc}{\lambda} \;\rightarrow\; \lambda(\mu\mathrm{m}) \;\approx \frac{1.24}{1.11} = \;\; 1.117\mu\mathrm{m} \qquad (3\text{-}1)$$

Through equation (3-1) it is possible to see that incident light with a wavelength below 1117 nm would be sufficient to promote electrons to the valence band in silicon and alter its conductivity. Therefore, light sources in the visible and near infra-red regions can be used. However, in these cases, high power light sources are used with bulky focussing lenses, which this work aims to avoid.

In the aforementioned region of wavelengths, there are a number of IR-LED devices available which are both compact and can provide high power. Nevertheless, the divergent nature of LEDs when compared to laser sources means that as the distance of the light source to the silicon increases, the incident illumination power density at the surface of the silicon will reduce significantly. It is therefore necessary to ensure that with a light source of this nature, sufficient conductivity change in the

silicon can still be achieved. Furthermore, the wavelength of the available source should be considered, since this will affect the penetration of the light, thus affecting the plasma depth.

Gamlath *et al* [93, 94] and Kowalczuk *et al* [95], [96] have both used a combination of numerical models and 3D EM simulation to evaluate the performance of silicon switches under optical illumination. Based on these, it is clear that the response of the silicon can be predicted in both its on and off state. Particularly, EM simulation software is capable of accurately predicting the performance of optically illuminated silicon and can therefore be used in both the characterisation process and in the design of antennas operating with this reconfiguration mechanism.

It was also shown by Gamlath *et al* [93] that for frequencies well below the plasma frequency, the conductivity effect tends to have more influence in the response than the real part of the permittivity. Furthermore, if the wavelength which is used is such that the plasma depth is small compared with the silicon itself, then the permittivity of the plasma will have very little impact.

In addition to this, the viable illumination sources for activating silicon must be considered. To establish whether IR-LEDs are a usable illumination source, section 3.3 documents a brief review of illumination source options, followed by an analysis of the performance of a silicon photoconductive switch when activated with both an IR laser source, and when activated with high power IR-LEDs placed in close proximity to the switch.

3.2.5 Non-linearity considerations

One of the key advantages of using a bulk semiconductor as the reconfiguration mechanism is that the power handling of this is superior to that of PIN diode or FET switches. In [97], the power handling of a photoconductive switch is considered through measurements. To test this, a high power RF source is used which is able to provide up to 44 dBm (25W) to an optically activated RF switch, and was only limited by the silver epoxy attaching the switch [96]. Based on these results, it may be

possible to use higher powers than these provided the silicon does not need an electrical connection to other devices. Such a system may have applications including high power satellite antennas, or applications relating to military radars.

3.3 Illumination source comparison

3.3.1 Types of illumination sources

The nature of the bandgap of silicon, combined with the myriad of applications which have been proposed making use of optically activated semiconductors, has given rise to a variety of illumination sources. Laser sources are often used, with some using simple direct illumination [81] without any focussing, while others use lenses [94] to ensure that the illumination is localised to a specific area .

The first reported optically activated reconfigurable mm-wave device was a phase shifter presented by [88] which made use of a 400 mW laser operating at 530 nm. This was further combined with a mask which ensured a fixed length plasma was generated in the silicon. Furthermore, a piece of fine ground glass was used to diffuse the incident light to ensure a constant illumination on the silicon. This early technique did not use the optimum wavelength for the laser source, but provided an early indication that reconfigurable photoconductive devices are possible and useful.

Various microwave devices and antennas have been proposed by the group at Loughborough University [83], [89], [95-99]. These devices again make use of laser based sources, but in some cases, combine these with fibre optics to ensure that the illumination is as efficient as possible. This is the case in[83], [95], [97], where a 980 nm, 200 mW laser source is combined with fibre optics to activate the silicon switches. This is a good method of ensuring that as much of the illumination as possible reaches the silicon devices, but does increase the form-factor of the design itself.

Haupt and Flemish [78], [100] showed the first use of a standard IR-LED as an illumination source for a reconfigurable photoconductive array. In this case, the

authors used an 870 nm IR-LED source in close proximity to the RF device. Despite the IR-LED operating at quite a high radiant intensity of 60 mW/sr, the RF device in this case acted as an attenuator, due to the fact that an IR-LED will not provide a high enough illumination power to the silicon to provide performance equivalent to PIN diodes or FET switches.

This highlights that there are generally types of illumination source which are suitable for this application: the first being laser based sources and the second being IR-LEDs. Both of these have their advantages and disadvantages. Laser based sources are bulky in themselves and are not fully practical for an application focussed design, but do allow the silicon to operate with excellent on-state characteristics. IR-LED sources provide a means to reduce the form factor of the illumination source, but careful consideration of the design has to be carried out, due to the lower illumination power available from an IR-LED. Although the literature shows that IR-LEDs are a feasible illumination source, it is necessary to also consider the on-state characteristics of the silicon when using them, and due to their relatively limited use, their feasibility at higher frequencies should also be considered.

3.3.2 Laser vs. IR-LED illumination

An initial study to compare the practical use of IR-LEDs to that of laser diodes was carried out. The experiment was carried out up to 6 GHz, which was due to the limitations imposed by the measurement equipment. More specifically, the limited frequency range was due to the need to carry the experiment out in a laser safe environment, where only an Anritsu portable VNA was able to be used. Previous characterisation work in [81], [94] has made use of microstrip gap structures, so a similar procedure was used here. A microstrip board, as shown in Fig. 3-2, was designed in CST, and fabricated on a 1.6 mm thick Taconic TLY-5 (ε_r = 2.2) substrate. The microstrip line had a gap of 0.3 mm in the centre, across which a high resistivity (ρ = 5000 Ω-cm) silicon piece with a thickness of 0.2 mm was fixed using silver epoxy. Two SMA coaxial connectors were used on both sides of the board for connection to the VNA.

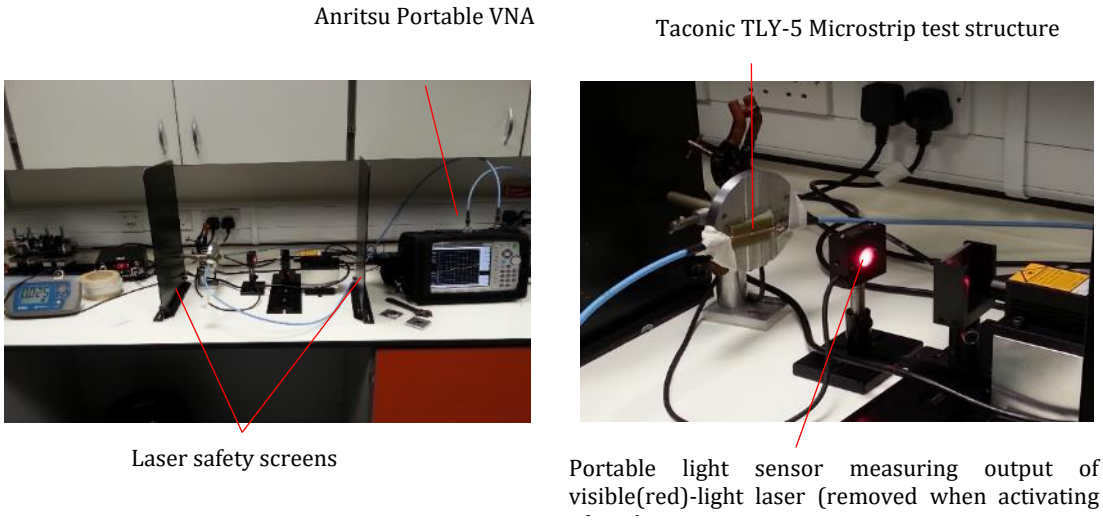

Fig. 3-3: Experimental setup for measurement of the silicon response under laser illumination. The right image shows the detector being tested on a red laser. The IR laser was not visible on the detector.

The microstrip board was illuminated by a 980 nm laser diode, with a maximum output of 400 mW, as shown in Fig. 3-3. Although the source can illuminate up to 400 mW, it was discovered that the values for the transmission (S_{21}) do not significantly improve at illumination powers above 100 mW. As such, the power level was maintained at 100 mW for the recorded results.

Following the use of the laser, the board was also illuminated with a portable reconfigurable light source with an operating wavelength of 850 nm [101], as shown in Fig. 3-4(a). Each LED can be individually switched on, giving a maximum total output power of 280 mW when all three LEDs are illuminated. To minimise the power

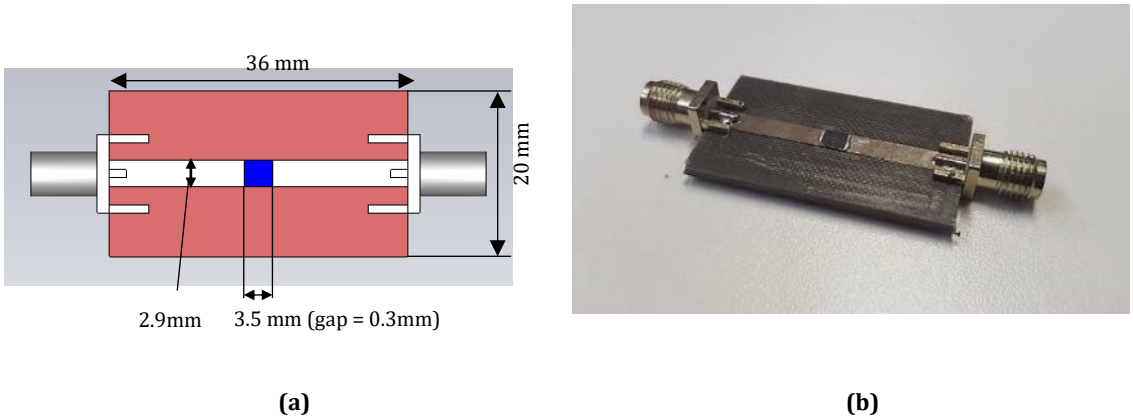

Fig. 3-2: (a) Simulation model of the Taconic TLY-5 microstrip board (b) the fabricated board with silicon switch mounted using silver epoxy. The substrate thickness was 1.6mm

lost due to the divergent nature of the LEDs, the light source was placed very close to the light meter when measuring its maximum output illumination power. This was also replicated when taking the transmission measurements of the board. Three measured illumination powers are achievable with this illumination source: 70 mW, 150 mW and 280 mW, for one, two and three LEDs illuminated respectively. These power values are measured with the portable light meter, which is not the same power level as that which falls on the silicon piece, as the illumination area is smaller when illuminating the silicon. An improved method for varying the output power of the LEDs would be to adjust the current to all three LEDs, thus maintaining the illumination pattern falling on the die.

The comparison between the laser illumination source at 100 mW, and the three different LED illumination states is shown in Fig. 3-5. Due to the focussed nature of the laser, more of the output power can be focussed directly onto the silicon piece. This means that when using a laser, for a lower optical power, a higher transmission can be achieved. It is also the case that the wavelength of the illumination source may have an effect on the transmission performance of the silicon and should be chosen. The difference in wavelength of the illumination sources will have an impact in the absorption depth in the silicon. The longer wavelength laser would go further into the silicon than the shorter wavelength LED illumination. An 880nm LED was used for the primary reason that the LEDs operating at 980nm at this time were not of high

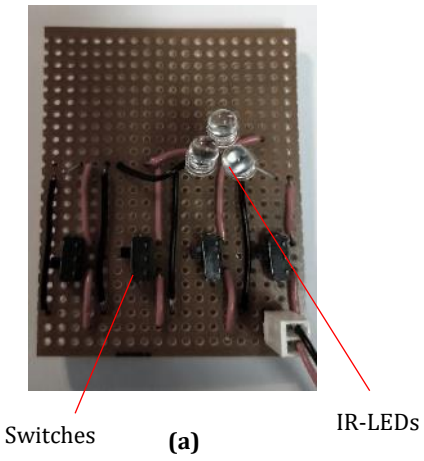

Fig. 3-4: (a) Image of the three LED variable light source

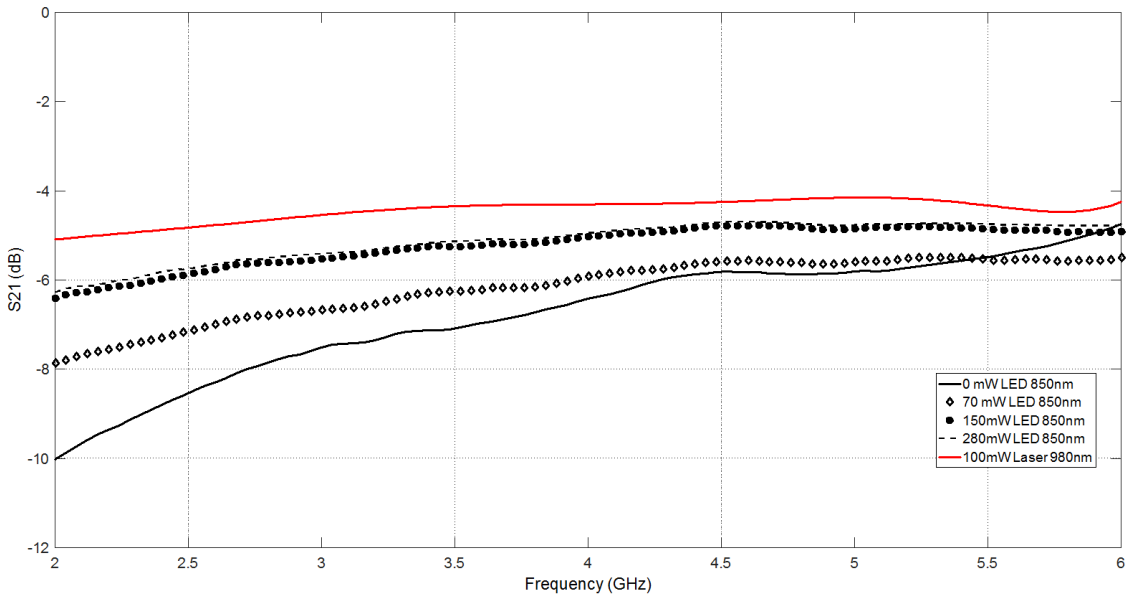

Fig. 3-5: Comparison of transmission for different illumination methodologies for a microstrip board with a 0.3 mm gap.

power levels. Although the 880nm will impact the results, the power level was considered to be the most important factor. Finally, the results show that 150mW and 280mW cases for the LED, only a slight difference in the transmission performance is observed. This is because the method of focusing the LED illumination is not sufficient to ensure that the increased power from a third LED falls directly onto the silicon piece. Therefore the alternative method of adjusting the current of the LEDs would have been an improved method for varying the illumination power.

Fig. 3-5 shows that there is a discernable difference between the level of the transmission for the highest power of the LED and the laser source. At 2.4 GHz, the difference is approximately 1.2 dB, which is 25% less transmission than observed with the laser. However, the compromise for the higher transmission is a much bulkier and more expensive illumination source.

Another observation which can be attained from the results in Fig. 3-5 is that the coupling across the gap is a significant factor in the design. As the frequency increases, the transmission in the off state also increases. Extrapolation of this result would more than likely show that the un-illuminated transmission would become higher at increased frequencies. As a result, a larger gap size is required to show the deviation

in the transmission results between the illuminated and un-illuminated states, particularly when this structure is used towards Ka-Band.

3.4 Silicon characterisation under IR-LED illumination

In [94], a microstrip gap structure on a silicon substrate was characterised up to 50 GHz, using a measurement – simulation matching technique. A 500 um thick substrate with a variable gap was designed, connected using two V-band connectors. A 1 W 830 nm wavelength laser diode and a combination of two lenses were used to illuminate the gap. To characterise the silicon under optical illumination, a highly accurate model of the measurement set up was designed in CST. The photo-induced plasma was modelled as a multilayer structure, with varying conductivity between each layer. Using this technique, the authors were able to extract conductivity levels for the plasma based on the illumination intensity.

Further work has included8 the characterisation of silicon beyond 50 GHz. In [82] a 3000 Ω-cm silicon wafer was used under optical illumination from a 980 nm IR laser source. By measuring the reduction in transmission (S21) as the conductivity increased, it was shown that a maximum conductivity value of 300 S/m could be achieved at 500 mW. This was achieved up to 170 GHz. It was also noted that at a certain illumination power, the transmission performance begins to saturate and will not improve further.

The characterisation procedure used by Gamlath *et al*. provides a straightforward and accurate method for extracting the illuminated properties of the silicon. However, two requirements exist when using this technique. The first is that the CST model must be very accurate, and the second is that the quality of the fabrication of the test structures must be high. In this way, it is possible to match the simulation and measurement results, such that the only parameter which affects the result is that of the conductivity of the silicon.

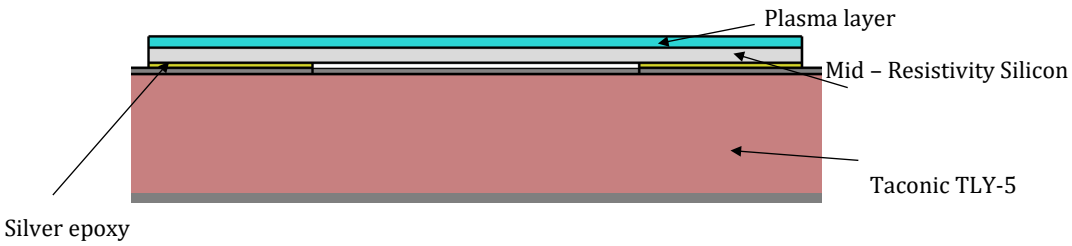

Fig. 3-6: Parameterised layout of used for accurately modelling the silicon on the microstrip board.

3.4.1 Transmission line parameter extraction.

To establish the feasibility of the simulation-measurement parameter extraction technique, the same Taconic TLY-5 microstrip board was used to extract the properties of the silicon up to 9 GHz. However, the silicon piece was changed to a medium resistivity silicon piece due to the better availability of this for future experiments. Gamlath *et al* have previously shown a method for designing a highly accurate model for modelling the conductive properties of silicon through the use of a multilayer plasma model with decreasing conductivity as the distance from the illumination source increases [94]. Nevertheless, this was only necessary at high frequencies above 20 GHz.

This shows that the model used in CST needs to be highly accurate, such that the only two parameters that affect the simulation result are the conductivity of the silicon and the plasma depth of the conductive part of the silicon. For this, in addition to accurately modelling the SMA connectors, the silver epoxy used to attach the silicon to the microstrip line was also modelled, as shown in Fig. 3-6. In this case, the silicon was modelled with a constant conductivity through the plasma layer, however a more accurate procedure would be to use a decaying conductivity as the distance increases from the top surface of the silicon.

The measurements were carried out using a similar process to that which was used for the laser and LED comparison experiment. However, in this case a Keysight PNA-L was used, which allowed the frequency range to be increased, being limited by the microstrip performance above 9 GHz. Furthermore, due to the illumination

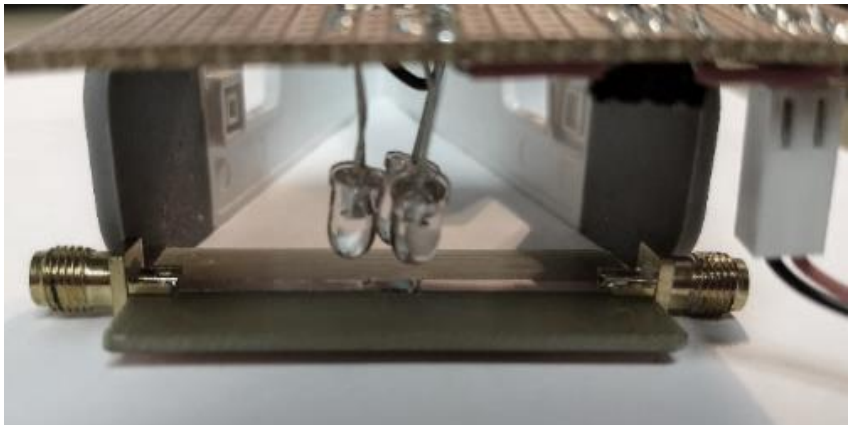

Fig. 3-7: Measurement setup for the characterisation of the silicon up to 9 GHz.

methodology, shown in Fig. 3-7, it is important to consider the impact of the proximity of the LED source. An initial measurement in off-state was carried out in which the light source was present and then removed. Negligible difference was observed between the two situations, confirming that the physical presence of the light source does not impact the result.

The transmission results (S_{21}) were recorded and imported into CST. The dimensions of the CST model were then modified to exactly match the fabricated design. This was due to slight variations being present between the fabricated model

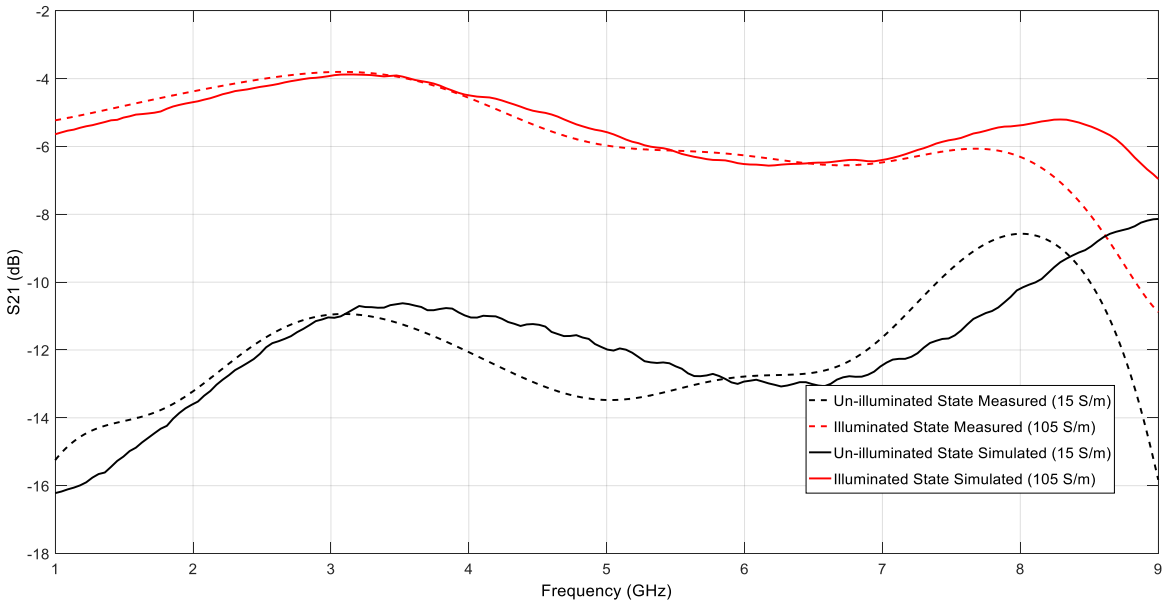

Fig. 3-8: Simulation and measurement comparison up to 9 GHz for the illuminated and unilluminated state.

and the initially designed model due to fabrication tolerances. The off state and the full illuminated state were both fitted to the experimental measurement results by using parametric sweeps of the conductivity and the plasma depth of the silicon. The bulk silicon conductivity remained constant, while the conductivity was varied in the plasma layer. Once the profile and level of the response was matched sufficiently to the measured results, the conductivity and plasma depths were noted.

In the off-state, the conductivity observed was estimated to be 15 S/m which matches with the use of medium resistivity silicon. The on-state deviated significantly from the off-state across the 1 to 9 GHz band as shown in Fig. 3-8, with a conductivity level of 105 S/m being observed.

3.4.2 Waveguide parameter extraction

Although the microstrip transmission line based simulation-measurement parameter extraction technique provides good results for frequencies below 10 GHz, the fabrication of the structure requires much more consideration above this. Furthermore, the coupling across the gap becomes significant as the frequency increases. To overcome this, a waveguide based design is used, in which the fabrication quality can be improved. Further improvement in the measurement procedure is found through the improved method in which the LED illuminates the silicon piece. This is achieved by the use of much smaller surface-mount IR-LEDS.

The IR-LED used in this characterisation, a Philips OSRAM SFH 4710 [102] is significantly smaller than the IR-LEDs used for the previous experiments up to this point. This particular LED operates at 850nm, with a radiant intensity of 63mW/sr. It has a half angle of ±65° which is quite large, but this can still be used if the LED is placed in close proximity to the silicon. Although the radiant power is also less than that of the LEDs used in the previous experiments, locating the LED inside a cavity ensures that the illumination of the silicon is as efficient as possible. The LED itself operates with a biasing voltage of 1.6 V, requiring 500 mA for its maximum radiant intensity. The dimensions of the LED are 1.6mm x 1.2mm.

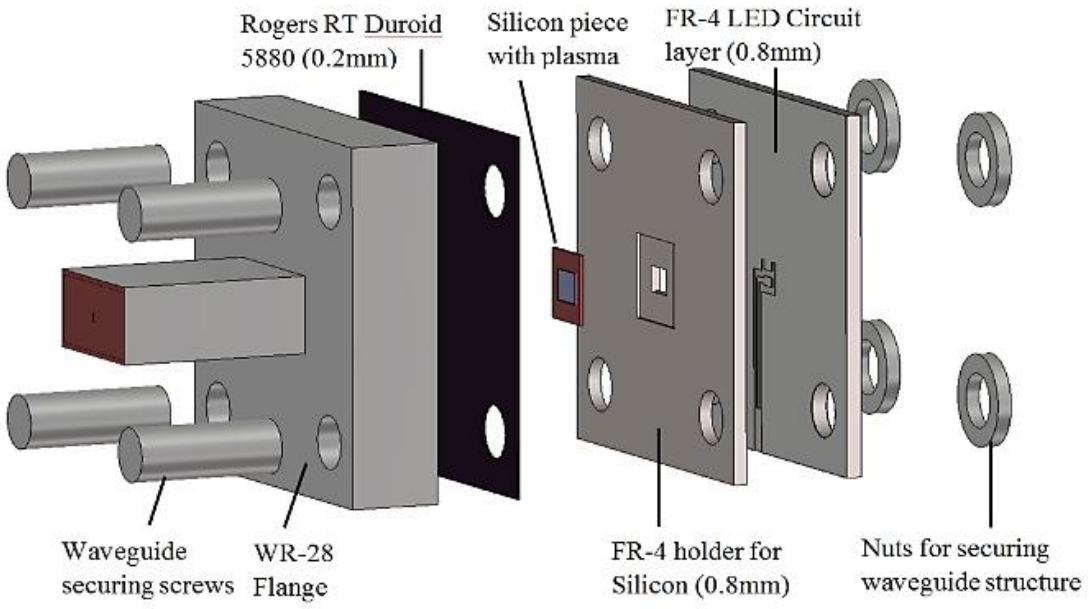

Fig. 3-9: Simulation model for the waveguide based silicon characterisation.

A multilayer design is used which can be attached to a WR-28 waveguide flange and is fixed using screws. The simulation design is depicted in Fig. 3-9. The lowest layer of the structure consists of the biasing circuit for the LED, which is designed to appear as a ground plane to the incident RF signal. The IR-LED is soldered to the top of this piece of FR-4. The silicon is placed in an indentation in a second piece of FR-4 located above the LED. A hole is present in this FR-4 holder, which matches the dimensions of the LED, effectively forming a cavity for the LED. This ensures that the illumination of the silicon is as efficient as possible. Above this, a thin layer of Rogers RT Duroid 5880 is used to secure the silicon piece while not attenuating the incident RF signal due to its low thickness and low loss.

The measurement setup is shown in Fig. 3-11**.** The characterisation cell is secured to the waveguide flange of a calibrated port extension. The port extension is used to protect the coaxial to WR-28 transition, which is necessary to connect to the cables of the VNA, in this case a Keysight PNA-X. Two biasing wires are soldered to the FR-4 LED circuit layer, which are used to bias the LED. The LED itself operates up to 1.8 V

Fig. 3-11: Experimental setup for the waveguide-based characterisation of the silicon.

with a 500 mA biasing current. In a similar way to the measurements up to 9 GHz, the curve-fitting of the reflection measurement was carried out in the on-state and the off-state.

The results presented in Fig. 3-10 show the differences between the active and the off-state of the silicon. By fixing all other parameters of the CST simulation model, it is possible to match the simulation and measurement results, using only the conductivity values. The conductivity value extracted for the off-state was 5 S/m, while for the active state it was 80 S/m. Results above 35 GHz are not considered to

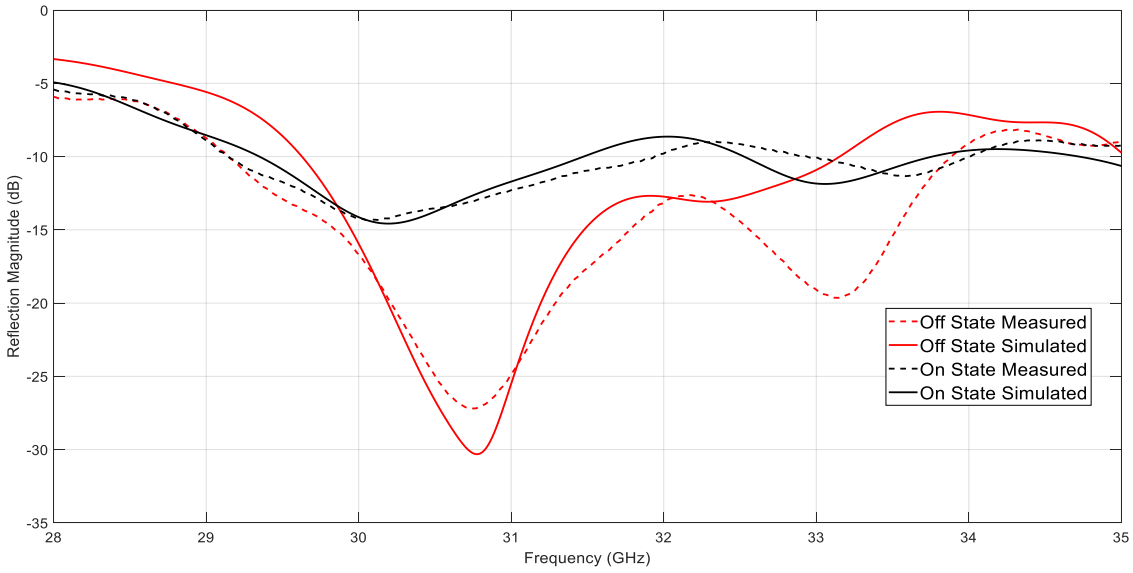

Fig. 3-10: Simulated and measured results for the silicon in its on and off states, using parametric sweeps to match the conductivity values.

be accurate due to the calibration of the PNA-X at the highest frequencies of the Ka-Band. However, the results in Fig. 3-10 show the excellent agreement achieved between simulation and measurement results, allowing the figures for the conductivity to be taken through the simulation –measurement matching process.

During the curve-fitting process, it was noted that the original design had a similar profile to that which is presented in Fig. 3-10, but the main resonance was at a higher frequency. When fabricated, the air-gaps between the layers caused the main resonance to appear at a lower frequency of 31 GHz. This was seen by adding small air-gaps (0.02mm) to the simulation model presented in Fig. 3-9. This should be considered when fabricating the unit-cell for the reflectarray and the final design, as these air-gaps will potentially cause a frequency shift.

It is clear that while the surface-mount IR-LED is a much more practical package, the maximum radiant intensity which is achievable from this device is much smaller than that of the traditionally packaged IR-LED used initially. This is shown in that the conductivity level which is reached is only 80 S/m. However, this is achieved with a single LED in a system operating at Ka-band, showing that the results are still promising for a Ka-band reconfigurable system. Furthermore, the compact size of the surface-mount LED means that it can be integrated with millimeter-wave arrays with ease, and placed close to the silicon layer for optimum illumination efficiency.

3.5 Summary

The use of silicon as an optically reconfigurable semiconductor is a proven concept, however this characterisation has further developed the feasibility of this reconfiguration method. Rather than using the traditional methods of laser or lens based illumination, this work has focused around a method of illumination which can be readily integrated in array antennas. The low-cost and compact size of the LEDs, combined with recent advances in terms of their output power now allows for a much more compact illumination source, albeit with less directionality. The initial experiments comparing an array of IR-LEDs to a traditional laser source have shown that there is a trade-off between the two sources. Although laser-based sources

provide better performance, the cost and size of these is significantly higher than the IR-LEDs, making the latter easier to integrate into designs.

Following this work, the physical properties of the silicon under this type of illumination were characterised. This was necessary as this type of illumination has not been used previously in designs up to Ka-band. A simulation-measurement matching technique was used to extract the performance of silicon, first using transmission line methods, followed by a waveguide method, which was more applicable at higher frequencies due to improved fabrication. Accurate CST simulation models were designed, and parameter sweeps of the silicon allowed the properties of the conductive plasma and its overall depth to be extracted.

The results show that this illumination type is applicable to applications in the lower millimeter-wave bands, and with the known physical properties of the silicon, it is possible to make use of the silicon in the reflectarray designs going forward.

Chapter 4:

Design of an Optically Reconfigurable Reflectarray

4.1 Introduction

Reflectarrays and phased arrays have already been introduced in the previous sections. It is common that the excitation phase or the reflection phase in the case of the reflectarray can be adjusted to provide the system with beam steering functionality. The techniques for this were covered in detail in Chapter 2: showing both discrete and continuous tuning methods for providing the required reconfiguration.

In addition to adjusting the reflection phase, the second parameter which was seen to be controlled is that of the amplitude of the reflected signal from each unit-cell. The amplitude of the reflection from each cell is predominately determined by the feed amplitude and the way in which the array is illuminated. However, by adjusting the reflection amplitude of each individual reflectarray element, it is possible to perform pattern synthesis, as seen in [65], [66]. This moves away from the traditional phase-only approach, providing a means for those applications which may stipulate the need for shaped beams, null control and contoured beams.

Achieving an amplitude-only or an amplitude and phase reconfigurable design requires the development of novel unit-cells, as undertaken in this chapter. This chapter focusses on the design of an optically reconfigurable reflectarray, making use of the characterisation parameters from the previous chapter. The design process begins at the numerical model, used primarily for its fast computation time and accurate results. Following this, an optically reconfigurable unit-cell is designed, in which the amplitude of the reflection magnitude can be changed using an IR-LED based approach with an integrated silicon layer. The use of an LED driver chip for the IR-LED control forced further modification to the individual unit-cell, which is then adapted into a 'quad-unit-cell'. This is then integrated into a full reflectarray design, illuminated by a feed horn, including the ancillaries for the array to operate.

4.2 Numerical model of a reconfigurable reflectarray

The design procedure for a reflectarray typically begins with a numerical model of the reflectarray itself. This numerical model is necessary to model the required phase response for each element to form the highly directive beam in the farfield, as described in Section 2.3.3. The reflected wave must be in equi-phase for a specific angular direction, which is achieved by incorporating a determined phase delay to each element to compensate for the individual elements' respective time delays resulting from their distance from the feed horn. In the case where the feed horn is located directly above the central element of the reflecting surface, the time delay will be the least, while those at the edges will have the highest time delay, which is accounted for by applying a certain phase shift to each element.

Calculation of this phase shift relies on the reflectarray geometry as shown in Fig. 2-4. By considering the Euclidian distance from each array element to the phase centre of the feed horn, $d_{m,n}$ the x and y co-ordinates of each element $x_{m,n}$ and $y_{m,n}$ the desired pointing directions for the main reflected beam θ_b, φ_b, the phase delay for each element can be calculated as in [12]:

$$\emptyset_{m,n} = k_0(d_{m,n} - (x_{m,n}\cos\varphi_b + y_{m,n}\sin\varphi_b)\sin\theta_b, \qquad (4\text{-}1)$$

where k_0 is the free space propagation constant.

The required phase distribution calculation is followed by ascertaining the radiation patterns for the M x N array. This is achieved by a modification of conventional array theory as presented in [1]. For this approach, both the feed and element patterns are modelled as cosine q functions and the distance and angle of the feed horn with respect to the elements is considered. The phase delay, as calculated in equation (4-1) is also included in the calculation. The formulation of the radiation pattern as presented in [103] is modified to include a varying amplitude distribution, $A_{m,n}$. This allows the magnitude of the reflection from each element to be adjusted, which can provide changes to the beam shape, including sidelobe manipulation. The scalar approximation of the radiation pattern can therefore be shown as:

$$E(\theta,\varphi) = \sum_{m=1}^{M}\sum_{n=1}^{N}\left(A_{m,n}\cos^{q_e}\theta\frac{\cos^{q_e}\theta_f(m,n)}{d_{m,n}}\right) \times \left(e^{-jk_0(d_{m,n}-r_{m,n}\hat{u})}A_{m,n}\cos^{q_e}\theta_e(m,n)e^{j\emptyset_{m,n}}\right), \quad (4\text{-}2)$$

$$\hat{u} = \hat{x}\sin\theta\cos\varphi + \hat{y}\sin\theta\sin\varphi + \hat{z}\cos\theta,$$

where θ_f is the angle of the feed, θ_e defines the angle of the feed to the element and q_e and q_f are the feed and element powers respectively. The distance from the centre of the reflectarray to the individual element is defined as $r_{m,n.}$

The modification to equation 4-2 can be justified by considering the individual parts of the equation itself. It is formed of an element pattern vector function and an element excitation vector function, which is caused by the illumination of the feed horn. Therefore, the addition of an amplitude coefficient can be considered as part of

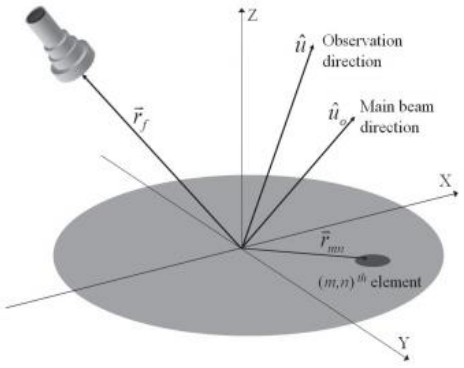

Fig. 4-1: Diagram of the reflectarray geometry, reproduced from [103]

the element pattern vector function. More specifically, a scalar multiplication value can be placed before the cosine q models for each element.

The phase delay needed for each element of a 12 x 12 array at 31 GHz is calculated first using a MATLAB script and is shown in Fig. 4-2. In this case, the horn is located at 150 mm from the array surface using a broadside illumination. This is the most basic case of the reflectarray design but serves as a good starting point for determining both the required properties of the reflectarray unit-cells along with the predicted performance of the array. A 12 x 12 array was chosen due to this size being large enough to show the effect of an amplitude distribution, whilst also not being too large to fabricate practically. The phase distribution calculated in Fig. 4-2 is used as $\emptyset_{m,n}$ in equation (4-2). This shows that the basic phase requirement for each unit-cell is to be able to alter the reflection phase from 0° to around 90° due to the small size of the array. The feed horn is located at 150 mm from the centre of the reflectarray, which is determined by the desired focal point of the reflectarray.

Although [103] presents a number of methods for calculating the radiation pattern, the array theory method used here (Eq 4-2) is the least computationally intensive and is the most straightforward to implement. MathCAD software [104] is

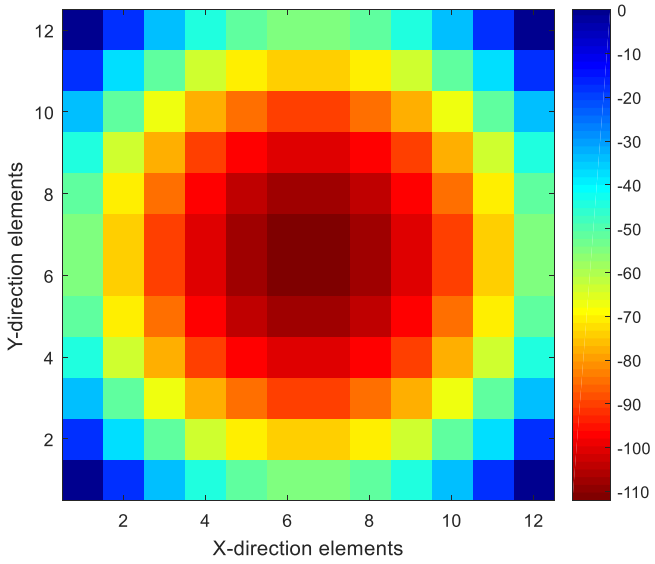

Fig. 4-2: Phase delay requirements for a 12 x 12 reflectarray at 31 GHz, with a horn located 150 mm from the surface

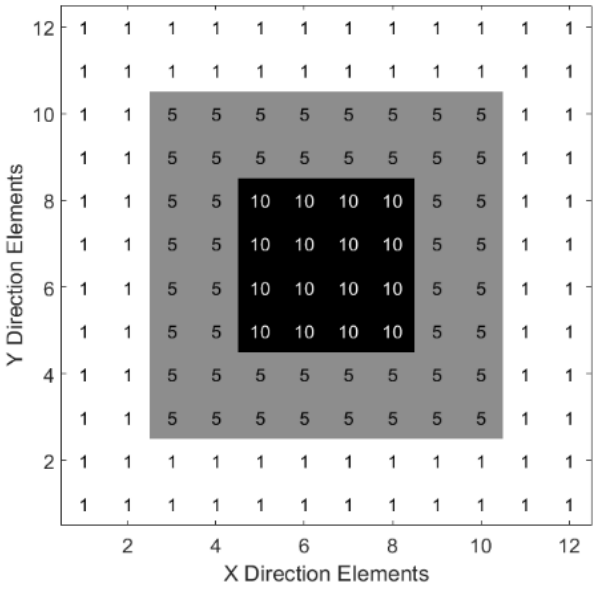

Fig. 4-3: Illustration of how the binomial distribution is spread across the array to control the amplitude.

used to calculate the radiation pattern predicted from the reflectarray. Initially, a uniform amplitude distribution is used for the $A_{m,n}$ parameter. The result of this calculation is shown in Fig. 4-4 as the solid trace. To test the effectiveness of an amplitude taper on a reflectarray of this size, a binomial distribution with an expansion coefficient of 5 is applied across the reflectarray. This was chosen as there are large differences between the values which will be more effective on a small reflectarray. This is spread across the array surface in a configuration which is shown in Fig. 4-3. Although a larger value for the expansion coefficient would result in a more effective sidelobe manipulation, the number that is possible is limited by the predicted tuning capability of the silicon itself. A coefficient of 5 is suitable for significant sidelobe reduction as presented in Fig. 4-4 as the dotted trace.

The results show a reduction of the sidelobe magnitude of 20 dB, despite a broadening of the mainlobe is visible. Enabling this type of reconfiguration is possible using the proposed reconfiguration mechanism. The basis of the unit-cell which can provide this level of reconfiguration is the characterisation cell from section 3.4.2.

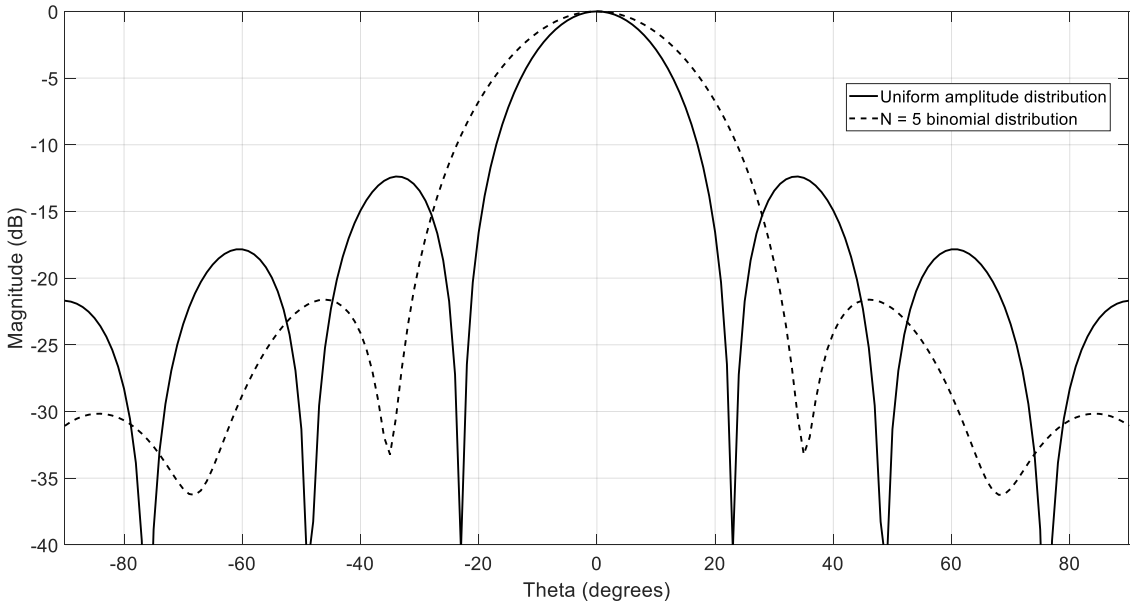

Fig. 4-4: Radiation pattern comparison between a uniform amplitude distribution applied to the reflectarray elements and an *N*=5 binomial distribution.

4.3 Design of the unit-cell

The initially proposed unit-cell has a similar multilayer structure to that which is used to characterize the silicon. They differ in that the silicon piece used in the unit-cell covers the whole area of the unit-cell. Additionally, a layer is included on the top surface, above, which forms the reflective surface. This layer is fabricated with the use of conductive silver ink, printed onto a polyethylene terephthalate (PET) substrate by a Diamatix Materials Printer (DMP-2831) which is able to print using a variety of metallic inks. The PET itself has a dielectric constant of 3.2 and a loss tangent of 0.022 at 10 GHz [105]. The thickness of the PET is 0.1 mm. Initially copper ink was used to print a grating design onto the PET, but the particle size and the conductivity of the ink was too low resulting in a low-quality print seen in Fig. 4-5(a). As a result, silver ink was used to print the grating structure, with a more accurate result (Fig. 4-5 (b)).

This grating structure is used to enable the illuminating radiation from the feed horn to reach the silicon layer, while also providing a certain level of reflection as required by the reflectarray. Furthermore, variations in the overall size of the grating provide the mechanism by which the phase distribution of Fig. 4-2 can be achieved.

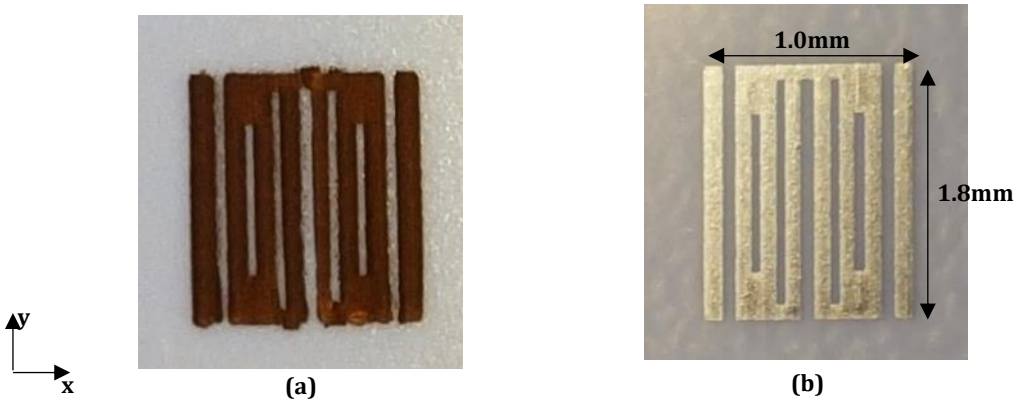

Fig. 4-5: (a) Inkjet printed grating using copper ink (b) grating printed using silver ink.

The use of inkjet printing adds further flexibility to the design. This layer can easily be removed and replaced, allowing multiple phase distribution to be applied rapidly.

This particular design was developed by adding slots to a square patch, which is the most basic form of a reflectarray unit-cell. The slots were initially of a single uniform length, but through parametric variations, it was discovered that a slightly wider bandwidth could be achieved with multiple slot sizes, without affecting the reflection magnitude significantly. The reflection phase can be adjusted by modifying the y-dimension of the grating, which is referred to as the scaling factor.

The simulation model for the unit-cell is shown in Fig. 4-6 (a,b) showing the layer structure used. Below the PET layer with the printed grating, a Rogers RT Duroid 5880 layer (thickness: 0.1016mm; dielectric constant of 2.2; loss tangent of 0.002) again provides a protective layer preventing damage to the silicon layer below it. The copper is removed from both sides of the substrate using a copper sulphate solution. Below this, the silicon layer is modelled using the parameters determined during the characterisation process. The plasma layer is modelled as a separate material, with a variable conductivity, and has dimensions which match those of the cavity (1.6 mm x 1.2 mm). This is because it is envisaged that the plasma layer will only exist directly above the LED rather than spreading throughout the silicon. The same LED as was used in section 3.4.2 is used, the Osram SFH 4710 [101].

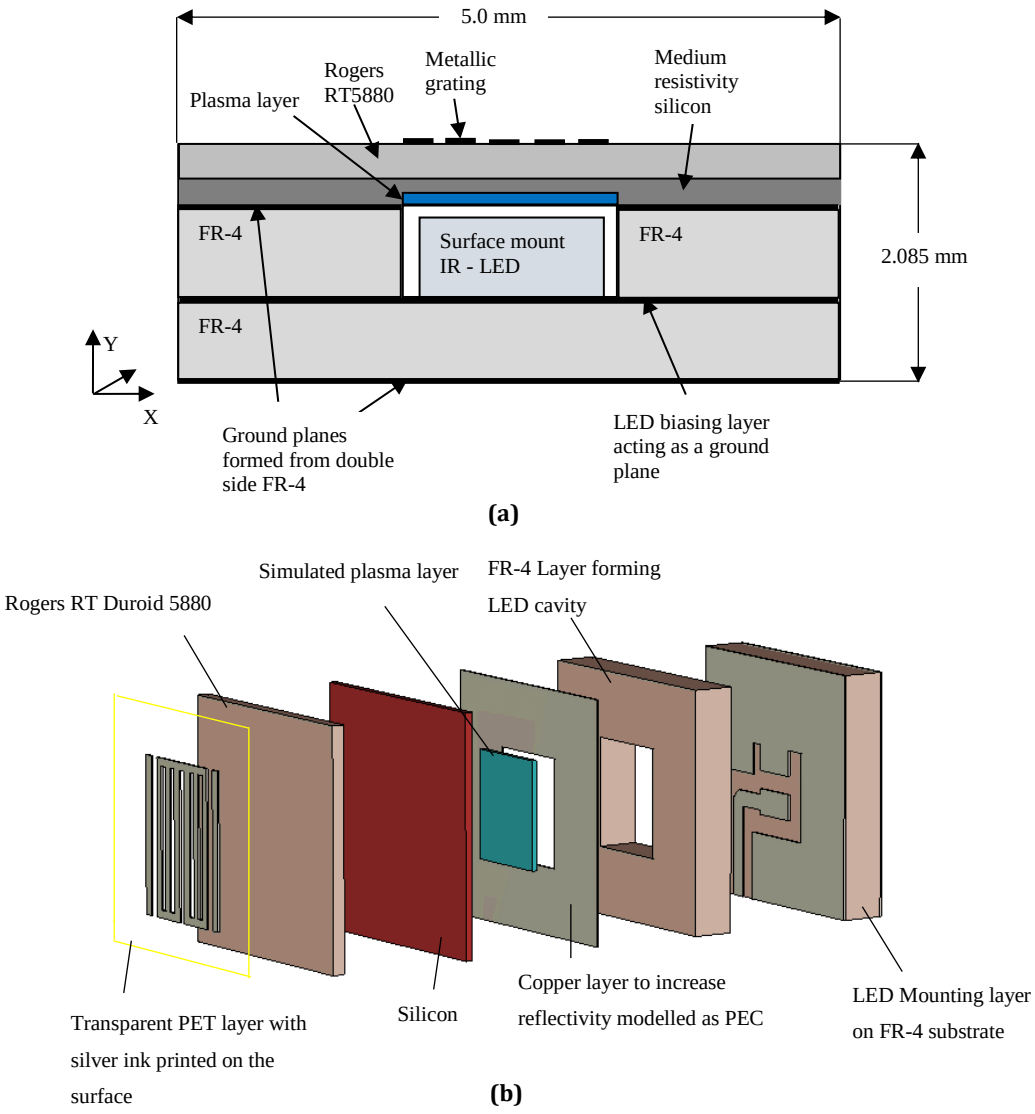

Fig. 4-6: Visual aspects of the initial unit-cell design showing (a) the cross-sectional view (b) exploded view of the simulation model.

The LED itself is mounted on the lowest layer of FR-4, with as minimal biasing circuitry as possible, and is then enclosed by the layer of FR-4 above it forming a cavity. The LED is again not modelled in CST due to the difficulty in assigning the appropriate material parameters to it.

This unit-cell is simulated using the infinite array approach in CST microwave studio. This simulates the properties of the unit-cell accurately, including mutual coupling effects, without requiring the time-consuming simulation of the full array.

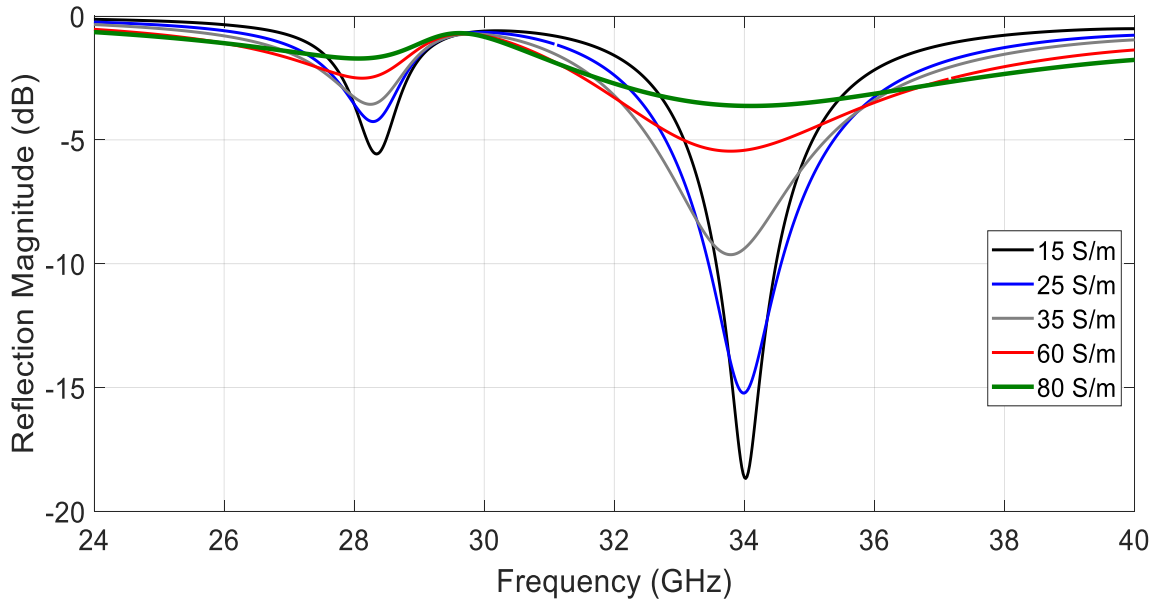

Fig. 4-7: Reflection magnitude variation across a range of conductivities.

The array was simulated to ascertain its reflection response with changing conductivity in the Ka-band and the results are presented in Fig. 4-7. The results show a good range of magnitude variation at 34 GHz, with the off-state of the silicon significantly attenuating the incident signal. In the maximum conductivity state (80 S/m) the reflection magnitude is approximately 3.75 dB. Although this is quite high for traditional reflectarrays, this particular configuration suffers from a trade-off between the reconfigurability of the silicon and the reflectivity of the cell. More specifically, if the slot sizes of the grating are reduced to increase the reflection magnitude of the cell, the range of reflection magnitude change with conductivity is reduced. The first resonance at 28.5 GHz, caused by the LED cavity, is not used as this has significantly less variation than the resonance at 34 GHz.

This design was simulated with the main resonance at 34 GHz, while it is expected that the air-gaps between the layers, and uncertainty in the FR-4 model in Ka-band, will cause the frequency to shift to a lower frequency when fabricated. These air-gaps were not included in the simulated design as they cannot be predicted accurately. Although in the ideal case, the design should be simulated at 31 GHz, where there is largest amount of deviation in the on and off state, the small uncertainties which are

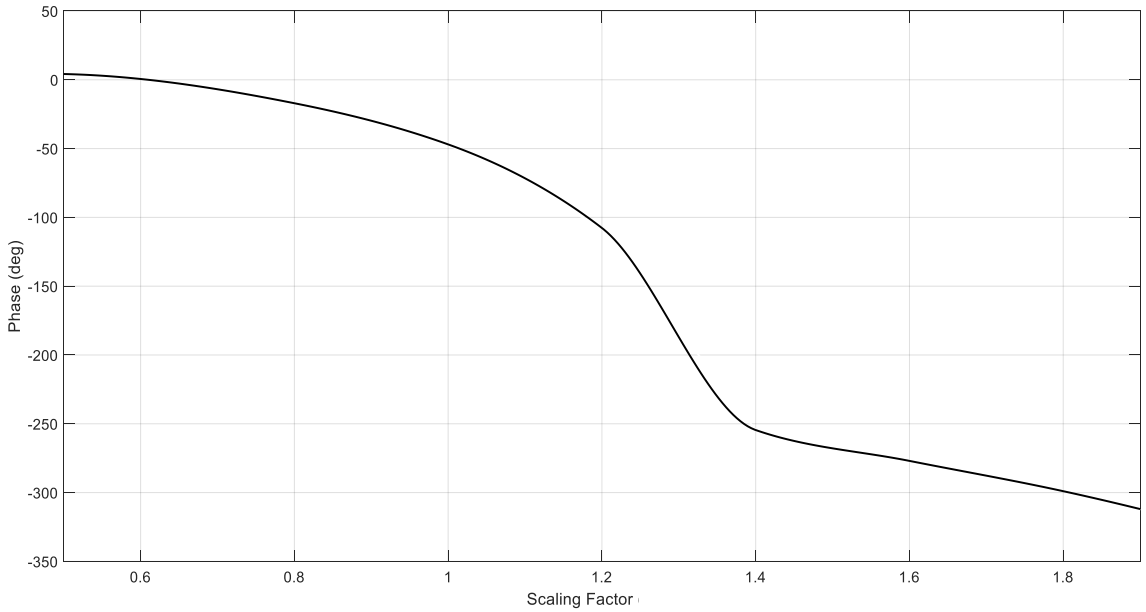

Fig. 4-8: Phase response for linear scaling of the y-dimension at 31 GHz.

present between the simulated model and the fabricated device, could cause the unit-cell to not resonate in a frequency band which has a large amount of deviation .

Aside from the reflection magnitude variation with respect to the conductivity, the phase response is a second important factor in reflectarray design. In this design, the adjustment of both the phase and the amplitude of the reflection would be extremely challenging using the conductivity as the single reconfiguration mechanism. Therefore, to achieve the phase response of Fig. 4-2 the overall dimensions of the grating are adjusted. This then stipulates the second requirement of the unit-cell, in that the phase response must remain constant with the adjustment of the conductivity, and must only change based on the size variations of the grating itself.

The phase response is simulated for linear variation in the scaling factor (y-dimension of the grating) in Fig. 4-8, and highlights the ability of this cell to adjust the phase response over the required 0 to 100 degree range required by the phase distribution from Fig. 4-2.

4.4 Measurement of the unit-cell

The simulation results presented show that the unit-cell provides the necessary responses to function as part of a reflectarray antenna. However, it is important to test the cell itself as a fabricated device prior to the design and manufacture of the full reflectarray. To do this, the previous characterisation device was used, which

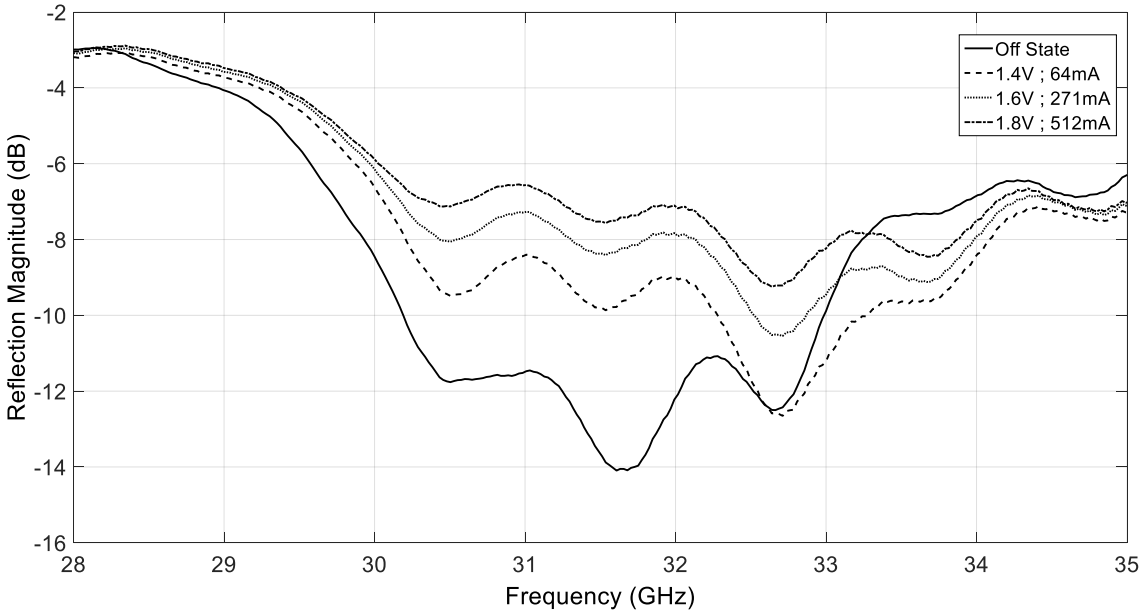

Fig. 4-9: Reflection magnitude response of the characterisation cell to different LED illumination intensities with the PET grating in place.

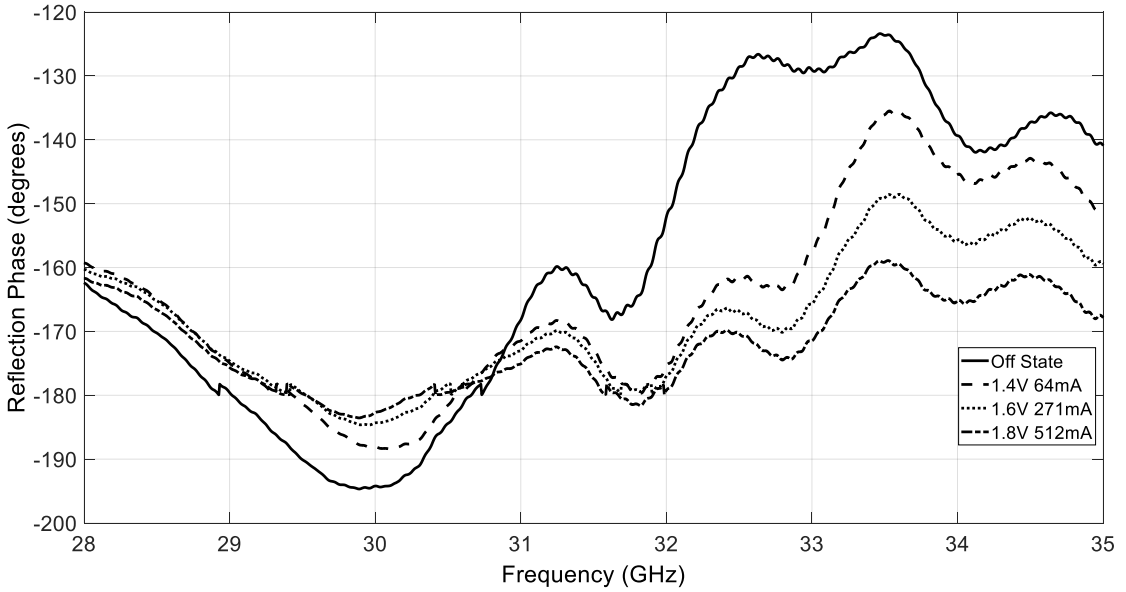

Fig. 4-10: Reflection phase response of the cell for different illumination intensities with the PET grating in place.

provides a system for characterisation the response with the grating in place. The PET grating layer was added above the Rogers RT Duroid layer of the characterisation cell which was shown in Fig. 3-9. In the simulation model, the PET substrate layer was not included, as it was envisaged to have very little effect on the properties of the reflection magnitude and phase, but would enforce a large increase in the number of mesh cells required for the simulation, increasing the time for the simulation.

The LED was supplied with a range of voltages, from its off-state to 1.8 V, 512 mA, which controls the illumination power of the IR-LED. The reflection of the cell was measured using a PNA-X, calibrated with a waveguide calibration kit. The reflection phase and reflection magnitude responses to the different LED illumination intensities are shown in Fig. 4-9 and Fig. 4-10 respectively.

It can also be seen in the results that the frequency at which the design operates at has moved to 31 GHz, which was anticipated due to the air gaps which exist between the layers, and the uncertainties which are caused by the unknown properties of the FR-4 materials at these higher frequencies.

The results presented highlight a high level of deviation for the reflection magnitude, across a relatively large bandwidth. More precisely, between on and off states, the maximum deviation is 7 dB. Furthermore, with each increase in voltage, the reflection magnitude increases by at least 1 dB, with the largest increase occurring between the off-state and 1.4 V. The amount of variation decreases as the power of LED reaches its maximum at 1.8 V and 512 mA. As previously mentioned, the reflection phase of this unit-cell should be independent of the illumination intensity of the LED, allowing the phase to be controlled only by the scaling factor of the grating. Fig. 4-10 demonstrates that very little phase deviation is present with respect to illumination intensity, particularly at around 30.7 GHz. Provided that the design is at this frequency, the phase response of the unit-cell will be very predictable, will only be affected by the aforementioned scaling factor.

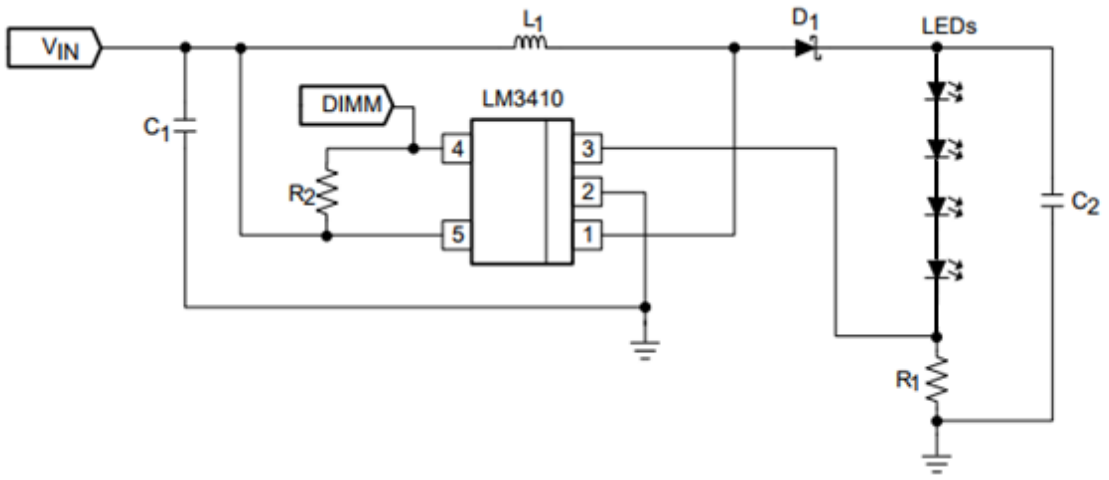

Fig. 4-11: Circuit schematic used for each quad-unit-cell, reproduced with minor changes from [105].

4.5 Development of the quad-unit-cell

During the measurement of a single grating and during the characterisation of the silicon, the IR-LED is biased directly from a DC power supply at varying voltages to adjust the brightness. However, in practice this will not be possible in a full array as each LED needs to be individually driven. Furthermore, the LEDs need to be supplied with a controlled current and voltage to ensure they do not overheat. To facilitate this, an LED driver chip is used which uses pulse width modulation (PWM) to control the LED brightness. For this design a TI LM3410 [106] LED driver chip is used due to its overall compact form-factor and limited external circuitry.

Despite the compact overall dimensions of the chip with its biasing circuitry, changes to the design of the full reflectarray were required to accommodate these. More precisely, each LED driver chip is used to control four of the IR-LEDs in series across four individual unit-cells. These four combined cells are known hereafter as a "quad-unit-cell" which has dimensions of 10.0 x 10.0 mm. The four LEDs are driven in series rather than in parallel, as the current for each cell would reach up to 2A per cell in this case. By driving four LEDs in series, the maximum current per quad-unit-cell remains at 500 mA, while the voltage increases to 7.2 V.

The schematic which is used is for each quad-unit-cell is shown in Fig. 4-11. The input capacitor, C1, is used to ensure a smooth input voltage to the chip while the

Table 4-1: Values for the components of the quad-unit-cell.

Designation	Component	Value
C1	Capacitor	10 uF
C2	Capacitor	2.2 uF
D1	Diode	$V_f = 0.43$ V, $I_f = 500$ mA, $V_R = 30$ V
R1	Resistor	4.02 Ω
R2	Resistor	100 kΩ
L1	Inductor	10 uH

output capacitor, C2, is used for a similar purpose in addition to smoothing any noise caused by switching. The inductor (L1) determines the input ripple current. Larger value inductors decrease the ripple current but have larger dimensions. The resistor, R1, is a current sense resistor, and is determined by the internal feedback of the amplifier in the LM3410 chip. The value of this resistor determines the magnitude of the current through each LED. R2 is used to prevent the input dimming pin from floating. Finally, the diode is used to conduct during switch off time of the chip. The component values are provided in Table 4-1.

The sense resistor value used is conservative for the initial tests, as, based on the V_{FB} (feedback voltage) value of 0.19 V, the current through each quad-unit-cell will only be 47 mA. This therefore limits the maximum brightness of the LEDs, but ensures that for the initial tests the IR-LEDs are not damaged by high current levels. The sense resistor (R1) can then be reduced down to a value of 0.68Ω, increasing the current to 500 mA.

Due to the size restrictions of the quad-unit-cell, the layout of the circuit was completed using Keysight ADS software, which allowed for a custom layout to be drawn easily. This was only feasible due to the low number of components. Furthermore, it enabled the incorporation of the pads for off-board connectors and connections to adjacent unit-cells.

The layout of the quad-unit-cell driver layer is provided in Fig. 4-12, showing the lowest layer containing the driver chip biasing circuit, while vias connect to an upper layer upon which the LEDs themselves are mounted. Each quad-unit-cell is supplied

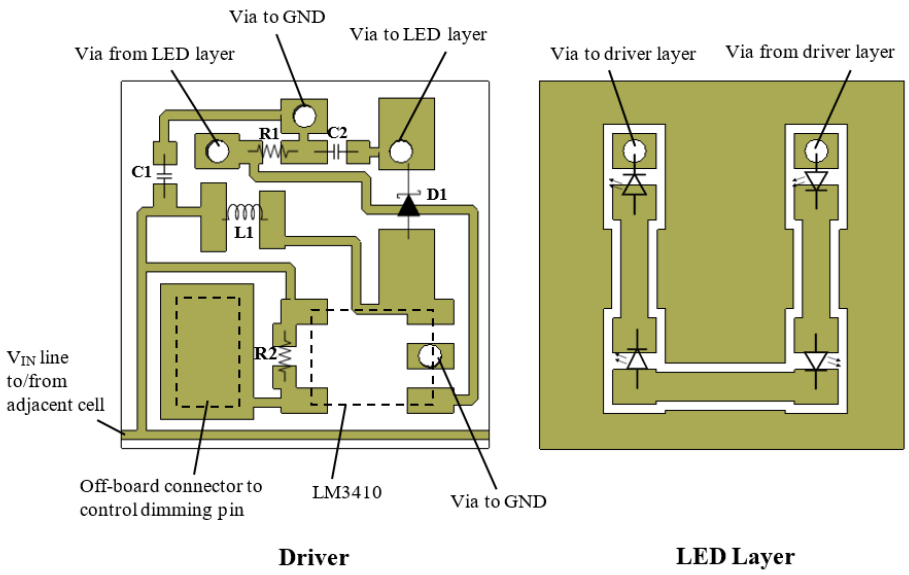

Fig. 4-12: Layout of the driver and LED layer of the quad-unit-cell.

through the V_{IN} line which makes each quad-unit-cell connected in parallel to each other. Therefore, the maximum current requirement of the array is predicted to be a maximum of 18 A for a 144-element array (36 quad-unit-cells × 500 mA per cell) while the voltage supply will need to supply 5V to power each quad-unit-cell. However, this current requirement can be reduced if a circular reflectarray, with fewer elements, is used. Although connecting each quad-unit-cell in parallel increases the current draw of the overall reflectarray, it prevents complete failure of the array if a single quad-unit-cell malfunctions.

These specifications are within the power supply rating of a standard PC power supply unit, which allows for a low-cost method for powering the reflectarray. However, it must be noted that this level of current is likely to require quite high heat dissipation meaning that the cooling of the reflectarray is critical for its long-term performance. The incorporation of a cooling system for the array is therefore considered in the full reflectarray design.

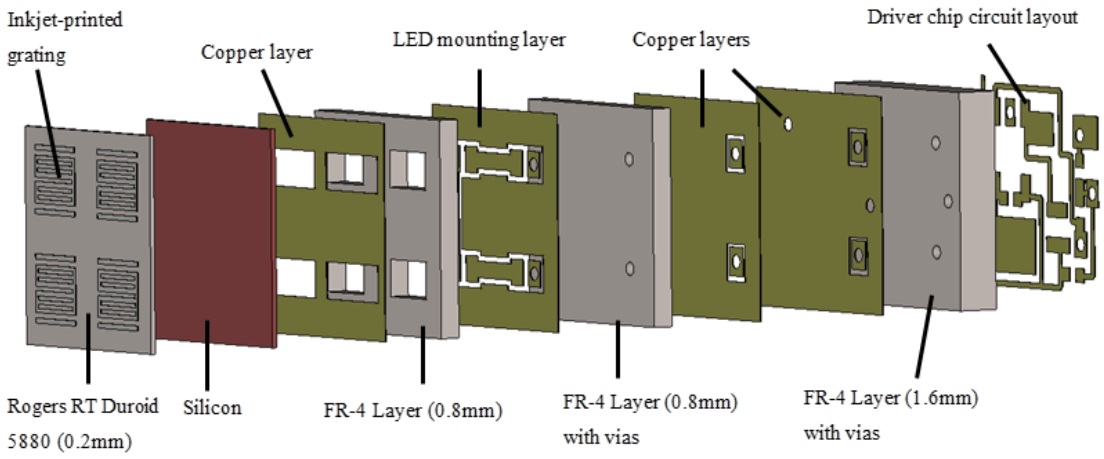

Fig. 4-13: Exploded view of the quad-unit-cell used for the full reflectarray design.

Aside from the aforementioned layers, the quad-unit-cell layer structure is largely similar to the structures presented in sections 3.4.2 and 4.3. The simulated model is shown in Fig. 4-13, highlighting the various layers of the structure. This model was simulated using the unit-cell simulation technique in CST, using the same parameters which produced the results in Fig. 4-7 for a comparison between the single unit-cell and that of the quad-unit-cell.

The reflection response at 34 GHz for conductivity levels of 15 S/m and 80 S/m is plotted in Fig 4-13 which provides a direct comparison between the two designs of

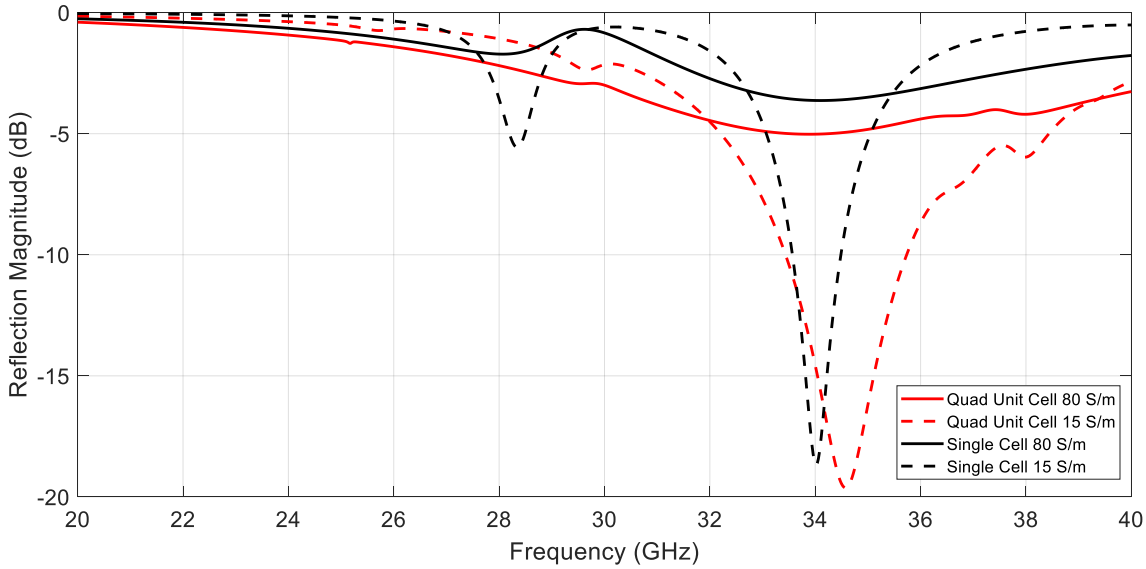

Fig. 4-14: Comparison between the response of the quad-unit-cell and the single unit cell.

the unit-cells. There are two main differences observed in the simulation results. The first is that the bandwidth is slightly wider for the quad-unit-cell than that of the single unit-cell. This is most likely caused by the increase in the number of layers [107]. However, the results also show that extra resonances are not generated, which would be the case if the biasing circuit was influencing the RF performance which means that the DC-RF isolation is sufficient. Furthermore, the packaging of each component of the driver circuit does not need to be simulated as the RF signal is not reaching the lowest layers of the circuit.

The design of the quad-unit-cell and the analysis of its performance shows that this type of unit-cell will perform well in the reflectarray itself. Again, the design was simulated for 34 GHz, to ensure that the uncertainties can in the fabricated design can be compensated. Following these unit-cell based simulations, the design of the full reflectarray can be undertaken with reasonable confidence in the simulation results as documented in the next section.

4.6 Design and simulation of the reflectarray

The unit-cell simulations provide a good approximation of how the array itself will perform, but there are certain effects which cannot be modelled using the unit-cell approach. Firstly, the use of the feeding horn is not included in the unit-cell simulation, and this is of particular interest in reflectarray simulations as it can have a detrimental effect on the performance of the array due to blocking effects[13], [55], [108]. Furthermore, the unit-cell simulation does not provide the overall radiation pattern when the phase distribution is applied or when the amplitude tapering is applied to the array. For this reason, the full reflectarray is simulated using a full-wave solver, which although time consuming provides the most accurate view of the performance of the array prior to fabrication. The subsequent sections detail the various aspects which should be considered when designing the full reflectarray, including the shape of the array, and the location and fixing of the feedhorn.

4.6.1 Circular and rectangular arrays

Reflectarray designs are often either rectangular or circular, with the latter being chosen for this design. This was chosen firstly for the reason that silicon wafers are typically circular in construction, so this would mean that cutting and potentially damaging the wafer could be avoided. Secondly, by using a circular configuration, the number of unit-cells could be reduced to 96 individual cells (24 quad-unit-cells), therefore reducing the power requirement of the array. In addition to reducing the power requirements, the cost of the array reduces along with the fabrication time. A further aspect to the choice of a circular aperture over a square design is that those elements at the corners have little impact on the radiation, particularly when the amplitude taper is applied, as seen in Fig. 4-3, where the coefficients at the edges are much lower. This would mean that these elements do not contribute as much to the radiation of the antenna as much as those in the centre of the reflectarray. The quad-unit-cells are therefore arranged in a circular fashion, as shown in Fig. 4-15 (a, b). The overall diameter of the reflectarray is 70 mm. The same layer structure as the Fig. 4-13 is followed, including the lower LED driver layer (Fig. 4-15 (b)).

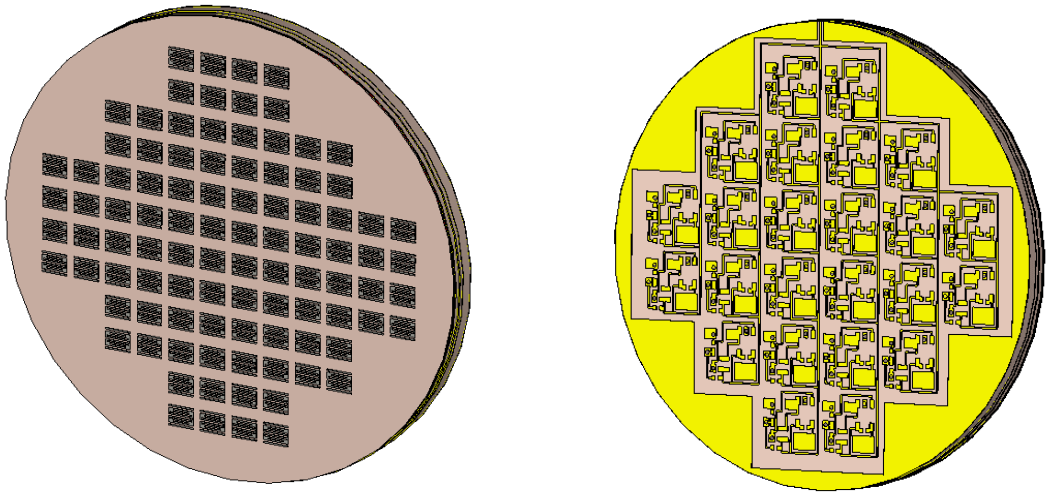

(a) **(b)**

Fig. 4-15: Configuration of the 96-element reconfigurable reflectarray (a) top view of the array (b) back view of the array.

4.6.2 The feeding mechanism

The feeding of the reflectarray is an important design aspect, and can have significant effects on the aperture efficiency of the reflectarray. In addition to this, blocking effects of the horn mounting structure and cabling cause distortion to the radiation patterns. In-depth studies of the blocking effects in centre-fed reflectarrays have already been carried out [108] highlighting that the feeding structure, which is often not included in simulations, can have significant scattering effect.

The specific location of the feed depends on the phase centre of the feed-horn and the distance at which the phase delay plot was designed for. The numerical model in this case was designed with the feed horn set at 150 mm from the centre of the array. The best method for locating the phase centre of a feed horn is outlined in [109], but modern simulation software is more than capable of this calculation to a reasonable degree of accuracy. For this reason, the horn antenna used was modelled in CST microwave studio, as shown in Fig. 4-16, which showed the phase centre to be located just inside of the taper of the horn, close to the aperture.

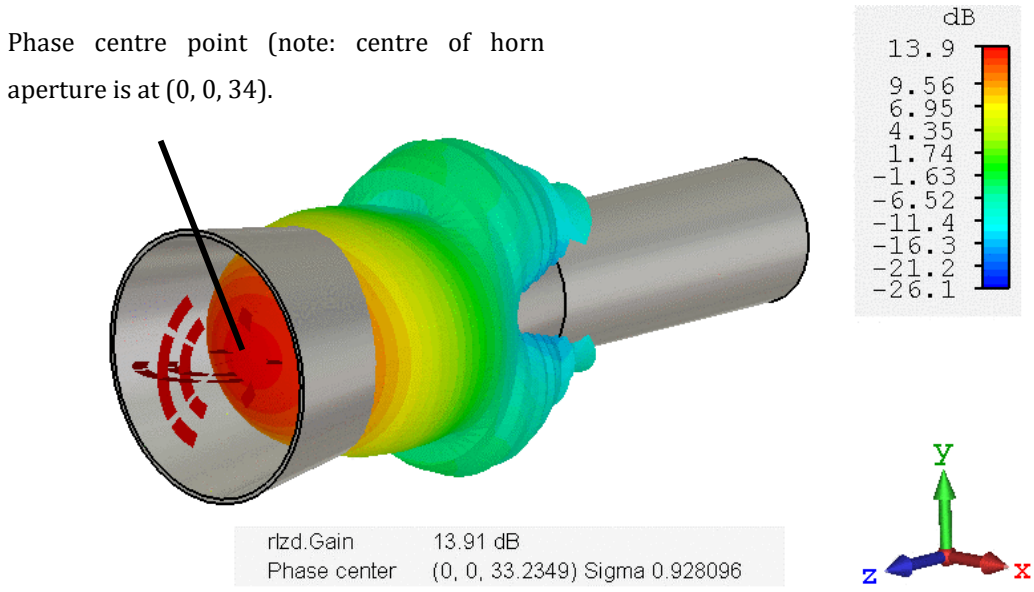

Fig. 4-16: CST model of the feed horn, showing the dimensions and the location of the phase centre.

It is anticipated that due to the use of a centre-fed horn, that there will be the potential for the feed to block the radiation of the array. This can be avoided using an offset fed design, but this will add an extra level of complication to the structure.

4.6.3 Simulation results

The phase distribution of Fig. 4-2 was implemented across the array surface using the varying unit-cell sizes. Additionally, the amplitude distribution was applied by normalising the reflection response, such that lowest reflection of the quad-unit-cell was used as a '10'. The radiation patterns for a uniform amplitude distribution (i.e. all are set to maximum reflection) and the binomial distribution are compared for both the numerical and full-wave models, with the results shown in Fig. 4-17. Initially the horn is placed in free-space above the array without its mounting structure to simplify the simulation. This enables a direct comparison to be carried out between the numerical model and the full-wave simulation.

The results show that the numerical and full-wave model predict similar responses for the reflectarray antenna in both cases of the amplitude distribution. This validates the techniques, and proves the concept of the optically reconfigurable

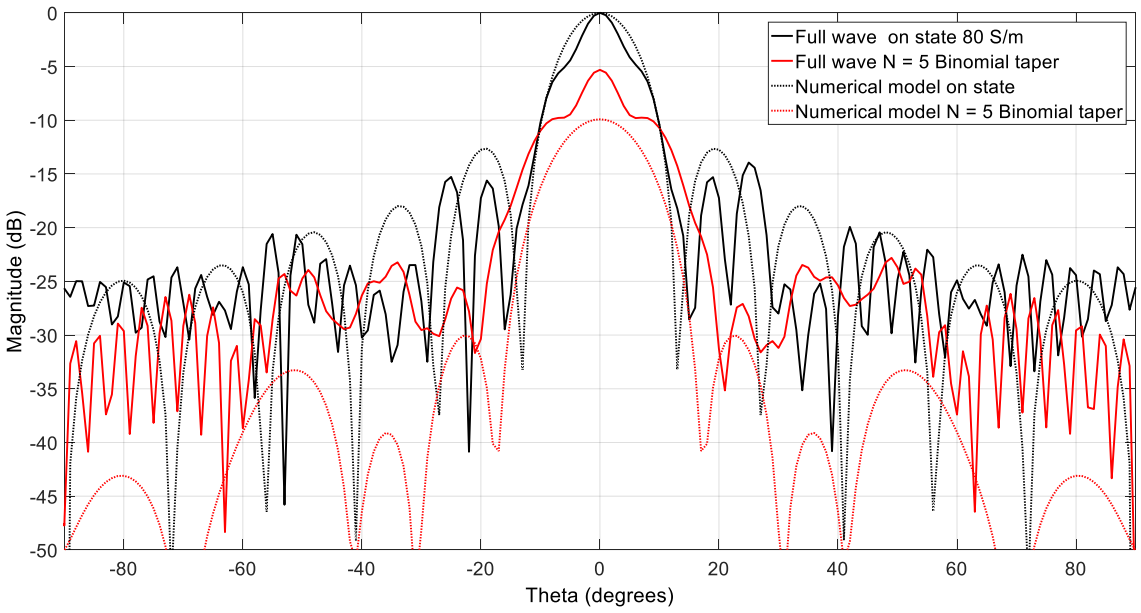

Fig. 4-17: Radiation pattern comparison between a binomial amplitude distribution and the uniform on state distribution for both full-wave and numerical models.

reflectarray. It further shows that this antenna would be a good candidate for sidelobe manipulation in satellite antennas.

The efficiency of the design is a critical section of this work, as designs which manipulate the amplitude response often suffer from poor efficiency [109]. The simulation results predict a total efficiency of 85% in the case where all the LEDs are illuminated (maximum reflection), while in the case of a binomial distribution being applied, the total 72%. The low levels of efficiency are due to the illuminated power being absorbed by the lossy plasma. However, this is a necessary trade-off for the flexibility with which the amplitude response can be adjusted.

The array simulations give an accurate depiction of how a fabricated array will operate. However, this concept can only be fully validated using a fabricated design. As was mentioned previously, the fabricated design needs to incorporate both the feed horn support and a cooling mechanism for the LED driver circuit. The feed horn support should also be adjustable to account for any fabrication inaccuracies in the array itself which may need to be compensated for.

To enable rapid fabrication and prototyping, the various fixtures should be designed to be 3-D printed. By using ABS material for the structure of this, the impact which the fixture will have on the radiation of the reflectarray will be significantly less than if metal were used. In particular, the feed horn clamp and supporting rod will be made from ABS thereby minimising interference. For cooling, a fan can be incorporated in the fixture directly below the driver layer, with consideration of the fans exhaust also included. The full structure is shown in Fig. 4-18. This full design is not simulated in CST, due to its electrically large size and the length of time that this design would take to simulate, however, these additions should not impact the performance of the reflectarray greatly.

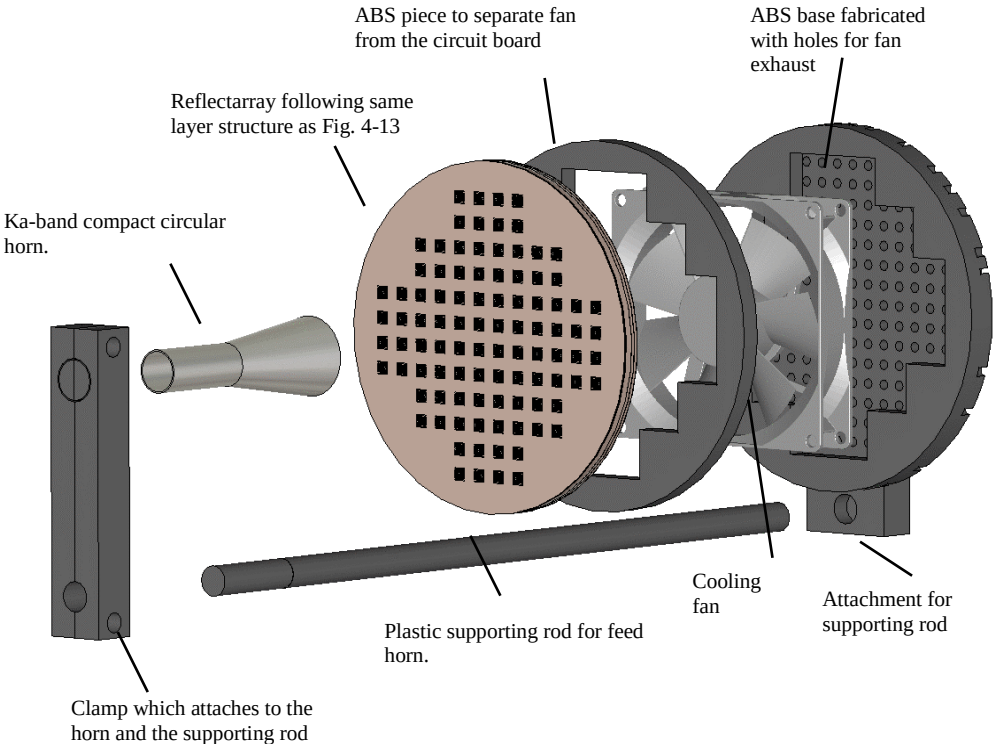

Fig. 4-18: Exploded view of the final reflectarray design.

4.7 Summary

This chapter has documented the procedure for the design of the reflectarray element. The previous chapter documented the reconfiguration mechanism, providing the values required for the design of the reflectarray unit-cell. Taking the design used for the characterisation of the silicon and making minor modifications to the layer structure, the unit-cell for the reflectarray could be designed. The unit-cell was simulated in CST using the data extracted from the characterisation process. The unit-cell is designed such that it can provide a good range of reconfiguration in terms of its reflection amplitude response. The PET grating structure is a key aspect of the design, in which it controls the phase response through its dimensions, while also allowing the cell to be reflective as stipulated by reflectarray requirements.

The unit-cell was measured using a slightly modified version of the characterisation cell used in Chapter 3. The measured results from this experiment show that the unit cell can provide the necessary reconfiguration, and there is a reasonable agreement with the simulated models.

The second phase of the unit-cell design was the development of the quad-unit-cell, which was necessary due to the biasing requirements of the IR-LED itself. Four individual unit-cells combined in a 2 x 2 array form a single quad-unit-cell which acts in a similar manner to the single unit-cell. The quad-unit-cell provides the necessary biasing to the LEDs, and allows for illumination control of the IR-LEDs.

The numerical model which was used initially highlights the advantages which can be provided by an amplitude reconfigurable reflectarray. Most notably, a significant reduction in the sidelobe level can be achieved through the application of an amplitude taper to the array. The unit-cells presented in this chapter have been designed to fulfil the requirements shown by the numerical model and this is shown by the simulation models of the full array using the quad-unit-cell design.

The final stage of the design is ensuring that the reflectarray will operate consistently when fabricated. The LED driver chips require cooling to ensure that they do not suffer damage, and a similar requirement comes from the IR-LED themselves. As a result, a cooling mechanism is incorporated into the design. Moreover, the design can make use of 3-D printing methods to allow for rapid prototyping of the various components of the array structure.

Chapter 5:

Fabrication & Measurement of an Optically Reconfigurable Reflectarray

5.1 Introduction

Although the simulations presented in the previous sections are based on measurement results of the silicon under IR-LED illumination, to fully validate the optically reconfigurable reflectarray concept, the design is fabricated and measured for its radiation properties. Initially, this chapter considers the methods by which the reflectarray can be measured and the requirements from the array itself based on these measurement techniques. It also documents the fabrication procedures used to construct the array for testing and finally provides the results of the measurements of the optically reconfigurable reflectarray.

5.2 Measurement techniques

There are a wide range of techniques available for the measurement of the reflectarray antenna. However, this chapter will predominately focus only on those which are available in the Antenna Laboratory at Queen Mary University of London (QMUL). The frequency at which this array operates limits the measurement to being

carried out using one of three techniques. The first is the use of the compact antenna test range (CATR) in its original configuration [111]. The second is to use the CATR chamber in conjunction with a spherical near-field scanner, providing both elevation and azimuth patterns. Finally, a planar near-field scanner can be used to ascertain the radiation properties of the antenna radiating at broadside. Each of these three will be considered for their structural requirements and their ease of use.

In addition to analysing these techniques, it is important to consider which techniques are most applicable to reflectarray antennas, and those techniques which have been tested previously. To do this, various reflectarrays which have been measured at different frequencies will be considered.

5.2.1 Compact Antenna Test Range (CATR)

The CATR at QMUL shown in Fig. 5-1 (a), is the largest chamber and was designed for the measurement of large antennas, in particular satellite based reflector antennas [112]. The chamber, depicted diagrammatically in Fig. 5-1 (b) consists of an illuminating horn located to the left of the antenna under test (AUT). This horn determines the operating frequency of the chamber, and should be chosen appropriately for the AUT. Furthermore, the chamber is designed to operate using corrugated illuminating horns to minimise the sidelobes and improve the cross-polar performance [111]. The horn in the feed tower can be rotated such that the E and H fields of the AUT can be measured. The feed horn is accurately aligned to illuminate the parabolic reflector located to the rear of the chamber. This reflector is manufactured to have an average surface accuracy of 8 to 15 μm, with each panel aligned using two theodolites. The reflected wave from the parabolic reflector has a 1 metre diameter quiet zone which encompasses the turntable upon which the AUT is mounted. The nominal quiet zone has minimal ripples, with a maximum peak-peak-amplitude variation of 1.0 dB. The turntable itself can rotate a full 360° in the azimuth profile, and close to 180° in elevation. This allows large antennas to be measured accurately in both profiles.

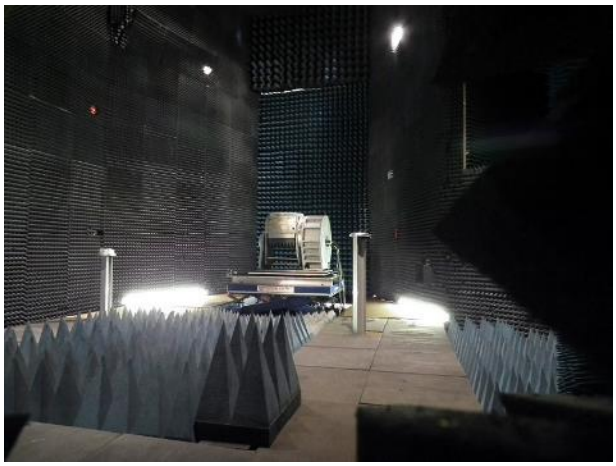

(a)

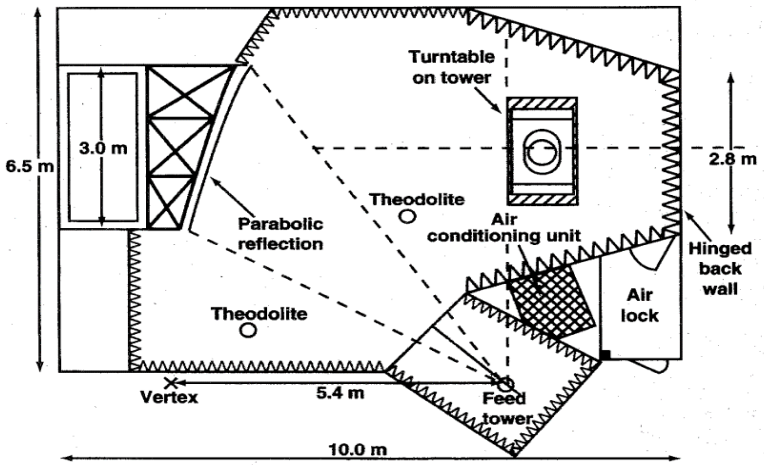

(b)

Fig. 5-1: (a) The CATR at QMUL, showing the AUT turntable (b) Diagram of the CATR taken from [112]

The main disadvantage of this system is the long acquisition time and potentially complex setup. Reconfiguration of the system from X-band to Ka-Band requires knowledge of the horn radiation pattern and precise alignment to ensure that the performance in the quiet-zone is optimal.

The main disadvantage of this system is the long acquisition time and potentially complex setup. Reconfiguration of the system from X-band to Ka-Band requires knowledge of the horn radiation pattern and precise alignment to ensure that the performance in the quiet-zone is optimal. Furthermore, the feed for a horn must travel from the feed tower to the chamber itself via a lengthy waveguide setup. At X-

band the losses of this are relatively small (around -3dB), but at Ka-band the loss of this feed is significant at around -10 dB across the Ka-band.

5.2.2 Planar near-field scanner

Near-field measurement of antennas has become increasingly popular with the development of the fast Fourier transform (FFT) and the computational capabilities of computers. Analysis of the far-field of an antenna through the measurement of its near-field radiation allows for a significantly more compact measurement range, without compromising on measurement accuracy [113].

The principle of near-field measurement relies upon the sampling of the complex data which surrounds the surface of an antenna at small distance from the AUT, and thus derive from it a similar vector field function at a large distance from the antenna [114]. In a planar rectilinear measurement setup, the AUT is kept stationary, and a near-field probe is moved in the X and Y directions, forming a sampling grid across the antenna aperture. Although other forms of planar scanning exist, including plane bipolar and plane polar, this is the configuration which available for use in QMUL. A particular advantage of planar scanning is that the AUT does not need to move allowing for a simpler measurement configuration. Furthermore, the simplicity of the measurement means that the data processing is less complex and alignment of the AUT and probe is easier than other types of near-field scanning [1]. Additionally, planar scanning is suited to antennas which have low backlobes, including reflector antennas, phased arrays and horn antennas.

The amplitude and phase sampling of the propagating near-field is sampled using a near field probe, which is typically an open-ended waveguide. This probe is moved across the antenna at a distance which is within the propagating near-field of the antenna. Samples of the magnitude and phase of the AUT's electric field tangential to the surface of the antenna are taken, and through modal expansion the total field of the antenna can be calculated. Thus, the far-field pattern can be taken through the solving of the fields at an infinite distance from the antenna.

Since the probe must move in the *x* - and *y* – axis, the probe is often mounted on a rail which can move in the required directions. The inverted T-scanner is one of the most common configurations and is what is available at QMUL. This setup, shown in Fig. 5-2 provides easy access to the AUT and the probe itself, and can be covered in absorber material to prevent multipath effects caused by any metallic objects. A positioning system is used for the control of the probe position, which itself is mounted on the vertical axis of an inverted-T shaped carriage. This vertical carriage arm moves in the *x*-axis, providing the mechanism for forming the planar grid over which the AUT can be measured.

A further advantage which can be seen from using planar scanning is that the individual unit-cells' embedded performance can be analysed [115]. Here, the individual scatters can be characterised, along with the incident field from the feed horn. Additionally, to aid with this type of characterisation using a near-field scanner, [116] present high-resolution near-field probes, which provide the ability to accurately determine the response of the unit-cells. Therefore, this does not automatically assume an infinite array and can provide an accurate measurement of

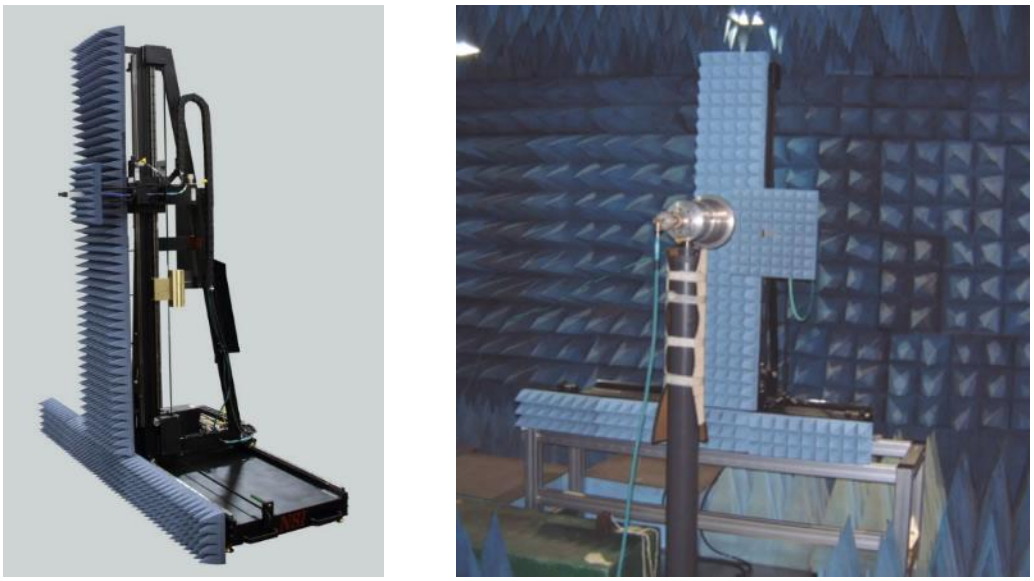

Fig. 5-2: NSI Inverted T-Scanner (Left); The scanner in place in the general purpose anechoic chamber at QMUL, measuring a 10 GHz corrugated horn (Right); taken from [122]**.**

how the individual cells perform. However, it does note that the probes must be of high-resolution, to ensure that the individual cells can be characterised.

Planar scanning is used for the measurement of the far-field results of reflectarray antennas at 120 GHz, showing its applicability even at high frequencies [117]. A corrugated horn is used in this work to illuminate the reflectarray, and a simple open-ended WR-8 waveguide is used as the measurement probe. Again, in this work, the individual elements are also analysed to view their amplitude and phase response. This proves that planar scanning is a useful technique in reflectarray measurement, and as such will be the main measurement technique used for this work.

The planar scanner at QMUL provides a useful means for measurement up to 100 GHz. The planar scanning method requires the least complex computations, but the measurement setup can be costly, and does not provide a full coverage of the AUT. To achieve full coverage of the antenna, the spherical scanning method can be used, but is the most expensive computationally and structurally. This is now possible with recent additions to the laboratory at QMUL.

5.2.3 Spherical near-field scanner

Spherical scanning is the most complete form of near-field scanning, but requires a complex measurement setup and a large amount of post-measurement computational processing to extract the far-field. However, with the use of FFTs and purpose-made software, this has become much simpler. The advantage of the spherical near-field scanning technique is that any angular cut from the antenna can be found. Unlike planar scanning, the probe remains fixed while the antenna itself is rotated using a two-axis scanner. The main drawback of spherical scanning is the overall cost of the system, and the complexity of the equations used for generating the far-field radiation pattern.

The spherical near-field scanner is a recent acquisition at QMUL, and is located inside of the CATR chamber, replacing the original configuration of the dual-reflector system. Although the scanner is initially configured for X-band operation, the system

can be setup for Ka-band operation. However, the distance from the measurement system, the PNA-X in this case, to the measurement probe is up to 12 metres. At X-band, the loss is not significant enough to impact the measurement, but at Ka-band it is necessary to include an amplifier prior to the probe itself.

Although this system would be the most optimum method for measuring the reflectarray antenna, the system is currently not in an operational state and so it is not possible to measure at this time. As a result, the best available method for measuring the reflectarray is to use the planar near-field scanning method.

Spherical scanning of a Ka-Band reflectarray is undertaken in [118] showing that this technique is one of the preferred measurement methods for reflectarray antennas. Similarly in [119], a spherical near-field scanning system is used for the measurement of a microstrip reflectarray operating in X-band. It is noted however, that there are not a significant number of reflectarray designs which are measured using a spherical scanner, which is most likely due to the expense of the measurement system itself.

5.3 Fabrication of the reflectarray

The reflectarray is designed for simple fabrication and for rapid prototyping. The structure presented in Fig. 4-18 makes use of 3-D printed structures for ease of fabrication, while the layer structure used ensures that the design can be easily modified if the prototype needs modification.

5.3.1 FR-4 layer fabrication

The first layers to be fabricated were the two lower FR-4 layers, which include the LED driver mounting layer, and the LED layer itself. These were fabricated on 0.8 mm thick FR-4 substrate using the ProtoMat M60 milling machine. Two attempts were required to fabricate the board, as the milling drill-bit was not accurate enough to etch out the circuit tracks. As a result, an RF specific milling tool provided better fabrication quality. The design includes through-hole vias for connection to the upper

layers, however the treatment of the via holes prior to the plating process was not adequate to ensure that the copper attached to the inner walls of the pre-drilled holes.

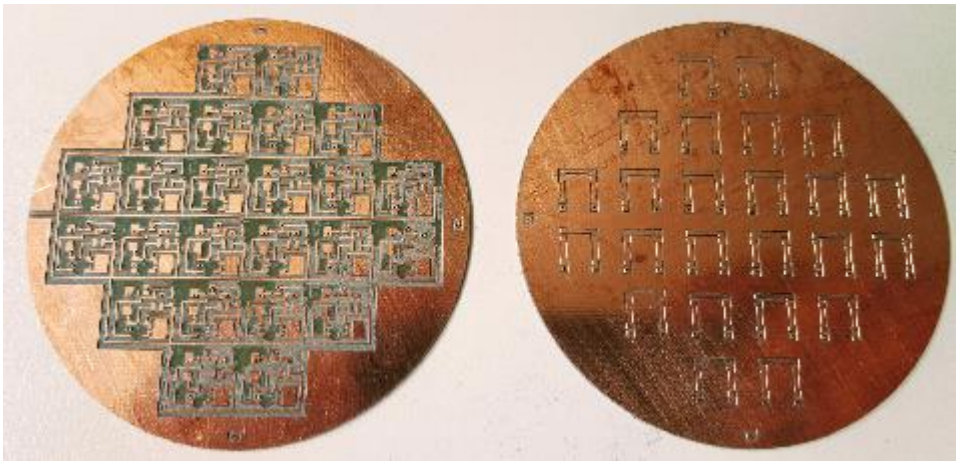

(a)

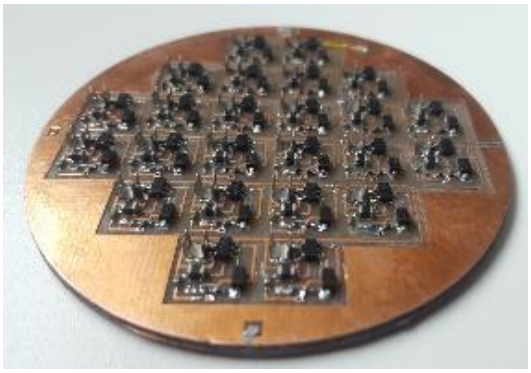

(b)

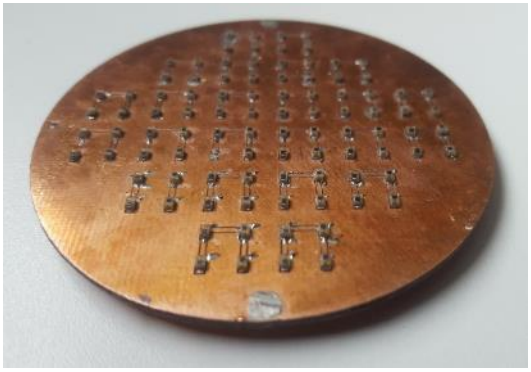

(c)

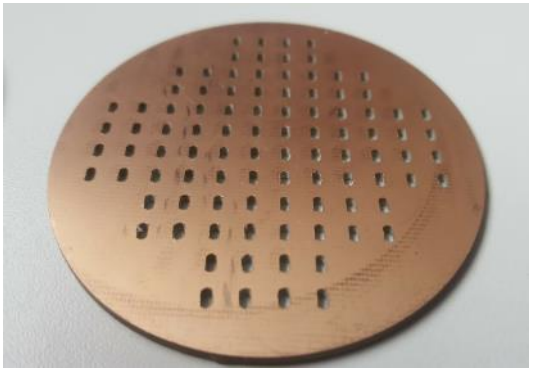

(d)

Fig. 5-3: (a) The two lowest layers of the reflectarray prior to component installation, both with a radius of 35 mm (b) the lower LED driver layer with soldered components (c) the IR-LED layer with the soldered LEDs (d) the final FR-4 layer which forms the cavity for the LED to sit in.

Therefore, to ensure a good connection through the board, thin wires were manually soldered through the holes of both boards once bonded together. At the edges of each layer, alignment holes were drilled, such that when a thin wire is inserted the two layers are accurately bonded together. The two layers shown in Fig. 5-3(a) were bonded together and the components were soldered in place using a fine-tip soldering iron, creating the structure shown in Fig. 5-3 (b, c). Each individual quad-unit-cell has an off-board connector which, when a wire is attached, will connect to the microcontroller for the LED brightness control.

Above these lower layers, a final FR-4 layer is included which encloses each LED, as shown in Fig. 5-3(d). This layer was also fabricated using the ProtoMat M60 milling machine. The difference in the colour of the board with respect to the other layers is due to the effect of the plating chemicals on the copper. Additionally, some difficulty was experienced when creating the individual holes for the LEDs, as the rounded drill bits of the milling machine do not manufacture square edges with a high level of accuracy. As a result, some manual modification of each hole was required, to ensure that the layer pictured in Fig. 5-3(d) sits flush above the preceding layers.

5.3.2 3-D printed layers

The array design makes use of 3-D printing to ensure that the structure can be rapidly fabricated and changed quickly in the event that the design needs modification. The material used was ABS, and the printer used for the fabrication was a RoVa 3D printer [120]. 3-D printers have a myriad of parameters which can have an impact on the quality of the fabrication. In this case, only a single extruder was used, despite the printer having the capability to print 5 separate materials. One of the most important parameters to adjust is the interior structure of the object being printed, as this has an impact on the fabrication time and the strength of the object. In this case, a honeycomb structure was used which allows the design to be fabricated quite rapidly without sacrificing the strength of the printed item. The settings of the printer were modified using a trial-and-error process, and once these settings were established, the various structures for the array test fixture could be fabricated.

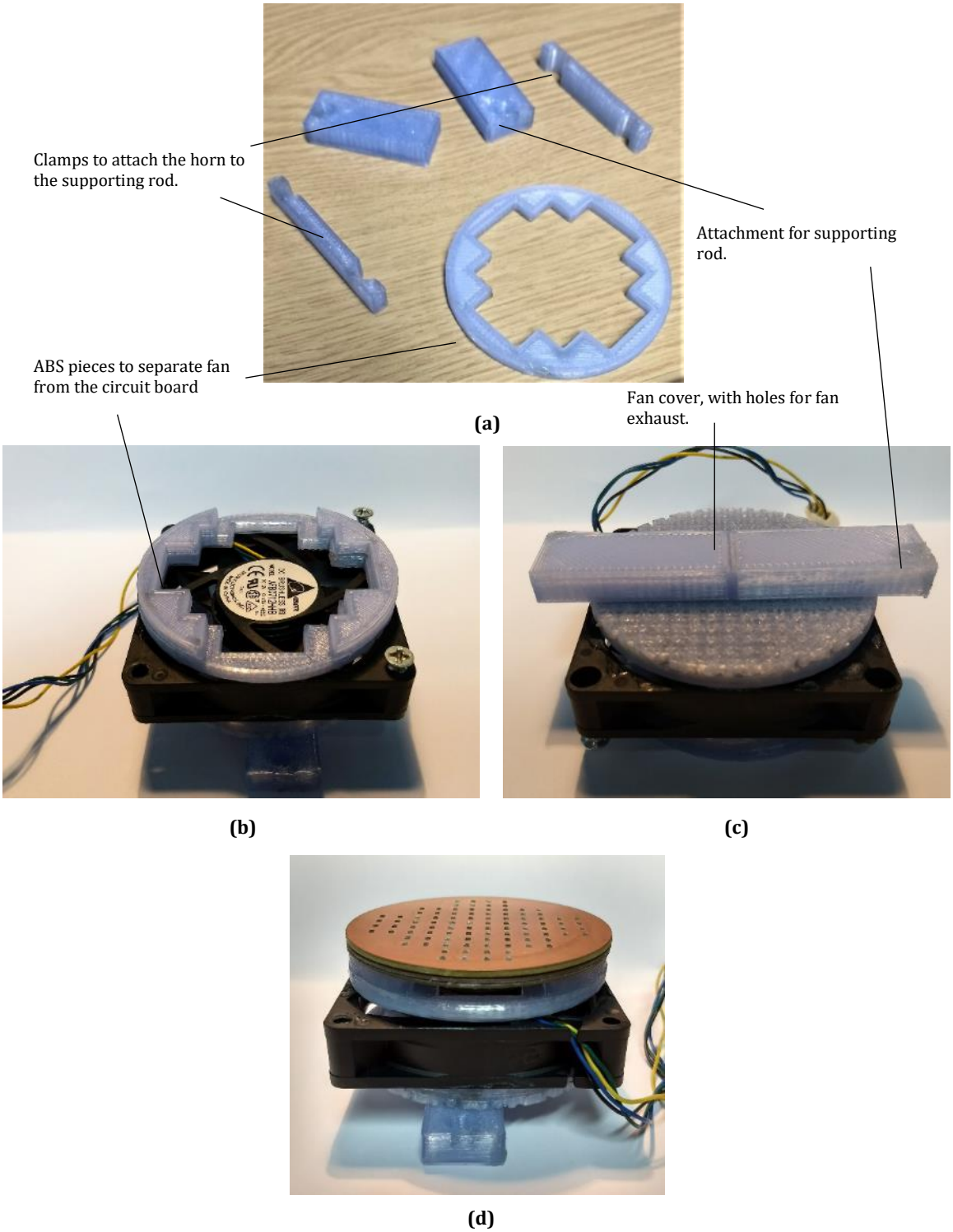

Fig. 5-4: (a) 3-D printed pieces for the reflectarray supporting structure (b) topside of the reflectarray fan assembly (c) backside of the reflectarray fan assembly (d) reflectarray assembly with FR-4 layers (not secured)

Fig. 5-4 (a) depicts some of the 3-D printed structures. Each piece was designed to be easily glued into its required location once finalised. Fig. 5-4 (b, c) shows the

assembled cooling mechanism, along with the feed-horn support upon which the reflectarray sits. The fan itself is taken from a PC, and operates from a separate 12V supply, drawing 300mA. The pieces shown in Fig. 5-4 (b) were necessary to ensure that when the reflectarray is mounted above the fan, there will be space for the control wires of each quad-unit-cell. Fig. 5-4 (d) shows the reflectarray FR-4 layers assembled with the fan assembly. In this image, the reflectarray is not secured in place, as this is not done until the reflectarray is mounted in the chamber. The FR-4 layer was secured to the ABS fan assembly using double sided tape, so that if modification is required, the layers can be easily separated.

During testing of the reflectarray, modifications were made to the 3-D printed designs, based on the performance of various components. The main issue observed was that the holes for the fan exhaust were not sufficient, and much larger holes were required. This was solved by removing large sections for the fan cover, allowing the fan to operate more efficiently. Additionally, a second attachment was used, where the design in Fig. 4-13 only has a single attachment. This forms a better base and provides a second option for the horn attachment.

The supporting rod was not 3-D printed, as this piece would be particularly challenging in a 3-D printer. The horn was mounted to the supporting rod using the

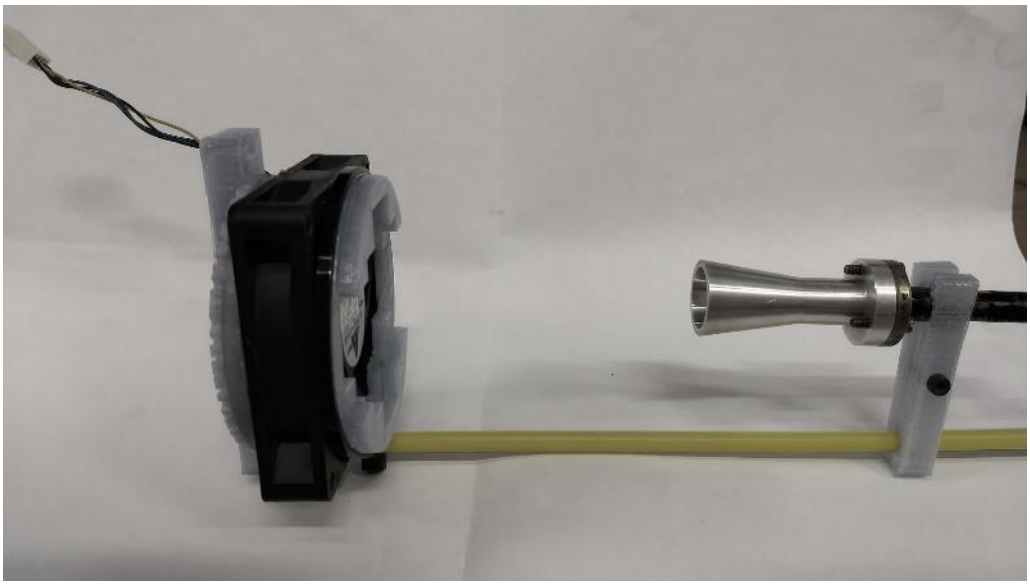

Fig. 5-5: The reflectarray structure with the mounting rod for the horn.

3-D printed clamps, as shown in Fig. 5-5. The advantage of this method of attaching the feed-horn is that the distance from the array can be optimised to provide the best performance.

5.3.3 Silicon and inkjet-printed layers

The silicon layer is again secured directly onto the FR-4 layer. This is done through the use of a ring of double-side tape around the outside of the FR-4 layer. This is done to ensure that the unknown dielectric properties of the tape do not impact the response of the array itself. It also allows the different layers of the reflectarray to be separated for further modification to the design.

The final layer at the top of the reflectarray is the PET layer containing the silver inkjet printing grating layer (Fig. 5-6(b)). The inkjet-printed layer required a number of attempts prior to achieving the optimum performance from the printer. Some imperfections remain in the design, with some gratings having small areas in which ink is not present. It is here where the main advantage of this printing exists, in that it is possible to re-print the top layer rapidly, to firstly improve the fabrication quality and secondly provide different phase responses for the reflectarray.

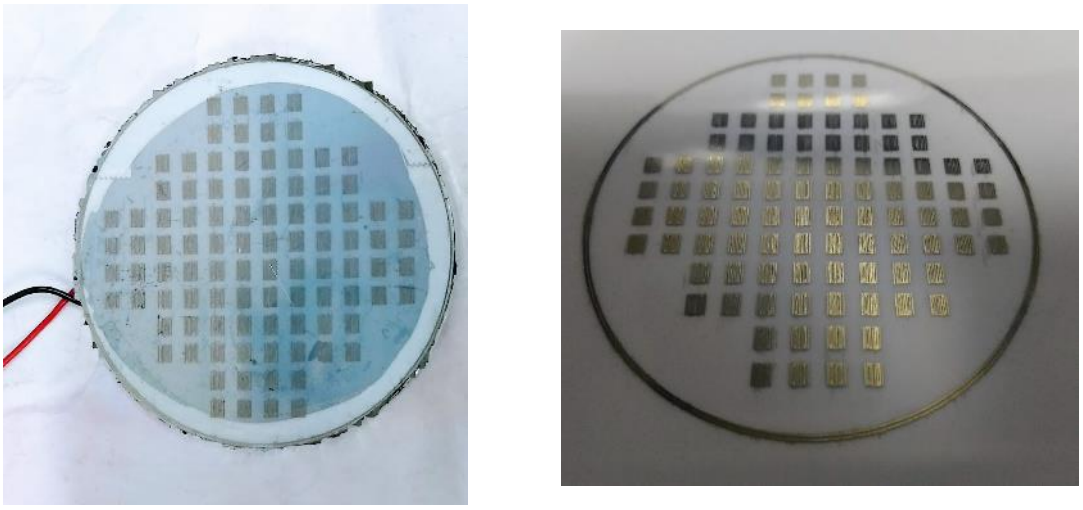

(a) **(b)**

Fig. 5-6: :(a) The reflectarray with the silicon layer secured to the top surface of the FR-4 layer and the inkjet-printed grating attached with double sided tape (b) The inkjet- printed PET grating layer.

5.4 Test fixture design and fabrication

To accurately and consistently measure the performance of the reflectarray, the design of a test fixture for placement inside the anechoic chamber is necessary. The four screws for the fan were used as the main attachment for the array to the test fixture. A large L-shaped bracket is used to mount which is then placed on the table inside the anechoic chamber. The reflectarray itself is located 250 mm above the table, which is high enough to ensure that absorbers can be placed to prevent

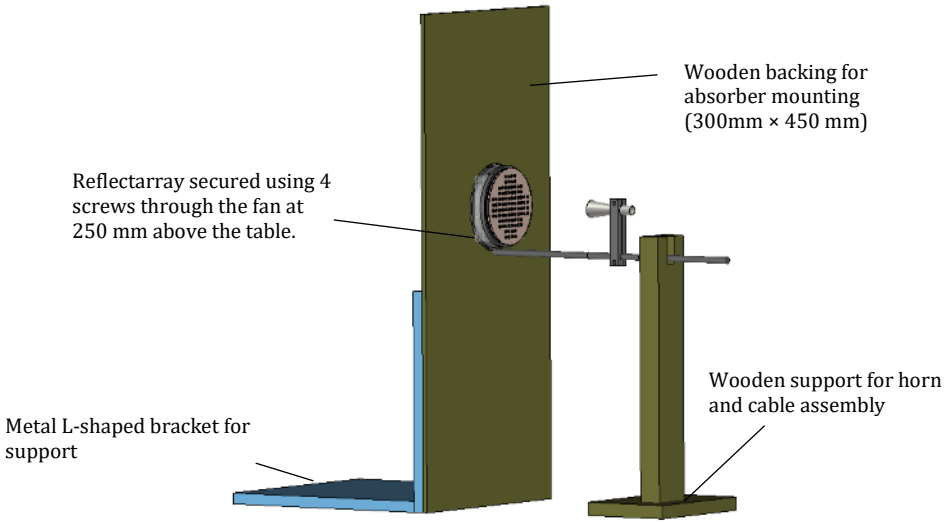

(a)

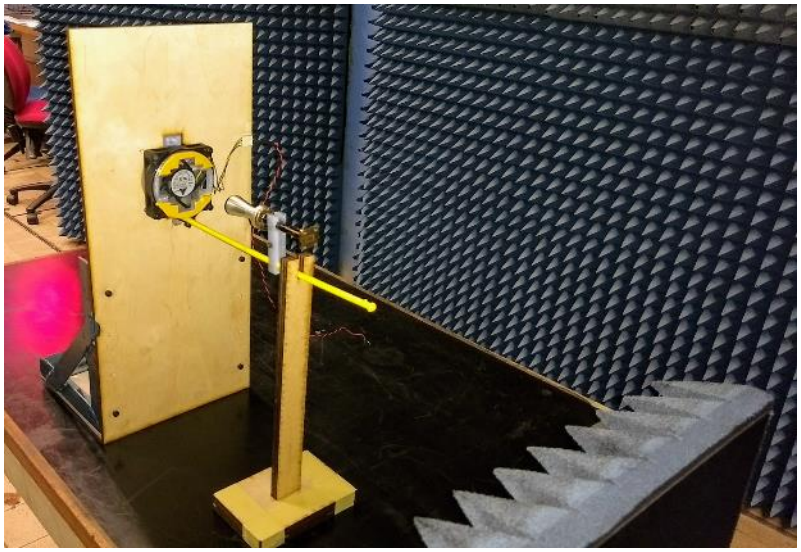

(b)

Fig. 5-7: (a) 3-D design of the reflectarray test fixture (b) fabricated test fixture placed inside the planar scanner chamber.

reflection from the table itself. The 3-D design of the test fixture is shown in Fig. 5-7 (a) and the fabricated fixture is shown in Fig. 5-7(b). It was discovered during the fabrication that the plastic rod for the horn and cable assembly would need to be supported due to the weight of the cable, so a wooden support structure was fabricated to ensure that the horn and cable assembly maintain a stable position.

5.5 The fabricated reflectarray

The fabricated reflectarray mounted for measurement is shown in Fig. 5-8(a-c) from various angles. The reflectarray is powered by a 5V, 5A power supply and the full structure can be mounted inside of the planar near-field scanner anechoic chamber. The horn is fed through a rectangular to circular waveguide transition, which itself is connected to a Keysight PNA-X through a coaxial to WR-28 waveguide transition.

The initial measurements for the array were carried out using low power for the IR-LEDs, enabling the use of the lower rated power supply. This is more compact, and prevents the reflectarray overheating and damage occurring to the LEDs themselves. Furthermore, it shows that initial cooling mechanism needs to be further improved, as even at a low current draw, the reflectarray becomes warm. The fan must be operated in its maximum 12V speed due to the heat produced by the LM3410 chips. If this is not present, the driver chips enter a thermal shut-off mode and need time to cool. The layers of the reflectarray are also sealed with aluminium foil backed tape, to ensure that minimal leakage is present between the layers.

The use of the test fixture has a second advantage in that it allows absorbers to be placed around the antenna, to ensure that the results for the antenna are as accurate as possible. Radio absorbing material is also placed on the cable assembly to ensure that this has minimal reflections. However, it was seen in the near-field scan results that this could not be completely removed from the scan.

(a)

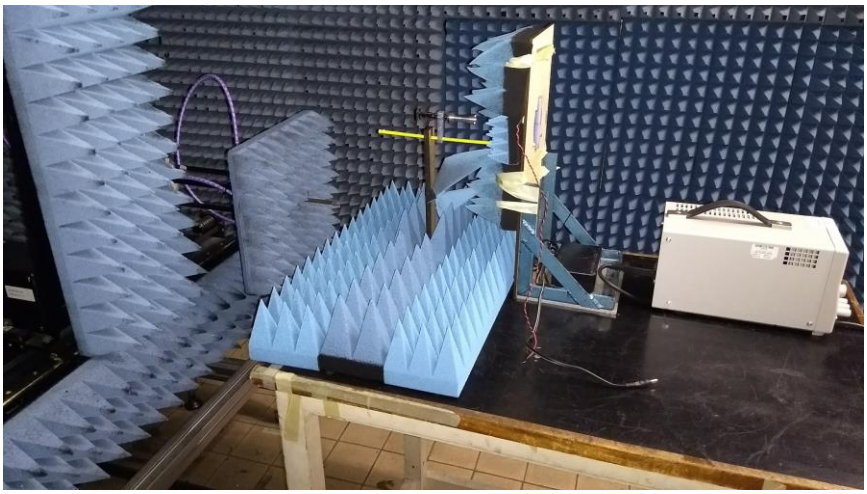

(b)

Fig. 5-8: (a,b) Test fixture for the reflectarray measurement, showing absorbers, power supply and horn.

5.6 Measurement results

5.6.1 Focal point optimisation

The first measurement to be carried out was to verify the off-state performance of the reflectarray, and to ensure that the feed-horn was centred in the correct position. Both the incident angle of the feed-horn and the distance at which it is located are important parameters which need to be optimised to ensure the best operation of the reflectarray. To facilitate this, the feed horn was removed from the supporting rod, and the wooden support was placed on a translation stage, as shown in Fig. 5-9 which allowed the distance from the reflectarray to be optimised using small movements. The angle was also adjusted manually, to ensure that the feed horn illuminates the central point of the reflectarray. The design stipulates a focal distance of 160 mm, and measurements at further focal distances provided poorer results. Thus, the feed distance was varied from 160 mm to 140 mm with respect to the centre of the reflectarray, with the results provided in Fig. 5-10 (a, b).

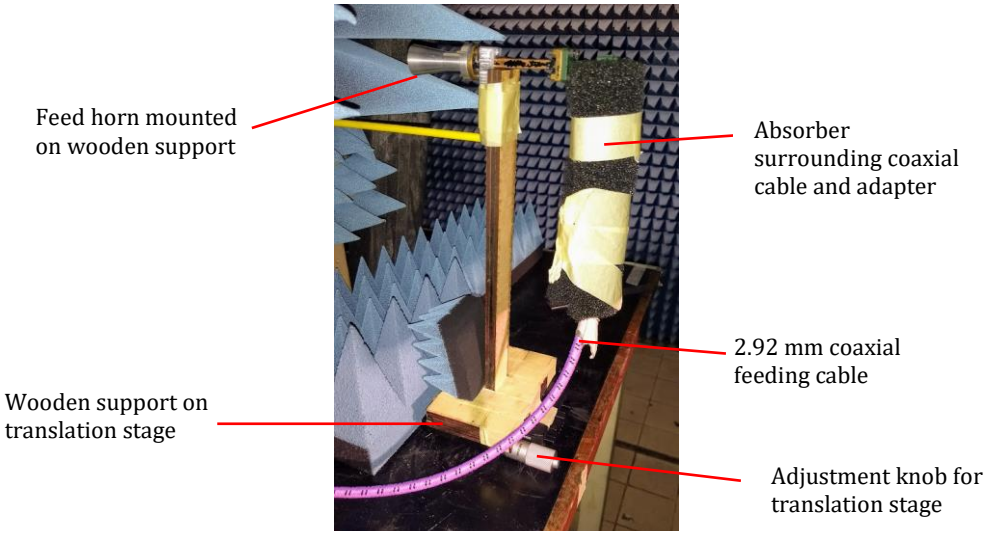

Fig. 5-9: Image of the measurement setup for the focal point optimisation, with the feed horn placed on a translation stage.

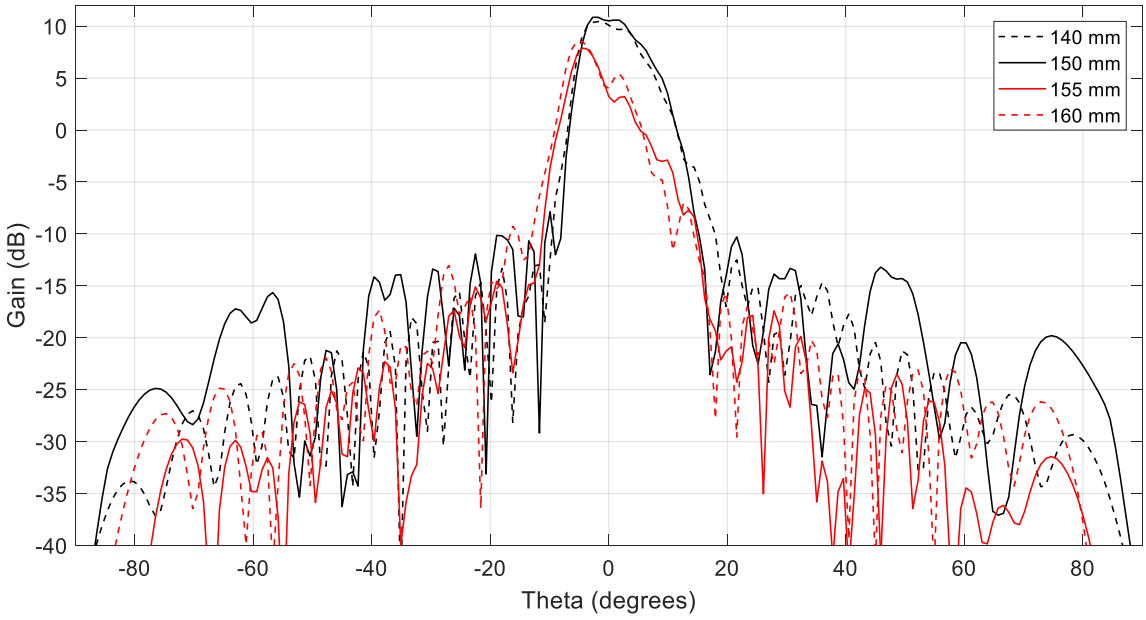

(a)

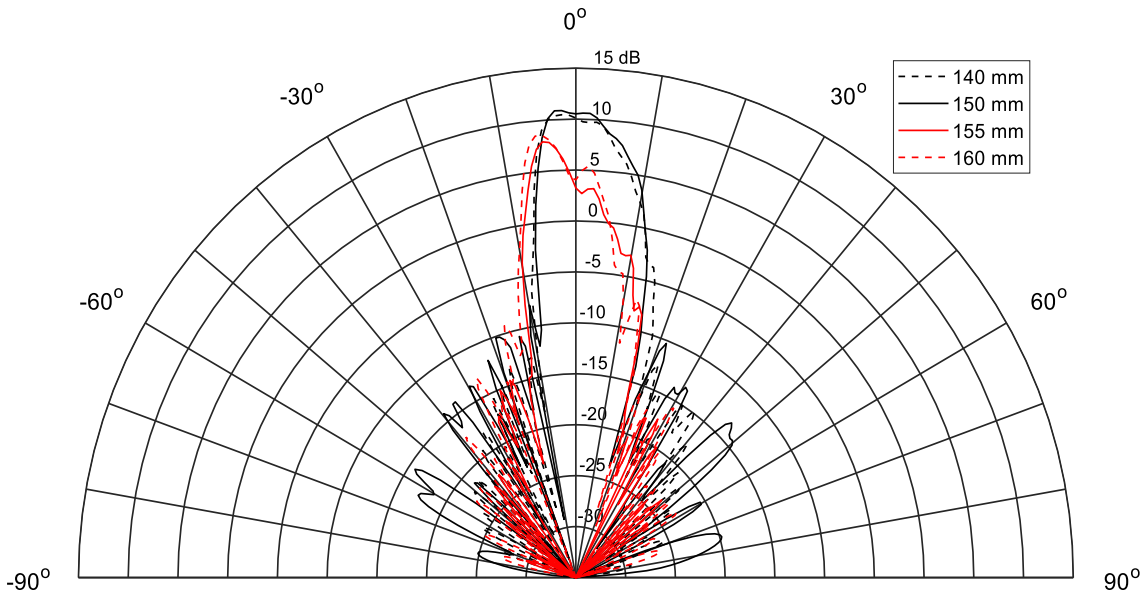

(b)

Fig. 5-10: Farfield radiation patterns at 31 GHz for the focal point optimisation measurements in: (a) Cartesian form (b) Polar form.

The results show that the optimal distance for the reflectarray is at 150 mm from the reflectarray. The results also show the anticipated feed blockage, some of which was minimised through the use of absorbers and accurate positioning of the cable

structure. Nevertheless, the resulting beam was asymmetric in both the azimuth and elevation profiles. This is one key area for future designs to improve. Another area for improvement is the fabrication of the reflectarray, as throughout the design process, there has been an uncertaintiy of the air-gaps between each layer, which had to be compensated by designing the reflectarray at 34 GHz, in the knowledge that the air gaps will cause the frequency to drop towards 31 GHz, where there is the highest amount of reflection magnitude variation. An improved design would eliminate these air-gaps altogether.

From these first measurements, it is also clear that the gain of the structure is lower than that which was anticipated by the simulation results. The main reason for this is the fabrication quality of the various layers of the structure, resulting in larger than anticipated losses. In particular two main sources of loss were leakage from between the different layers, which was minimised by the use of foil tape, and the PET grating layer being less conductive than anticipated. The latter of these means that the array is less reflective, as the overall conductivity is lower.

5.6.2 Initial low current measurements

The initial measurements, to verify the operation of the IR-LEDs, were carried out with a low current for each quad-unit-cell. This ensured that if any design or fabrication errors were present, these would not seriously damage the IR-LEDs or the LM3410 ICs. This meant that each LED was driven by 42 mA, with a total current draw of 1 A for the whole reflectarray. Despite this low current, the circuit still required the use of the fan, as the structure became warm during its operation. Furthermore, a detailed near-field scan of the antenna has a duration of between 6 and 8 minutes, over which time the reflectarray will become quite warm even with the cooling mechanism in place. The initial results showed a small deviation, but more deviation can be achieved with a larger current.

These initial results showed that the low operating current results provided a small deviation between the on and off states. It was also observed that the fan,

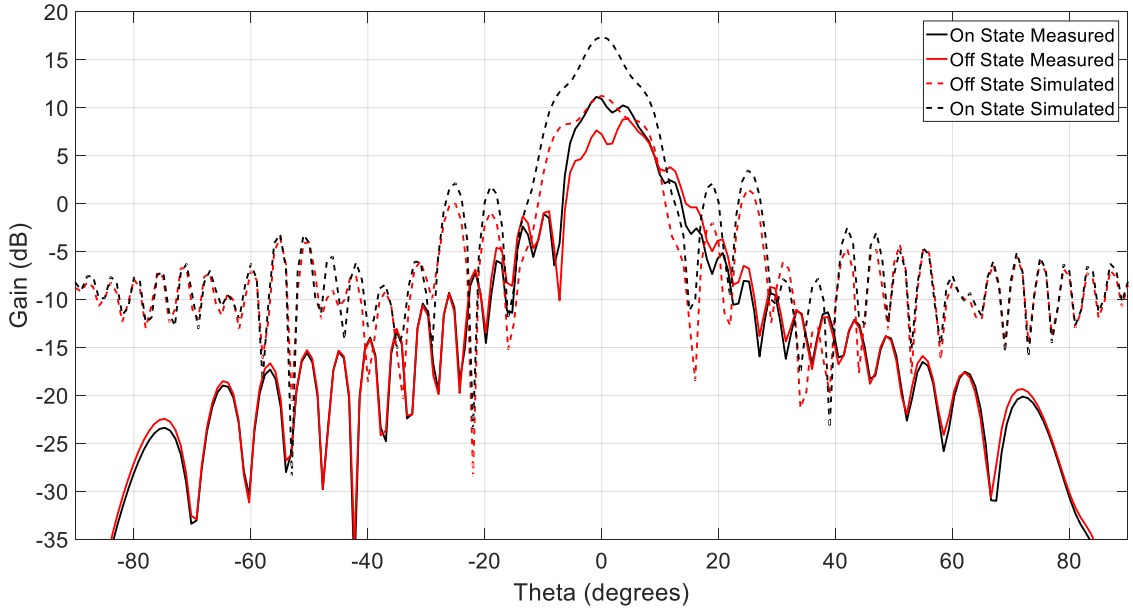

(a)

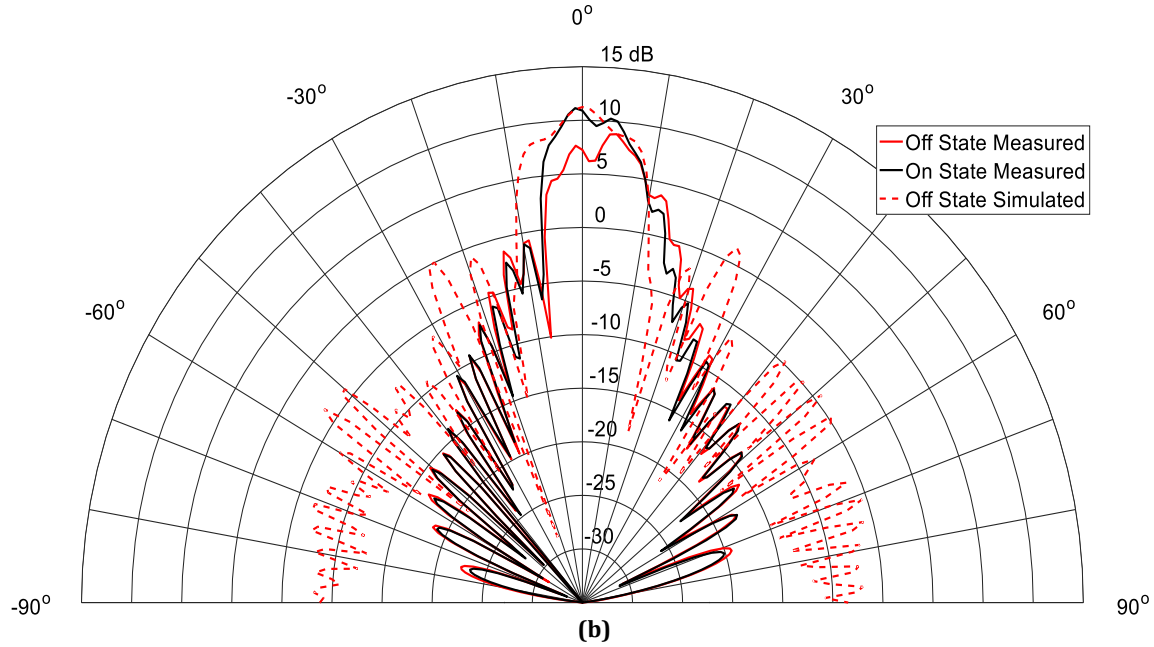

(b)

Fig. 5-11: On and off state measured gain results for the 125mA per-cell case (a) Cartesian plot (b) Polar plot

combined with the ground layers acting as heat-sinks were sufficient to ensure that there was no overheating. This meant that the design could operate at a higher operating current. To facilitate this, the sense resistor was replaced with a lower value, increasing the current in each cell to 125 mA by using a 2Ω resistor which provided a much more noticeable gain difference, as shown in Fig. 5-11 (a, b).

The results in Fig. 5-11 (a, b) show a slightly different pattern to those which are shown in Fig. 5-10 (a, b), particularly the sidelobes of the pattern. This is due to the measurement error which is present when the array is reassembled after the resistor modification. It is possible to see that there is a slightly higher sidelobe at approximately -10°, due to the control wires for the reflectarray, which were present in this experiment. However, the results also show that the gain pattern increases by up to 5 dB, at the main-lobe, without significant increase to the sidelobes. An additional source of error is the use of absorbers on each side of the reflectarray, which in these first measurements were of the wrong frequency and were affecting the radiation pattern themselves. For the results presented after this, they were replaced with correct sized absorbers.

5.6.3 Amplitude tapering

The initial results presented in the previous section, have shown that it is possible to adjust the magnitude of the main-lobe of the reflected pattern using the IR-LED array, with each LED operating at 125 mA. However, to facilitate the amplitude tapering in this design, several modifications need to be made to each cell.

The first modification is to ensure that the full range of biasing currents required for the amplitude reconfiguration can be achieved. This again requires modification to the current sense resistor. Specifically, on each quad-unit-cell the value of the sense resistor is reduced to 0.68Ω, meaning that each quad-unit-cell can draw a maximum of 500 mA. However, as mentioned, this is an unsustainable current draw, and as such, the current draw of each cell must be limited through the use of a PWM signal at the input to the "DIMM" pin of the driver IC. The driver circuit presented in Fig. 4-12 contains an off-board connector, which is connected directly to this pin, which is in place for this purpose.

The use of a PWM signal to control the brightness of the IR-LEDs is possible due to the internal switch in the TI LM3410 chip. By driving the "DIMM" pin with an alternating digital signal, it has the same effect as repetitively enabling and disabling

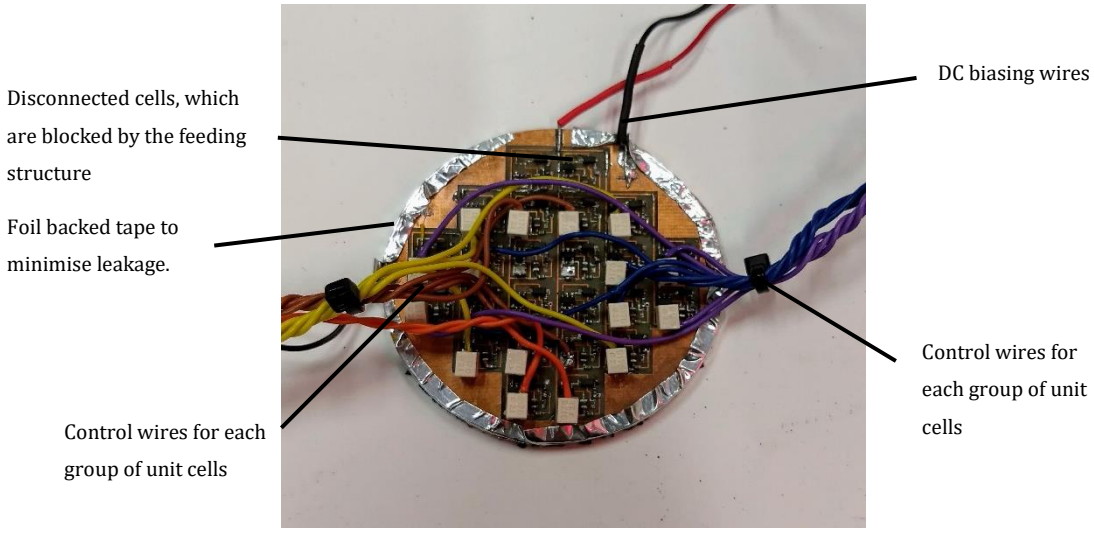

Fig. 5-12: The reflectarray with the control wires for each driver circuit grouping.

the chip. Therefore, the average drive current when using a PWM signal over a certain period of time will be less than if the DIMM pin is left floating or driven to a permanent enable state (i.e. using a 100% duty cycle signal).

Although each LED driver IC can be controlled individually, the symmetrical nature of this reflectarray allows the driver chips to be grouped together, meaning that fewer control lines are required, and a compact microcontroller such as an Arduino can be used to generate the PWM signal. A simple method for generating a PWM signal is to simply alternate the output voltage of a microcontroller pin, and subsequently vary the duty cycle. A 50% duty cycle corresponds to halving the driver current, while a 25% duty cycle will result in a 125 mA current draw. The software for controlling the Arduino is included in Appendix A. Each grouping of the driver chips is colour coded, for ease of programming, as shown in Fig. 5-12. The central four elements are not controlled, since in all amplitude distributions, the central four elements have the maximum current. Furthermore, the two elements, which are located at the bottom of the reflectarray (top of Fig. 5-12) are disconnected due to fabrication errors. This does not have a significant impact on the results, as this section is blocked by the feed structure in the measurement.

As this was the final experiment with this reflectarray implementation, three quad-unit-cells had malfunctioning driver chips. The most critical of these was located in the centre of the array, which prevented the operation of four individual unit-cells. Due to fabrication cost and time constraints, a second board could not be fabricated to replace this quad-unit-cell. However, it does show the advantage of using a parallel connection for each quad-unit-cell.

The results for a binomial distribution, implemented across the array as in Fig. 4-3, are shown in Fig. 5-13. The results show that some sidelobe reduction is possible even with this small array configuration. Furthermore, it also shows that the gain does not significantly reduce when the distribution is applied. However, the reduction is only small, due to a variety of reasons. The first is that the feed is blocking a significant portion of the pattern, and possibly removing some of the effect of the IR-LEDs being activated. Furthermore, the malfunctioning unit-cell in the centre of the array may be having a significant effect on main-lobe shape, causing a slightly misshapen beam at θ = 5°. However, this amplitude distribution has resulted in a reduction in the sidelobe pattern of up to 5 dB at some angles. More specifically, at 30°, the sidelobes are reduced from -10dB in the off state, to -16dB in the on state. The effect is less pronounced in the negative angular direction, due to the larger cabling structure which is present on one side of the array. These wires cause the reflections seen at -10°, masking some of the sidelobe reduction on this side. However, sidelobe reduction is observed on both sides of the reflectarray, proving the potential for this type of reconfiguration mechanism in larger reflectarray designs.

The comparison with the simulated results shows a good agreement in terms of the main-lobe of the reflectarray, but the sidelobes of the simulated pattern are higher than those of the measured pattern. This is potentially due to the inaccurate modelling of the reflectarray in the simulation which was necessary reduce the simulation time.

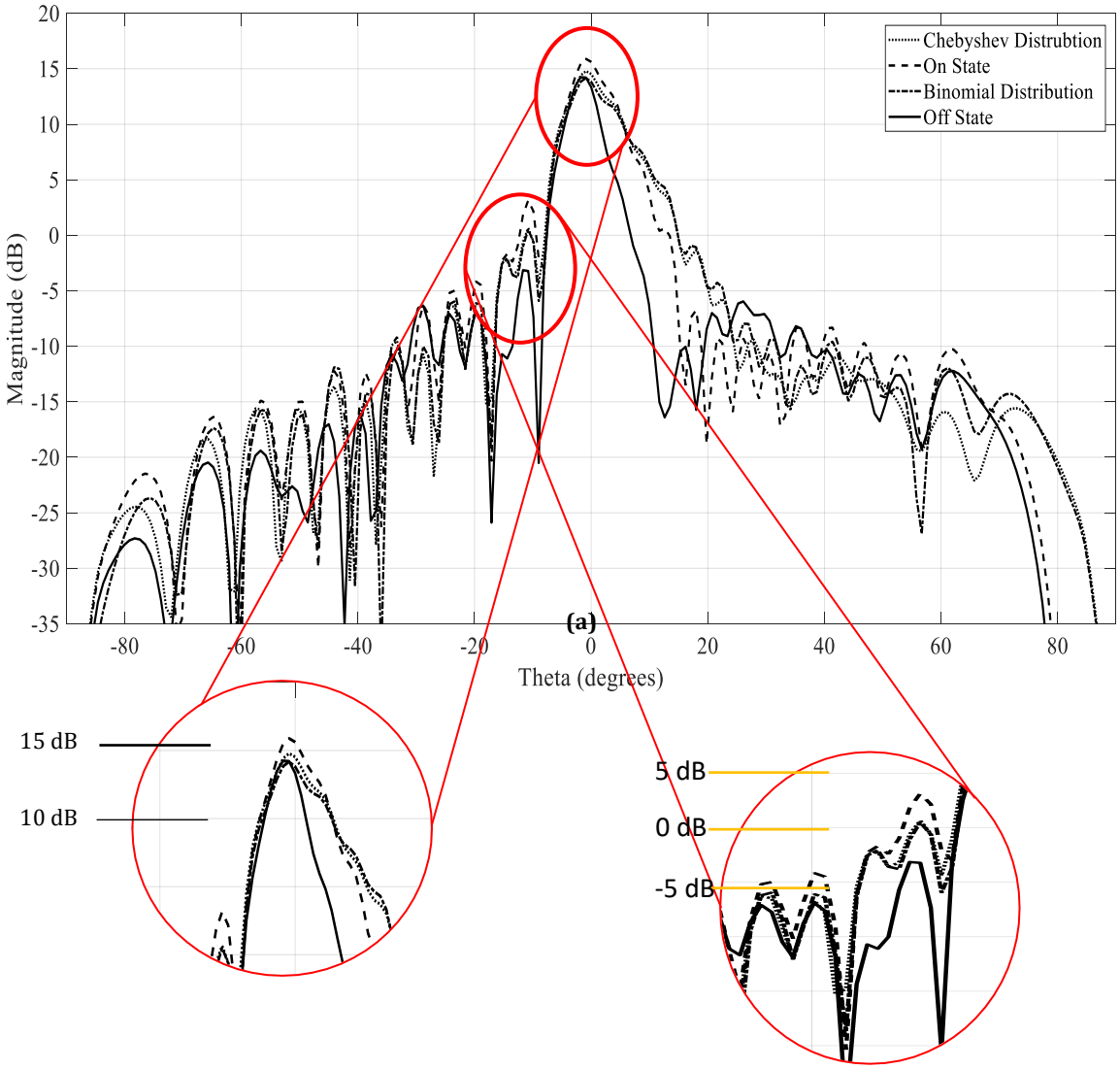

Fig. 5-13: Results for a binomial distribution spread across the reflectarray surface. The insets highlight the small reduction in gain, but also show the -3dB sidelobe reduction which is present.

5.7 Design limitations

This prototype design had two main objectives: the first being to prove the concept of amplitude reconfiguration in a reflectarray antenna, making use of a low-cost, small form factor illumination mechanism; the second was to highlight the main areas in which future designs of optically reconfigurable reflectarrays can be improved. The results presented in the previous subsections have shown that the reconfiguration mechanism is applicable to reflectarray antennas operating in Ka-

band, but during the fabrication and testing of the design, a number of areas of improvement have been highlighted, which will be summarised in this section.

The first area which has been referred to several times in the measurement section is that of the feeding mechanism for the reflectarray. The simulation results did not highlight the extent to which the feed structure would impact the radiation characteristics, and as such a centre fed reflectarray was designed originally. Furthermore, the symmetric nature of a centre fed reflectarray ensures that fewer control wires are required for the control of the LED brightness, which would not be possible if an offset, asymmetric design was used. However, the measured results showed that the feed shadowing effect was significant, so an offset fed reflectarray would be the first improvement to this design, and is quite simple to implement, as it only requires the adjustment of the top layer grating dimensions.

Secondly, throughout the measurement process, the current has had to be controlled carefully to prevent damage to the IR-LEDs and the other components on the board through over-heating or from the components' inability to handle high current loads. For example, the tracks on this board would need to be widened to allow for high current operation, and the DC power wires would need to be thicker to allow the full 12 A operation of the reflectarray. Further to this, increased heat-sinking, or the inclusion of liquid cooling should be considered in the design of later prototypes.

Finally, the fabrication process should be improved in a number of areas. The securing of the different layers should be considered in more detail, along with a more permanent solution than what was implemented in the prototype demonstrator. The inkjet printed layer on the top surface should also be refabricated to ensure it is as conductive as possible. In addition, machine automated placement of the components would ensure that all the quad-unit-cells function appropriately, as with manual fabrication of each layer, there is a higher degree of error and greater possibility of damaging components, resulting in malfunctioning unit-cells.

However, despite these limitations, it has been seen through the measurement results that the reflectarray functions with a satisfactory performance and operates in the manner that it was designed to. This design therefore provides a good starting point for future iterations of this concept.

5.8 Summary

This chapter has provided a detailed documentation of the process by which the reflectarray antenna was fabricated and measured. Initially, a review of the techniques which can be used to measure reflectarray antennas was carried out, referring to measurements of reflectarrays available in the literature. Based on the equipment available, and the AUT structural requirements of the different measurement techniques, planar near-field scanning of the reflectarray was used to ascertain its response in the far-field.

Following this, the fabrication of the reflectarray was detailed, beginning with the 3-D printing of the various pieces required to secure the cooling fan to the reflectarray itself. In addition to this, the FR-4 circuits were fabricated using the in-house milling machine, and the components attached to the appropriate layers. The layers were secured together using strong double-sided tape, and the feed-horn was attached to the array.

Once the fabrication was complete, the test fixture for the measurement of the reflectarray was designed and fabricated, allowing for the placement of absorbers around the array and to ensure that the measurements were repeatable throughout the various changes to the array components.

The planar near-field scanner was then used to measure the response of the reflectarray. Firstly, a translation stage was used to accurately determine the appropriate focal point for the horn. The horn was then fixed in this location throughout the experiments. A deviation of 10 mm was observed, which can be attributed to fabrication inaccuracies in the design and inaccuracies in the modelling of the feed horn. After this, the reflectarray was measured with the LEDs operating

with a low current input to ensure that no damage was done to any of the components during the early testing phases. The current was gradually increased by means of changing the current sense resistor to smaller values, which resulted in more variation of the gain of the reflectarray.

The final measurement involved the use of a microcontroller to vary the brightness of the IR-LEDs in groups of four quad-unit-cells. This was done using PWM signals to the driver chip, allowing for brightness variation based on the duty cycle of the input signal. For maximum brightness variation, the sense resistors were changed to their lowest value. A small amount of sidelobe suppression was observed, with a maximum reduction of 5dB. Finally, improvements to the reflectarray based on the limitations of this design are suggested.

Chapter 6:

Conclusions and Future work

6.1 Conclusions

The vast nature of the mm-wave spectrum means that it encompasses many technologies, ranging from lumped element-based devices at the lower frequencies to the need for quasi-optical systems at the upper mm-wave frequencies. The considerable number of technologies which are available provide the means to drive the high number of applications which are taking hold in the mm-wave spectrum. In particular, those bands which can provide consumer products, or connectivity for communications between consumer devices are becoming popular. This work has studied these applications, their operating requirements and their state of development. It was observed that those bands from 30 to 110 GHz are becoming increasingly well-used, but many are already in a late stage of development due to the fast-pace of the communications industry. However, Ka-band SATCOM technologies were identified as one band which has sufficient room for development and areas in which novel technologies can be applied.

The antenna systems which can operate in this band include reflector systems, phased arrays and the reflectarray antenna, which combines the preceding two

antenna systems into a more planar high gain system. These antenna systems have been applied to the various applications which work up to 110 GHz, with differing reconfiguration techniques used to meet the requirements of each operating band.

Systems in Ka-band were seen to require highly directional beams with the ability to steer over a small angle. They can also benefit from amplitude reconfiguration to minimise interference between co-located systems. This was seen through a comprehensive study of the literature, including analysis of the various reconfiguration mechanisms available, and the state-of-the-art in Ka-band systems. From this, the direction of the research turned towards the chosen reconfiguration mechanism, specifically, optically activated silicon and the antenna system which it can be applied to – the reflectarray antenna.

Although silicon has previously been used in designs beyond Ka-band as was seen in the literature, this form of reconfiguration is often cumbersome and has potential dangers associated with it due to the high-power light sources used. However, a novel illumination technique was proposed which moves away from high power laser sources and lenses and towards high power IR-LEDs. By doing so, the illumination source becomes much more compact without a severe detrimental effect on the performance of the reconfiguration mechanism provided the system is designed appropriately. This is shown by comparing the source to an IR based laser illumination system. However, the use of this novel illumination mechanism in an antenna necessitated the characterisation of the silicon under illumination at various frequencies. A simulation-measurement matching technique was used to extract the illuminated and un-illuminated properties of the silicon. A transmission line measurement technique was used at lower frequencies, while a waveguide based characterisation cell was used for measurements at Ka-band. Once the properties of the silicon in various illuminations states were obtained, the design of the unit-cell for the reflectarray could be undertaken.

The first stage of the design of the reflectarray was to use a numerical model to predict the radiation response of the reflectarray in different illuminations states. It

also enables the calculation of the phase delay for each unit-cell to ensure the beam is generated in the far-field of the reflectarray. The unit-cell used was similar to the design used for the Ka-band silicon characterisation cell. The multilayer structure of the unit-cell improves bandwidth of the unit-cell and ensures isolation of the RF and the DC biasing lines for the LED. The reflection response and the phase response of the unit-cell are both measured, with both being satisfactory for the design of the reflectarray. However, based on the requirements for the LED, a driver circuit must be included with each LED, which stipulated the design of the quad-unit-cell, in which four LEDs are driven in series across four individual unit-cells. This quad-unit-cell is then formed into the full array, which is then simulated to verify its performance.

The final design of the reflectarray incorporates the feed-horn structure, and the cooling mechanism for the driver circuits. This design is then manufactured using a range of new fabrication technologies including 3-D printing and material printing which both allow rapid fabrication of the prototype design. The range of measurement techniques available for the verification of the performance of the reflectarray are considered for their benefits with planar scanning being the technique of choice for this array. This is then used for the measurement of the reflectarray. The reflectarray is then further modified to incorporate amplitude tapering, with a view to improving the radiation characteristics. Finally, the limitations of this design are considered, with areas for improvement being highlighted.

6.2 Key contributions

This major contributions of this work are summarised in this sub-section.

The first contribution is that of the new illumination method and the analysis of the response of the silicon to it. Previous work had only generally considered high power laser sources and lens based illumination for the silicon. However, this work has provided much more compact light source and compared its performance to existing methods, proving it to be a satisfactory alternative. The properties of the silicon under this LED illumination are also provided here for future applications.

Another contribution is that of the unit-cell and its multilayer structure. This design is, to the authors' knowledge, the first time that both ink-jet printing and 3-D printing have been combined in Ka-band reflectarray design. This therefore enables rapid prototyping of the reflectarray meaning that errors can be easily be rectified and layers or sections be replaced easily.

Finally, this work has contributed a novel reflectarray design which can provide amplitude reconfiguration, enabling a method for sidelobe reduction and beam-shaping. This has a potential impact on applications such as Sat-Com On-The-Move and can provide a means to prevent interference between systems which are operating in close proximity by enabling frequency re-use.

6.3 Future work

This work provides the design of an active and reconfigurable system at mm-wave frequencies. Considerations of the limitations of this work and the natural progression of this thesis, provide a direct route for exploring this area of research further.

The clearest objective from the measurement results, is that the power handling of the board itself should be improved. Furthermore, an analysis of the effect on the silicon of the increase in temperature caused by the high current should be done. In addition to this, another key area for further exploration is an accurate calculation of the efficiency, through the use of a reverberation chamber.

With this implemented, a further development would be to convert the design into a folded reflectarray design [121], which provides a much more planar design, making use of a sub-reflector system. This would enable the system to be potentially mounted on aircraft or other vehicles, where a low-profile design would be applicable. This can be combined with a larger reflectarray to provide higher gain capability. In addition to this, the horn antenna which is traditionally used with a folded reflectarray could also be replaced with a planar phased array feeding mechanism, which would further decrease the form factor of the reflectarray antenna.

Another development to the reflectarray would be to take the design to higher frequencies. It was proven by *Gamlath et.al.* in [92] that silicon can operate well at frequencies towards 60 GHz, and operation at this frequency would allow for a greater number of elements without an impact on the reflectarray size. However, this would require much more development to the illumination mechanism, as the more compact unit-cell would make it challenging to implement the compact light source.

Appendix A :

Software for LED Brightness Control

The brightness of the IR-LEDs can be controlled through PWM at the input to pin 4 of each of the driver chip ICs. The duty cycle of the input signal acts as an alternating enable signal, which means that the IC is activated for a shorter period of time, thereby reducing the overall current consumption.

```
int ledPin = 9; // LED connected to digital pin 9
int ledPin2 = 10; //LED connected to digital pin 10
int ledPin3 = 11; //LED connected to digital pin 11
int ledPin4 = 6; //LED connected to digital pin 6
int ledPin5 = 5; //LED connected to digital pin 5
int val = 0;  // variable to store the PWM duty cycle
int val2 = 0; // variable to store the PWM duty cycle
int val3 = 0; //variable to store the PWM duty cycle
int val4 = 0; //variable to store the PWM duty cycle
int val5 = 0; //variable to store the PWM duty cycle

void setup() {
   pinMode(ledPin, OUTPUT); // sets the pin as output
   pinMode(ledPin2, OUTPUT);
   pinMode(ledPin3, OUTPUT);
   pinMode(ledPin4, OUTPUT);
   pinMode(ledPin5, OUTPUT)
```

```
void loop() {
  //set LED brightness via PWM: 255 = 100% duty cycle, 127 = 50%
duty cycle
   val  = 26; // orange outer pins
   val2 = 127; //yellow inner pins
   val3 = 127; //brown inner pins
   val4 = 127; //blue inner pins
   val5 = 26; //purple outer pins
   //writing to LED pins
   analogWrite(ledPin, val);  //write to pin 9
   analogWrite(ledPin2,val2); //write to pin 10
   analogWrite(ledPin3,val3); //write to pin 11
   analogWrite(ledPin4,val4); //write to pin 6
   analogWrite(ledPin5,val5); //write to pin 5
```

References

[1] C. A. Balanis, Antenna Theory - Analysis and Design (3rd Edition). John Wiley & Sons, 2005.

[2] OFCOM, "Release of the 59 - 64 GHz band," 2009. [Online]. Available: http://stakeholder.ofcom.org.uk/consultation/59_64ghz/statement/.

[3] R. Lachner, "Development Status of Next generation Automotive Radar in EU," 2009.[Online].Available:http://itsforum.gr.jp/Public/J3Schedule/P22/lachner090226.pdf.

[4] L. Yujiri, M. Shoucri, and P. Moffa, "Passive millimeter-wave imaging," IEEE Microw. Mag., vol. 4, no. 3, pp. 39–50, Sep. 2003.

[5] J. Hasch et al., "Millimeter-Wave Technology for Automotive Radar Sensors in the 77 GHz Frequency Band," Microw. Theory Tech. IEEE Trans., vol. 60, no. 3, pp. 845–860, 2012.

[6] W. Menzel and A. Moebius, "Antenna Concepts for Millimeter-Wave Automotive Radar Sensors," Proc. IEEE, vol. 100, no. 7, pp. 2372–2379, Jul. 2012.

[7] "Maximum permissible levels of off-axis EIRP density from earth stations in geostationary-satellite orbit networks operating in the fixed-satellite service transmitting in the 6 GHz, 13 GHz, 14 GHz and 30 GHz frequency bands," 1978.

[8] Agilent Technologies, "Wireless LAN at 60GHz - IEEE 802.11ad Explained," 2013. [Online].

[9] "ITU Regulations for Ka-band Satellite Networks.", ITU Technical Report, 2012.

[10] "FCC grants oneweb access to U.S. Market for its proposed new broadband satellite constellation.", FCC Technical Report, Jun. 2017.

[11] L. Baggen et al., "Designing integrated frontends for satcom applications," in International Semiconductor Conference (CAS), 2012, pp. 11–18.

[12] J. Huang and J. A. Encinar, Reflectarray Antennas. John Wiley & Sons, Inc., Hoboken: NJ, USA, 2007.

[13] M. Kaynak et al., "Wide-angle scanning active transmit/receive reflectarray," IET Microwaves, Antennas Propag., vol. 8, no. 11, pp. 811–818, Aug. 2014.

[14] "FCC 16-89 Use of Spectrum Bands Above 24 GHz For Mobile Radio Services.", FCC Technical Report, Jul. 2016.

[15] T. S. Rappaport et al. "Overview of Millimeter Wave Communications for Fifth-Generation (5G) Wireless Networks-with a focus on Propagation Models," IEEE Trans. Antennas Propag., pp. 1–1, 2017.

[16] T. S. Rappaport et al., "Millimeter Wave Mobile Communications for 5G Cellular: It Will Work!," IEEE Access, vol. 1, pp. 335–349, 2013.

[17] A. Rahimian, Y. Alfadhl, and A. Alomainy, "Analytical and numerical evaluations of flexible V-band Rotman lens beamforming network performance for conformal wireless subsystems," Prog. Electromagn. Res. B, vol. 71, pp. 77–89, 2016.

[18] Chao-Hsiung Tseng, Chih-Jung Chen, and Tah-Hsiung Chu, "A Low-Cost 60-GHz Switched-Beam Patch Antenna Array With Butler Matrix Network," IEEE Antennas Wirel. Propag. Lett., vol. 7, pp. 432–435, 2008.

[19] S. Bulja, D. Mirshekar-Syahkal, M. Yazdanpanahi, R. James, S. E. Day, and F. A. Fernandez, "60 GHz Reflection Type Phase Shifter based on liquid crystal," in IEEE Radio and Wireless Symposium (RWS), 2010, pp. 697–699.

[20] Y. Yikun et al., "A 60GHz digitally controlled phase shifter in CMOS," in 34th European Solid-State Circuits Conference (ESSCIRC), 2008, pp. 250–253.

[21] R. Rudd et al., "Building Materials and Propagation," Ofcom Technical Report, 2014.

[22] T. S. Rappaport et al., "Broadband Millimeter-Wave Propagation Measurements and Models Using Adaptive-Beam Antennas for Outdoor Urban Cellular Communications," IEEE Trans. Antennas Propag., vol. 61, no. 4, pp. 1850–1859, Apr. 2013.

[23] T. Manabe, Y. Miura, and T. Ihara, "Effects of antenna directivity on indoor multipath propagation characteristics at 60 GHz," in 6th Int. Symp. Personal, Indoor and Mobile Radio Commun. (PIMRC), Sep. 1995, p. 1035–1039.

[24] T. Manabe, Y. Miura, and T. Ihara, "Effects of antenna directivity and polarization on indoor multipath propagation characteristics at 60 GHz," IEEE J. Sel. Areas Commun., vol. 14, no. 3, pp. 441–448, Apr. 1996.

[25] N. Chahat, G. Valerio, M. Zhadobov, and R. Sauleau, "On-Body Propagation at 60 GHz," IEEE Trans. Antennas Propag., vol. 61, no. 4, pp. 1876–1888, Apr. 2013.

[26] M. Boers et al., "A 16TX/16RX 60 GHz 802.11ad Chipset With Single Coaxial Interface and Polarization Diversity," IEEE J. Solid-State Circuits, vol. 49, no. 12, pp. 3031–3045, Dec. 2014.

[27] T. Kamgaing et al., "Ultra-thin dual polarized millimeter-wave phased array system-in-package with embedded transceiver chip," in IEEE MTT-S Int. Microwave Symp. (IMS), 2015, pp. 1–4.

[28] A. Balankutty et al., "A 12-element 60GHz CMOS phased array transmitter on LTCC package with integrated antennas," in IEEE Asian Solid-State Circuits Conf., 2011, pp. 273–276.

[29] A. Natarajan et al., "A Fully-Integrated 16-Element Phased-Array Receiver in SiGe BiCMOS for 60-GHz Communications," IEEE J. Solid-State Circuits, vol. 46, no. 5, pp. 1059–1075, 2011.

[30] "Project Soli." [Online]. Available: https://www.google.com/atap/project-soli/. [Accessed: 16-Feb-2016].

[31] “Chassis Systems Control LRR3: 3rd generation Long-Range Radar Sensor.”, Bosch Technical Report, 2009.

[32] J. Hasch et al., “Millimeter-Wave Technology for Automotive Radar Sensors in the 77 GHz Frequency Band,” IEEE Trans. Microw. Theory Tech., vol. 60, no. 3, pp. 845–860, Mar. 2012.

[33] W. Menzel, “Millimeter-wave radar for civil applications,” in European Radar Conf. (EuRAD), Sep. 2010, pp. 89–92.

[34] V. Manasson, L. Sadovnik, and R. Mino, “MMW scanning antenna,” in Proc. IEEE National Aerospace and Electronics Conference (NAECON), 1996, pp. 145–149.

[35] B. Korn and H.-U. Doehler, “Passive landing aids for precision EVS approach and landing,” in 22nd Digital Avionics Systems Conference, Oct. 2003, p. 9.D.1-9.1.

[36] L. Yujiri, “Passive Millimeter Wave Imaging,” in 2006 IEEE MTT-S International Microwave Symposium Digest, 2006, pp. 98–101.

[37] R. Boehnke and S. Saito, “Hand-held security scanning device,” WO2014032984 A1, Mar. 6th 2014.

[38] S. Hantscher et al. “94 GHz person scanner with circular aperture as part of a new sensor concept on airports,” in Int. Radar Symp. (IRS) , Jun. 2010, pp. 1–4.

[39] L. Zhang, “Millimetre Wave Imaging for Concealed Target Detection,” Ph.D. Dissertation, Queen Mary Univ. of London, 2011.

[40] J. L. H. Webb, D. C. Munson, and N. J. S. Stacy, “High-resolution planetary imaging via spotlight-mode synthetic aperture radar,” in Proc. of 1st International Conference on Image Processing, Nov. 1998, pp. 451–455.

[41] C. G. Christodoulou et al. “Reconfigurable Antennas for Wireless and Space Applications,” Proc. IEEE, vol. 100, no. 7, pp. 2250–2261, Jul. 2012.

[42] T. Shroyer, “Satcom-on-the-move why one size doesn’t fit all,” in IEEE Military Communic. Conf. (MILCOM), 2012, pp. 1–6.

[43] T. E. Bogale and L. B. Le, “Massive MIMO and mmWave for 5G Wireless HetNet: Potential Benefits and Challenges,” IEEE Veh. Technol. Mag., vol. 11, no. 1, pp. 64–75, Mar. 2016.

[44] A. Osseiran et al., “Scenarios for 5G mobile and wireless communications: the vision of the METIS project,” IEEE Commun. Mag., vol. 52, no. 5, pp. 26–35, May 2014.

[45] E. Hossain et al., “Evolution toward 5G multi-tier cellular wireless networks: An interference management perspective,” IEEE Wirel. Commun., vol. 21, no. 3, pp. 118–127, Jun. 2014.

[46] V. Kallnichev, “Analysis of beam-steering and directive characteristics of adaptive antenna arrays for mobile communications,” IEEE Antennas Propag. Mag., vol. 43, no. 3, pp. 145–152, Jun. 2001.

[47] M. Agiwal, A. Roy, and N. Saxena, “Next Generation 5G Wireless Networks: A Comprehensive Survey,” IEEE Commun. Surv. Tutorials, vol. 18, no. 3, pp. 1617–1655, 2016.

[48] T. Rappaport, W. Roh, and K. Cheun, “Mobile’s millimeter-wave makeover,” IEEE Spectr., vol. 51, no. 9, pp. 34–58, Sep. 2014.

[49] J. G. Yang and K. Yang, “Ka-Band 5-Bit MMIC Phase Shifter Using InGaAs PIN Switching Diodes,” IEEE Microw. Wirel. Components Lett., vol. 21, no. 3, pp. 151–153, Mar. 2011.

[50] D. Teeter et al., “Ka-band GaAs HBT PIN diode switches and phase shifters,” in IEEE MTT-S Int. Microwave Symp. (IMS), 1994, pp. 451–454.

[51] K. Maruhashi, H. Mizutani, and K. Ohata, “Design and performance of a Ka-band monolithic phase shifter utilizing nonresonant FET switches,” IEEE Trans. Microw. Theory Tech., vol. 48, no. 8, pp. 1313–1317, 2000.

[52] V. Sokolov et al., “A Ka-Band GaAs Monolithic Phase Shifter,” IEEE Trans. Microw. Theory Tech., vol. 31, no. 12, pp. 1077–1083, Dec. 1983.

[53] A. Moessinger et al., “Compact tunable Ka-band phase shifter based on liquid crystals,” in Int. Microwave Symp(IMS)., 2010, pp. 1020–1023.

[54] A. Hoehn, P. B. Hager, and J. T. Harder, “Design characterization of an electronic steerable Ka-band antenna using liquid crystal phase shifters,” in IEEE Aerospace Conference, 2013, pp. 1–14.

[55] Byung-Wook Min and G. M. Rebeiz, “Ka-Band Low-Loss and High-Isolation Switch Design in 0.13um CMOS,” IEEE Trans. Microw. Theory Tech., vol. 56, no. 6, pp. 1364–1371, Jun. 2008.

[56] K.-J. Koh, J. W. May, and G. M. Rebeiz, “A Millimeter-Wave (40–45 GHz) 16-Element Phased-Array Transmitter in 0.18μm SiGe BiCMOS Technology,” IEEE J. Solid-State Circuits, vol. 44, no. 5, pp. 1498–1509, May 2009.

[57] G. Rebeiz and K. Koh, “Silicon RFICs for phased arrays,” IEEE Microw. Mag., vol. 10, no. 3, pp. 96–103, May 2009.

[58] Dong-Woo Kang et al., “Single and Four-Element Ka-Band Transmit/Receive Phased-Array Silicon RFICs With 5-bit Amplitude and Phase Control,” IEEE Trans. Microw. Theory Tech., vol. 57, no. 12, pp. 3534–3543, Dec. 2009.

[59] A. Brejcha, “Microwave Communications from the Outer Planets: The Voyager Project,” in 9th European Microwave Conference, 1979, 1979, pp. 34–44.

[60] B. Rohrdantz et al., “An Electronically Scannable Reflector Antenna Using a Planar Active Array Feed at Ka-Band,” IEEE Trans. Microw. Theory Tech., vol. 65, no. 5, pp. 1650–1661, May 2017.

[61] N. Chahat, et.al “CubeSat deployable Ka-band reflector antenna for Deep Space missions,” in IEEE Int. Symp. Antennas Propag. (APSURSI), Jul. 2015, pp. 2185–2186.

[62] D. Berry, R. Malech, and W. Kennedy, "The reflectarray antenna," IEEE Trans. Antennas Propag., vol. 11, no. 6, pp. 645–651, Nov. 1963.

[63] D.-C. Chang and M.-C. Huang, "Microstrip reflectarray antenna with offset feed," Electron. Lett., vol. 28, no. 16, p. 1489, 1992.

[64] Dau-Chyrh Chang and Ming-Chih Huang, "Multiple-polarization microstrip reflectarray antenna with high efficiency and low cross-polarization," IEEE Trans. Antennas Propag., vol. 43, no. 8, pp. 829–834, 1995.

[65] H. Yang et al., "Design of Resistor-Loaded Reflectarray Elements for Both Amplitude and Phase Control," IEEE Antennas Wirel. Propag. Lett., vol. 16, pp. 1159–1162, 2017.

[66] M. E. Bialkowski, A. W. Robinson, and H. J. Song, "Design, development, and testing of X-band amplifying reflectarrays," IEEE Trans. Antennas Propag., vol. 50, no. 8, pp. 1065–1076, Aug. 2002.

[67] S. V. Hum and J. Perruisseau-Carrier, "Reconfigurable Reflectarrays and Array Lenses for Dynamic Antenna Beam Control: A Review," IEEE Trans. Antennas Propag., vol. 62, no. 1, pp. 183–198, Jan. 2014.

[68] X. Yang et al., "A Broadband High-Efficiency Reconfigurable Reflectarray Antenna Using Mechanically Rotational Elements," IEEE Trans. Antennas Propag., vol. 65, no. 8, pp. 3959–3966, Aug. 2017.

[69] R. E. Hodges, et al., "Novel deployable reflectarray antennas for CubeSat communications," in IEEE MTT-S Int. Microwave Symp. (IMS), May 2015, pp. 1-4.

[70] M. Kim, J. G. Yang, and K. Yang, "Switched transmission-line type Q-band 4-bit MMIC phase shifter using InGaAs pin diodes," Electron. Lett., vol. 46, no. 3, p. 219, Feb. 2010.

[71] K. Maruhashi, H. Mizutani, and K. Ohata, "Design and performance of a Ka-band monolithic phase shifter utilizing nonresonant FET switches," IEEE Trans. Microw. Theory Tech., vol. 48, no. 8, pp. 1313–1317, 2000.

[72] M. Aust et al., "GaAs monolithic components development for Q-band phased array application," in IEEE Microwave Symposium Digest (MTT-S), 1992, pp. 703–706.

[73] H.C. Nathanson, and R.A Wickstrom, "A resonant-gate silicon surface transistor with high-q band-pass properties". Applied Physics Letters vol. 7, no. 4, pp. 84–86, Aug. 1965.

[74] B. Pillans, et al., "Advances in RF MEMS phase shifters from 15 GHz to 35 GHz," in IEEE/MTT-S International Microwave Symposium Digest, Jun. 2012, pp. 1–3.

[75] G. I. Kiani, T. S. Bird, and K. Y. Chan, "MEMS enabled frequency selective surface for 60 GHz applications," in in IEEE Int. Symp. Antennas Propag. (APSURSI), Jul. 2011, pp. 2268–2269.

[76] Yi Yang et al., "MEMS-loaded millimeter wave frequency reconfigurable quasi-Yagi dipole antenna," Asia-Pacific Microwave Conf. (APMC), Dec. 2011. pp. 1318–1321.

[77] Y. Garbovskiy et al., "Liquid crystal phase shifters at millimeter wave frequencies," J. Appl. Phys., vol. 111, no. 5, p. 54504, Mar. 2012.

[78] J. R. Flemish et al., "A new silicon-based photoconductive microwave switch," Microw. Opt. Technol. Lett., vol. 51, no. 1, pp. 248–252, Jan. 2009.

[79] R. L. Haupt, J. Flemish, and D. Aten, "Adaptive Nulling Using Photoconductive Attenuators," IEEE Trans. Antennas Propag., vol. 59, no. 3, pp. 869–876, Mar. 2011.

[80] R. L. Haupt and J. R. Flemish, "Broadband linear array with photoconductive attenuators," Proc. European Conf. Antennas Propag. (EuCAP), Apr. 2010, pp. 1–4

[81] H. Su, et al., "Optically tuned polarisation reconfigurable antenna," in IEEE Asia-Pacific Conf. Antennas Propag. (APCAP), 2012, pp. 265–266.

[82] H. Su et al., "Optically controlled frequency selective surface for millimeter-wave applications," in IEEE Int. Symp. Antennas Propag. (APSURSI), Aug. 2012, pp. 1–2.

[83] C. J. Panagamuwa, A. Chauraya, and J. C. Vardaxoglou, "Frequency and Beam Reconfigurable Antenna Using Photoconducting Switches," IEEE Trans. Antennas Propag., vol. 54, no. 2, pp. 449–454, Feb. 2006.

[84] N. T. Yardimci, S.-H. Yang, C. W. Berry, and M. Jarrahi, "High-Power Terahertz Generation Using Large-Area Plasmonic Photoconductive Emitters," IEEE Trans. Terahertz Sci. Technol., vol. 5, no. 2, pp. 223–229, Mar. 2015.

[85] J. I. Herranz-Herruzo et al., "LOCOMO satcom terminal: A switchable RHCP/LHCP Array Antenna for on-the-move applications in Ka-band," in IEEE Int. Symp. Antennas Propag. (APSURSI), Jul. 2015, pp. 210–211.

[86] Y. Tawk and C. G. Christodoulou, "A New Reconfigurable Antenna Design for Cognitive Radio," IEEE Antennas Wirel. Propag. Lett., vol. 8, pp. 1378–1381, 2009.

[87] R. Pereira, R. Gillard, R. Sauleau, P. Potier, T. Dousset, and X. Delestre, "Four-state dual polarisation unit-cells for reflectarray applications," Electron. Lett., vol. 46, no. 11, p. 742, 2010.

[88] Chi Lee, P. Mak, and A. DeFonzo, "Optical control of millimeter-wave propagation in dielectric waveguides," IEEE J. Quantum Electron., vol. 16, no. 3, pp. 277–288, Mar. 1980.

[89] A. Chauraya, C. J. Panagamuwa, and J. C. Vardaxoglou, "Beam scanning antenna with photonically tuned EBG phase shifters." in IEEE Int. Symp. Antennas Propag. (APSURSI), Jul. 2006, pp. 2283–2286.

[90] C. D. Gamlath, D. Benton, and M. J. Cryan, "Microwave characterisation of

optically illuminated silicon," in International Conf. on Transparent Optical Networks (ICTON), Jul. 2012, pp. 1–4.

[90] H. Tang, F. Zhao, and F. Zhang, "Investigation on an optically-controlled phase-shifter based organic semiconductor poly-(3-hexylthiophene) (P3HT)," J. Phys. Conf. Ser., vol. 276, no. 1, p. 12092, Feb. 2011.

[91] A. M. Vaucher, C. D. Striffler, and C. H. Lee, "Theory Of Optically Controlled Millimeter-wave Phase Shifters," IEEE Trans. Microw. Theory Tech., vol. 31, no. 2, pp. 209–216, Feb. 1983.

[92] M. Riordan, L. Hoddeson, and C. Herring, "The invention of the transistor," Rev. Mod. Phys., vol. 71, no. 2, pp. 336–345, 1999.

[93] C. D. Gamlath, D. M. Benton, and M. J. Cryan, "Investigation of an optically reconfigurable plasma for silicon based microwave applications," in European Microwave Conf. (EuMC), Oct. 2013, pp. 874–877

[94] C. D. Gamlath, D. M. Benton, and M. J. Cryan, "Microwave Properties of an Inhomogeneous Optically Illuminated Plasma in a Microstrip Gap," IEEE Trans. Microw. Theory Tech., vol. 63, no. 2, pp. 374–383, Feb. 2015.

[95] E. K. Kowalczuk, R. D. Seager, and C. J. Panagamuwa, "Investigating factors affecting photoconductive microwave switch performance using 3D EM simulation," in Loughborough Antennas & Propagation Conference (LAPC), Nov. 2015, pp. 1–5.

[96] E. Kowalczuk, "Simulating, fabricating and characterising photoconductive microwave switches for RF applications," Ph.D. dissertation, Loughborough University, 2014.

[97] E. K. Kowalczuk, R. D. Seager, and C. J. Panagamuwa, "Power handling of a photoconductive microwave switch," in Loughborough Antennas & Propagation Conference (LAPC), Nov. 2016, pp. 1–3.

[98] D. Draskovic et al., "Frequency switchable dual-band branch-line couplers," in European Microwave Conference (EuMC), Sept. 2009, pp. 133–136.

[99] K. Chakrabarty et al., "Linearity evaluation of optically reconfigurable UWB microstrip bandpass filter," in IEEE Int. Symp. Antennas Propag. (APSURSI), Jul. 2013, pp. 786–787.

[100] J. R. Flemish and R. L. Haupt, "Optimization of a Photonically Controlled Microwave Switch and Attenuator," Microw. Theory Tech. IEEE Trans., vol. 58, no. 10, pp. 2582–2588, Oct. 2010.

[101] "OSRAM SFH4550 Infrared Emitter." [Online]

[102] "SFH 4710 OSRAM [Online].

[103] P. Nayeri, A. Z. Elsherbeni, and F. Yang, "Radiation Analysis Approaches for Reflectarray Antennas [Antenna Designer's Notebook]," IEEE Antennas Propag. Mag., vol. 55, no. 1, pp. 127–134, Feb. 2013.

[104] “PTC Mathcad.” [Online]. Available: https://www.ptc.com/en/engineering-math-software/mathcad. [Accessed: 21-Sep-2017].

[105] S. F. Jilani and A. Alomainy, “Planar millimeter-wave antenna on low-cost flexible PET substrate for 5G applications,” in 10th European Conference on Antennas and Propagation (EuCAP), Apr. 2016, pp. 1–3.

[106] “TI LM3410.” [Online]. Available: http://www.ti.com/product/LM3410.

[107] J. A. Encinar, “Design of two-layer printed reflectarrays using patches of variable size,” IEEE Trans. Antennas Propag., vol. 49, no. 10, pp. 1403–1410, 2001.

[108] Y. Pan and Y. Zhang, “Analysis of Blockage Effects in a Center-Fed Reflectarray,” Microw. Opt. Technol. Lett., vol. 55, no. 8, pp. 1921–1926, Aug. 2013.

[109] E. Muehldorf, “The phase center of horn antennas,” IEEE Trans. Antennas Propag., vol. 18, no. 6, pp. 753–760, Nov. 1970.

[110] T. Pochiraju and V. Fusco, “Amplitude and Phase Controlled Reflectarray Element Based on an Impedance Transformation Unit,” IEEE Trans. Antennas Propag., vol. 57, no. 12, pp. 3821–3826, Dec. 2009.

[111] C. G. Parini et al., “The design, construction and use of a millimetrewave compact antenna test range” 6th Int. Conf. Antennas and Propag., Apr. 1989, pp. 345–350

[112] T. J. Hewison and R. Saunders, “Measurements of the AMSU-B antenna pattern,” IEEE Trans. Geosci. Remote Sens., vol. 34, no. 2, pp. 405–412, Mar. 1996.

[113] “Near-field vs Far-field.” [Online]. Available: http://educypedia.karadimov.info/library/NSI-near-far.pdf.

[114] S. Gregson, J. McCormick, and C. Parini, Principles of Planar Near-Field Antenna Measurements. The Institution of Engineering and Technology, Michael Faraday House, Six Hills Way, Stevenage SG1 2AY, UK: IET, 2007.

[115] J.-D. Lacasse and J.-J. Laurin, “A Method for Reflectarray Antenna Design Assisted by Near Field Measurements,” IEEE Trans. Antennas Propag., vol. 54, no. 6, pp. 1891–1897, Jun. 2006.

[116] S. Dieter and W. Menzel, “High-Resolution Probes for Near-Field Measurements of Reflectarray Antennas,” IEEE Antennas Wirel. Propag. Lett., vol. 8, pp. 157–160, 2009.

[117] A. Tamminen et al., “Reflectarray Design for 120-GHz Radar Application: Measurement Results,” IEEE Trans. Antennas Propag., vol. 61, no. 10, pp. 5036–5047, Oct. 2013.

[118] D. Rodriguez Prado et al., “Design, Manufacture, and Measurement of a Low-Cost Reflectarray for Global Earth Coverage,” IEEE Antennas Wirel. Propag. Lett., vol. 15, pp. 1418–1421, 2016.

[119] M. Zhou et al., “Investigations on accurate analysis of microstrip reflectarrays,” in Proc. of 33rd ESA Antenna Workshop, 2011

[120] “ORD Solutions - RoVa 3D.” [Online]. Available: https://www.ordsolutions.com

[121] D. Pilz and W. Menzel, “Folded reflectarray antenna,” Electron. Lett., vol. 34, no. 9, p. 832, 1998.

[122] “Antennas Electromagnetics Research Group: NSI planar near-field beam pattern scanner.” [Online]. Available: http://antennas.eecs.qmul.ac.uk/